Customer	**:**	**ESRIN**	**Document Ref**	**:**	**S2PAD-ATBD-0001**
Contract No	**:**	**21450/08/I-EC**	**Issue Date**	**:**	**20 September 2012**
WP No	**:**	**1.1.5.1.2**	**Issue**	**:**	**2.0**

Title : **Sentinel-2 MSI – Level 2A Products Algorithm Theoretical Basis Document**

Abstract : This document is the ATBD for Level 2A processing.

Authors : R. Richter (DLR), J. Louis (Telespazio France), Uwe Müller-Wilm (Telespazio VEGA Deutschland GmbH)

Approval : Christian Laroque

Accepted : Christine Dingeldey
Quality Assurance Manager

Distribution :

Hard Copy File:
Filename: S2PAD-VEGA-ATBD-0001-2_0_L2A_ATBD.docx

TELESPAZIO VEGA DEUTSCHLAND
A Finmeccanica / Thales Company

DLR

Telespazio VEGA Deutschland GmbH
Europaplatz 5, D-64293 Darmstadt, Germany
Tel: +49 (0)6151 8257-0 Fax: +49 (0)6151 8257-799
www.telespazio-vega.de

This Page Is Intentionally Blank

TABLE OF CONTENTS

TABLE OF CONTENT FOR FIGURES

TABLE OF CONTENT FOR TABLES

AMENDMENT POLICY

This document shall be amended by releasing a new edition of the document in its entirety. The Amendment Record Sheet below records the history and issue status of this document.

AMENDMENT RECORD SHEET

ISSUE	DATE	DCI No	REASON
1.0	Jan 2009	N/A	Initial Issue
1.2	Sep 2009	N/A	Updated following Review by ESA
1.3	6 Nov 2009	N/A	Fixed RIDs from PDR-1.
1.4	13 Nov 2009	N/A	Updated according to the comments received from ESA on 11th November 2009.
1.5	12 Apr 2010	N/A	Fix various RIDs from S2_PADPDR_2.
1.6	5 May 2010	N/A	Fix RID PADPDR-131.
1.7	01 Dec 2010	N/A	Merge with SMAC ATBD and integrated changes after S2 phase 1 review.
1.8	13 Mar 2011	N/A	Updated following Review by ESA
1.9	03.Jul 2012	N/A	Updated for CDR
2.0	15.Aug 2012	N/A	FIX RIDs from CDR

DOCUMENT CHANGE RECORD

		DCR No	***001***
		Date	06 Nov 2009
		Originator	R. Richter
		Approved by	M. Niézette
1. Document Title:		Sentinel-2 MSI – Level 2A Products Algorithm Theoretical Basis Document	
2. Document Reference Number:		S2PAD-DLR-ATBD-0002	
3. Document issue / revision number:		1.3	
4. Page	5. Paragraph	6. Reason for change	
	Section 2.1	RID PDR-59. (water mask obviously is not correct in case of sun glint) Tasselled cap transform is described in section 2.6. So far it is not adapted to S2	
	Section 2.4 Section 4	RID PDR-62. P. 8: see new chapter 4 P. 15: there is no cost function in this case, just a spectral correlation, see modified section 2.4. Places with no DDV are assigned the average AOT value of DDV pixel. Validation of the DDV including thresholds: see MODIS reference.	
	Section 4	RID PDR-65. Cirrus band SNR=200, not 20. 1.24 channel sentence was deleted, parallax differences are an item: is included in chapter 4.	
	Section 1	PDR-37. Sentence on tiling capability for S2 was removed in chapter 1.	
	Section 4	PDR-38.	
	Section 4	PDR-40. MSI band numbers are now included.	

	DCR No	***002***
	Date	13 Nov 2009
	Originator	M. Niézette
	Approved by	M. Niézette
1. Document Title:	Sentinel-2 MSI – Level 2A Products Algorithm Theoretical Basis Document	

2. Document Reference Number:		S2PAD-ATBD-0001
3. Document issue / revision number:		1.4
4. Page	5. Paragraph	6. Reason for change
	Document	Comment from ESA in Ferran Gascon's email of 11th November 2009. Band -8 name changed, "panchromatic NIR band" replaced by "wide NIR band".
	Front sections	List of Figures, List of Tables, and DCR for issue 1.3 fixed.

	DCR No	***003***
	Date	12 Apr 2010
	Originator	R. Richter
	Approved by	M. Niézette
1. Document Title:		Sentinel-2 MSI – Level 2A Products Algorithm Theoretical Basis Document
2. Document Reference Number:		S2PAD-DLR-ATBD-0002
3. Document issue / revision number:		1.5

4. Page	5. Paragraph	6. Reason for change
	section 2.1	RID-PDR-74 : mask processing
	Section 2.4	RID-PDR-70: Aerosol estimates
	Section 2.4	RID-PDR-77: AOT retrieval
	Section 2.4	RID-79: Aerosol model
	Section 2.8	RID-85: Cloud shadow removal
	Section 2.1	RID-113: Valididity of thresholds
	Section 2.10	RID-122: DEM accuracy
	Section 2.3	RID-127, ozone, MODTRAN accuracy
	Section 2.3, 3.2, 3.6	RID-130: Region-dependent water vapor
	Section 2.4	RID-129
	Section 3	RID-123
	Section 2.7	RID-120 cirrus is baseline processing
	Section 2.4	RID-119

	Section 2.6	RID-118: exclusion of waer pixels
	Section 2.4	RID-115: range of elevations in AOT
	Section 6	RID-111: level 1C in TOA reflectance
	Section 2.1	RID-75: acronym definition
	Section 2.1	RID-59: thin cirrus (min refl. value 1%)
	Section 2.1	RID-58: cloud detection threshold
	Section 4 (Answer was already included)	RID-13: spatial resolution
	Section 2.5: Typo is corrected	RID-12: Equation 2.32 wrong

	DCR No	***004***
	Date	05 May 2010
	Originator	R. Richter
	Approved by	M. Niézette
1. Document Title:	Sentinel-2 MSI – Level 2A Products Algorithm Theoretical Basis Document	
2. Document Reference Number:	S2PAD-DLR-ATBD-0002	
3. Document issue / revision number:	1.6	
4. Page	5. Paragraph	6. Reason for change
	section 1	PADPDR-131
	Section 2	PADPDR-131
	Section 3	PADPDR-131
	Section 4	PADPDR-131
	Section 5	PADPDR-131
	Section 6	PADPDR-131

		DCR No	***005***
		Date	01 Dec 2010
		Originator	Uwe Müller-Wilm
		Approved by	M. Niézette
1. Document Title:		Sentinel-2 MSI – Level 2A Products Algorithm Theoretical Basis Document	
2. Document Reference Number:		S2PAD-ATBD-0001	
3. Document issue / revision number:		1.7	
Page and table # refer to the previous SMAC and ATCOR ATBDs			
4. Page	5. Paragraph	6. Reason for change as requested by reviewer.	
integrated from ATCOR ATBD:			
All	All	Merged ATCOR and SMAC ATBD.	
All	All	Replaced MODTRAN by libRadtran.	
All	All	Replaced all references to SMAC with 2A-SC and all references to ATCOR with 2A-AC.	
11	1.0	Document structure adapted to merge.	
11	1.1	Removed remark on preliminary processing strategy as this has been updated in section 4.1.	
14	2.1	Adapted remark on haze removal.	
14	2.1	Added section on ground elevation increase up to 8 km.	
18	2.1 – 2.2	Classification map: replaced with SMAC one.	
21	2.3	Changed section on mid-latitude.	
44	2.12	Added algorithm for adjacency effect correction, Input from DLR.	
45 - 56	3	Removed error and sensitivity analysis according to reviewer comments.	
59 -62	4	Moved processing strategy to new chapter 4.	
59 -62	4	Moved comments on cirrus removal to section 4.6.	
62	4	Discussed reviewer comments on tiling.	
59	4.1	Added new section about proposed processing strategy as input from DLR.	
63	5	Removed ATCOR processing of test scenes according to reviewer comments.	
integrated form SMAC ATBD:			
18 - 44	2.1, 2.2	Integrated section on scene classification into merged ATBD.	

19	2.2.1.1	Added cubic spline for resampling.
45	2.3	Removed section on validation.
63	3	Removed section on SMAC AC.
97	4	Moved References on Scene Classification to merged ATBD.
101	Appendix A	Moved Appendix on Cirrus Detection to merged ATBD.

	DCR No	***006***
	Date	13 Mar 2011
	Originator	Uwe Müller-Wilm
	Approved by	M. Niézette
1. Document Title:	Sentinel-2 MSI – Level 2A Products Algorithm Theoretical Basis Document	
2. Document Reference Number:	S2PAD-ATBD-0001	
3. Document issue / revision number:	1.8	

4. Page	5. Paragraph	6. Reason for change as requested by reviewer.
All	All	Use the band names (B1, B2, etc) instead of blue, red, etc.
	2.2.1.2	In order to identify not saturated and not defective pixels, the masks from Level-1C product need to be used by the L2A processor and identified in this section as input.
	2.3	Section describing the Output Data is missing.
	Fig. 3-2	Add YES/NO label to the decision steps.
	3.2.3.6	Detail the DILATE operator function.
	3.2.8	Be more precise in detailing this median filter.
	3.2.3.1	Assumed that VEGA will provide this auxiliary data file (as it is not an available product but it still has to be derived from MODIS snow monthly products).
	Fig. 3-1	Step for resampling at 60m resolution is missing.
	3.2	This text should be an introduction to the cloud/snow detection algorithm. This note can be included in the description of the pre-processing step which is missing (resampling at 60m, discarding defective/saturated pixels…).
	3.2.3.1	PIXELS MASKS (for saturated, defective pixels) from Level-1C need to be identified as Processor Input.
	Figure 3-6	Assumed VEGA will provide this auxiliary input file.

	3.2.3	Some black regions (therefore identified as never snowing regions) are identified on European coasts (in UK, NL, E, I, Croatia…) area and inland Italy.
	Fig.3.2.1	What happens with the other types of surfaces (e.g. urban/artificial targets)? In which class do they fall?
	4.1	This whole section is not consistent with the decision to keep the native L1C resolution as output of the L2A processing and neither with the content of the Product Definition.

	DCR No	***007***
	Date	02 Jul 2012
	Originator	Uwe Müller-Wilm
	Approved by	C. Laroque
1. Document Title:	Sentinel-2 MSI – Level 2A Products Algorithm Theoretical Basis Document	
2. Document Reference Number:	S2PAD-ATBD-0001	
3. Document issue / revision number:	1.9	

4. Page	5. Paragraph	6. Reason for change as requested by reviewer.
	2.1, 2.2	In- and output data are now referring to the PDD, in order to align the documents with each other.
	2.4	Update of processing strategy after requirement changes on number of tiles.
	2.4.2	Remark EC: resampling of DEM
	2.4.2	Remark EC: precise ‘previously’
	Appendix A	New processing strategy for continuous data strips added.
	All	Reference documents updated and all references in document corrected.

		DCR No	***008***
		Date	15 Aug 2012
		Originator	Uwe Müller-Wilm
		Approved by	C. Laroque
1. Document Title:		Sentinel-2 MSI – Level 2A Products Algorithm Theoretical Basis Document	
2. Document Reference Number:		S2PAD-ATBD-0001	
3. Document issue / revision number:		2.0	
4. Page	5. Paragraph	6. Reason for change as requested by reviewer.	
	Figure 3-2	ATB_01	
	3.2.3.2	ATB_02	
	3.2.2	ATB_03	
	3.2.3.2	ATB_04	
	3.2.3.6	ATB_05	
	3.4.1	ATB_06	
	4.1	ATB_07	
	Figure 4.2	ATB_08	
	1.1	ATB_09	
	3.2.3.2	ATB_10	
	3.2.2	ATB_11	
	3.2.3.2	ATB_12	
	3.1	ATB_13	
	Figure 3-1	ATB_14	
	3.2.3.1	ATB_15	
	Page 47	ATB_16	
	Page 47	ATB_16b	
	4.1	ATB_17	
	Section 4.3, End	ATB_18	

	4.8	ATB_19
	4.11	ATB_20
	1.1	ATB_21
	1.1	ATB_22
	1.1	ATB_23
	1.3	ATB_24
	table 4-1	ATB_25

1. INTRODUCTION

1.1 Purpose and Scope

This Algorithm Theoretical Basis Document (ATBD) describes the algorithms for the Level 2A processing of Sentinel-2 imagery over land. Sentinel-2 is the High spatial Resolution (HR) optical payload of the Global Monitoring of Environment and Security (GMES) program.

Level 2A processing is mainly performed by two parts:

- Scene classification (SC): the generation of a scene classification map and of two quality indicators, (1) a map of cloud probability and (2) a map of snow probability are additional products and serve as a necessary input for the atmospheric correction part and is described in chapter 2 of this document.

- Atmospheric correction (AC): this algorithm has to be performed in order to obtain Bottom of Atmosphere (BOA) corrected transforms of multispectral Level 1C (L1C) products. L1C products cover Top of Atmosphere (TOA) reflectance images. The main processing will be named “Sentinel-2 Atmospheric Correction” (S2AC) algorithm throughout the document. For this purpose, a large database of look-up tables (LUTs) has to be compiled using the atmospheric radiative transfer model *libRadtran*[1] [LRDT-1, LRDT-2]. The LUTs have to be generated for a wide variety of atmospheric conditions, solar geometries, and ground elevations and need to be calculated with a high spectral resolution (0.6 nm). This database has to be subsequently resampled with the Sentinel-2 spectral responses, in order to obtain the sensor-specific functions needed for the atmospheric correction, i.e. path radiance, direct and diffuse transmittances, direct and diffuse solar fluxes, and spherical albedo. The AC part is described in chapter 3 of this document.

Restrictions:

1. The Look Up tables are only compiled for the rural aerosol and the mid-latitude summer (MS) atmosphere with its corresponding ozone column (331 DU for sea level. Other Look up Tables can be generated on request but are not part of the current baseline.

2. The current version of the processor will not give validated results over water or on coastal regions. The design of the current implementation does not prevent such an extension, but this is not part of the current baseline.

1.2 Structure of the Document

The document is structured as follows:

The remaining part of this chapter reviews and summarizes the relevant Sentinel-2 documentation to assess the prerequisites of the L2A processing.

---

[1] *libRadtran - library for radiative transfer - is a collection of C and Fortran functions and programs for calculation of solar and thermal radiation in the Earth's atmosphere. libRadtran is freely available under the GNU General Public License. Current release at state of this document creation is: 1.5-beta, February 2, 2010..*

Chapter 2 lists the sensor characteristics which are the common base for the next two chapters 3 and 4.

Chapter 3 describes the algorithms proposed to detect clouds, snow and cloud shadows, and to generate the classification mask and the quality indicators.

Chapter 4 contains a detailed theoretical description of each retrieval algorithm for the atmospheric correction (aerosol, water vapour, haze removal, cirrus removal and surface reflectance retrieval in flat and rugged terrain). The chapter finishes with a preliminary proposed processing strategy for Sentinel-2 for the AC part.

APPENDIX A introduces a new strategy on the Sentinel-2 (S2) aerosol retrieval for long strips of continuous data acquisition.

APPENDIX B contains a more detailed description of the Neural Network Algorithm used for the initial classification of cloud shadows as described in section 3.4.1.

APPENDIX C lists a collection of relevant documentation, which forms the scientific background of the algorithms described before.

1.3 Documentation and Definitions

The reference list of all project related documents with their version number and issue date is given in:

[S2-L2A-GLOS] S2PAD Project Glossary S2PAD-VEGA-GLO-0001, version 3.0, 30.08.2012

1.3.1 Informative Reference Documents

[S2-L2A-PDD] Sentinel-2 – Level-2A Product Definition Document

[LRDT-1] B. Mayer, B., Kylling, A., The libRadtran software package for radiative transfer calculations

[LRDT-2] B. Mayer et al., libRadtran: library for radiative transfer calculation http://www.libradtran.org/doc/libRadtran.pdf

[ECMWF] User guide to ECMWF forecast products: http://www.ecmwf.int/products/forecasts/guide/user_guide.pdf

[S2-L2A-PFS] Sentinel-2 MSI – Level 2A Product Format Specification Technical Note

[S2-L2A-TN5] Sentinel-2 MSI – Selection of Algorithms for Level 2A Products Generation

1.3.2 Relation to other Documents

The *Sentinel-2 MSI - Level 2A Products Specification Technical Note* [S2-L2A-PFS] describes Sentinel-2 Level 2A file naming convention and presents how the Sentinel-2 Level 2A XSD schemas are organized.

2. SENSOR CHARACTERISTICS,I/O DATA

Sentinel-2 will be launched into a sun-synchronous orbit at 786 km. The instrument will cover a 290 km swath allowing a revisit time of 10 days. A second Sentinel-2 is planned for a later launch which will reduce the revisit time to 5 days. Data encoding is 12 bits/pixel and the radiometric accuracy is 5% (goal 3%).

2.1 Sensor specification

The sensor has three different spatial resolutions (10 m to 60 m) and 13 spectral bands as shown in Figure 2-1.

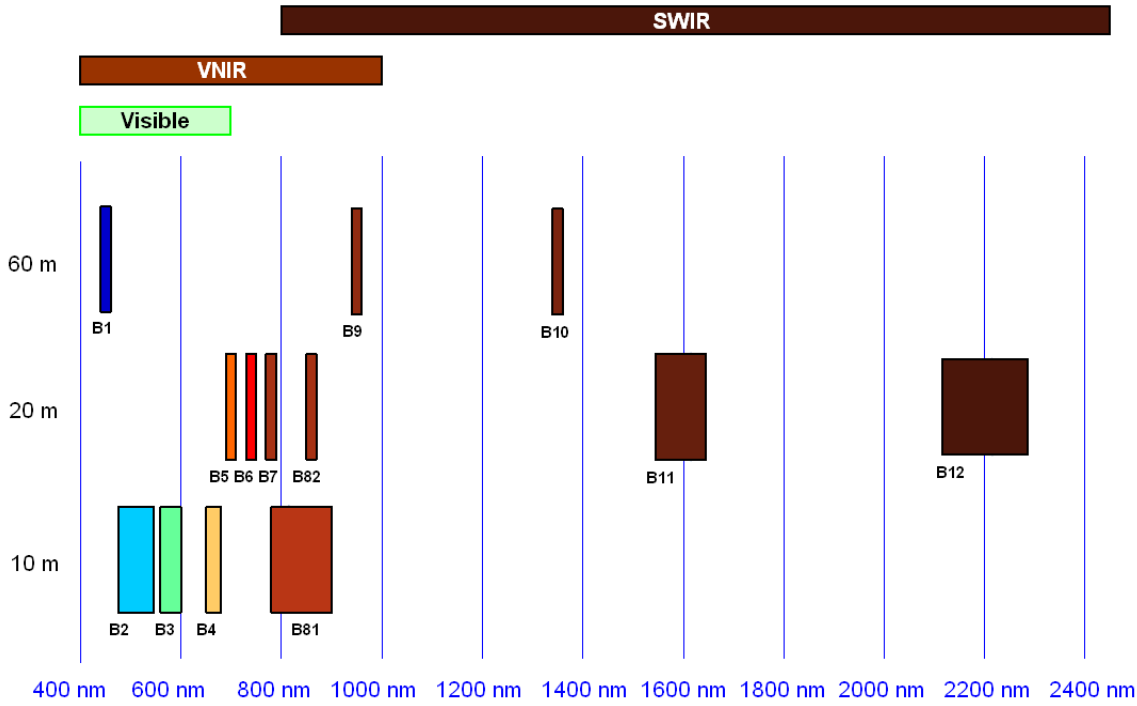

Figure 2-1 – S2/MSI spectral bands and resolutions

The three 10 m bands in the visible region enable true colour images with a high spatial resolution, which is especially important for urban areas. The 10 m wide NIR band also allows a 10 m false colour infrared (CIR) composite. The spectral bands needed to retrieve atmospheric parameters are designed with a coarser resolution of 60 m (channels at 443 nm, 940 nm, 1375 nm) which is justified because aerosol, water vapour, and cirrus contents usually do not vary rapidly within a scale of 100 m. The remaining channels have a spatial resolution of 20 m. Figure 2-2 shows the normalized spectral filter functions of the Sentinel-2 bands together with a typical atmospheric transmittance curve (grey). All VNIR bands are influenced by aerosol scattering (hull of the transmittance curve), the signal in bands 1 -3 is influenced by ozone absorption, band 5 slightly depends on the atmospheric water vapour column, band 7 on oxygen absorption, and band 9 measures the water vapour absorption depth. The sensor characteristics are summarized in Figure 2-2.

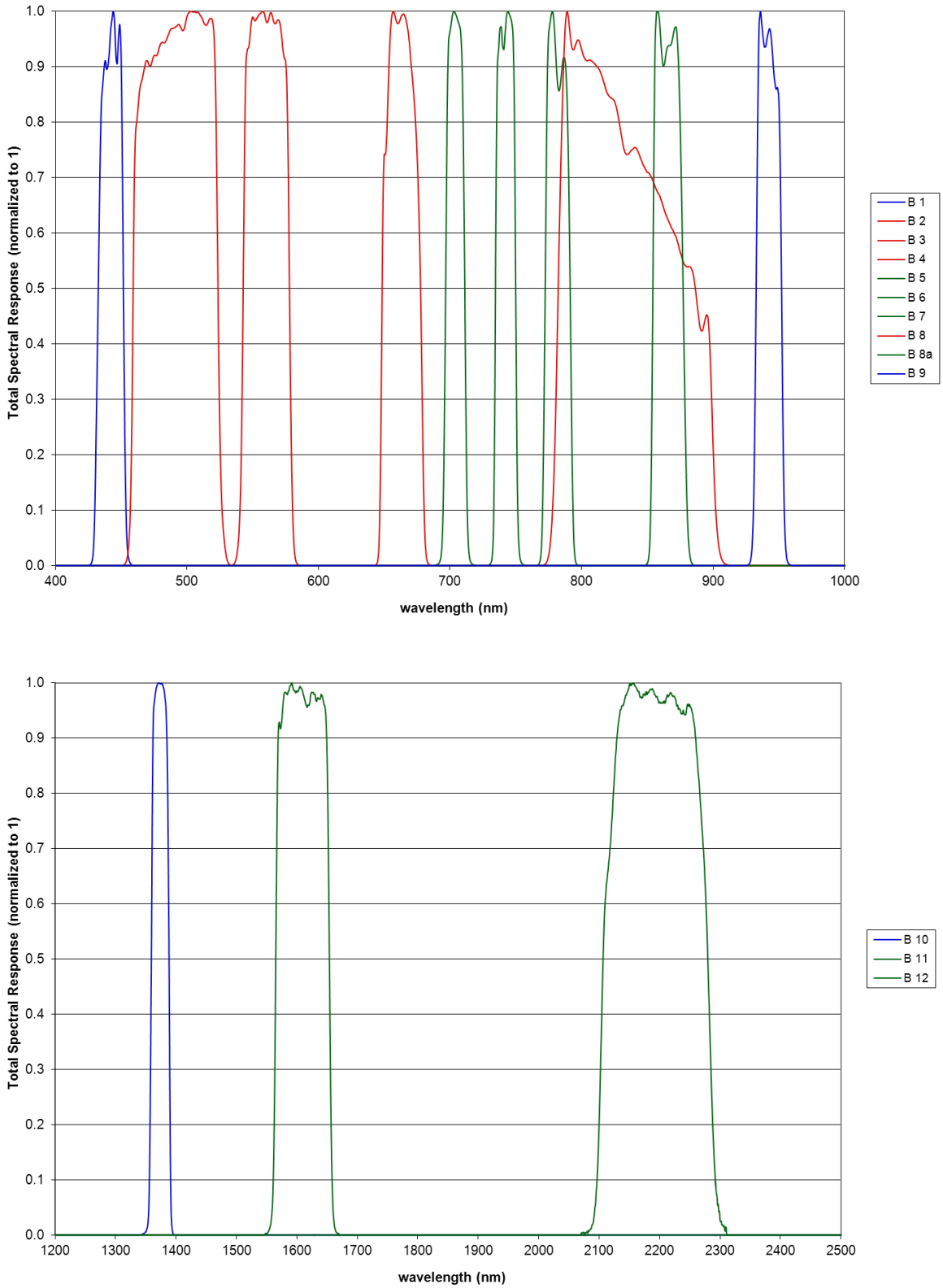

Figure 2-2 – Sentinel-2 filter curves and atmospheric transmittance

Table 2-I – Spectral bands of Sentinel-2 and spatial resolution and its purpose (based on ESA's spectral response functions from January 2009)

Band	Center λ (nm)`	Spectral Width Δλ (nm)	Spatial Re-solution (m)	Purpose in L2A processing context
B1	443	20	60	Atmospheric Correction
B2	490	65	10	Sensitive to Vegetation Aerosol Scattering
B3	560	35	10	Green peak, sensitive to total chlorophyll in vegetation
B4	665	30	10	Max Chlorophyll absorption
B5	705	15	20	Not used in L2A context
B6	740	15	20	Not used in L2A context
B7	783	20	20	Not used in L2A context
B8	842	115	10	Leaf Area Index (LAI)
B8a	865	20	20	Used for water vapour absorption reference
B9	945	20	60	Water Vapour absorption atmospheric correction
B10	1375	30	60	Detection of thin cirrus for atmospheric correction
B11	1610	90	20	Soils detection
B12	2190	180	20	AOT determination

2.2 Input data

All input data of the processor are listed in section 2.1.1 (Input Data) of the according Product Definition Document [S2-L2A-PDD].

2.3 Output data

All output data of the processor are listed in section 2.1.2 (Product Summary) of the according Product Definition Document [S2-L2A-PDD].

2.4 Processing Strategy

Defective, non-existing and saturated pixels have to be excluded from the processing steps. Saturated pixels may disturb the calculation of the spectral band ratios and the actual meaning of the thresholds of the scene classification. Therefore they have to be identified and isolated from the algorithm before the computation of the spectral ratios. When L1C data is re-projected on tiles (see figure below) it may occur that on the borders of the acquisition, data is missing on the tile. These non-existing data have also to be excluded from the processing.

Figure 2-3 – Level-1C data re-projection on tiles

It is anticipated that the Sentinel-2 product will be less affected by saturation problems.

Non-existing, defect and saturated pixels are classified in ahead and collected in two separate classes of the scene classification algorithm (two new classes are proposed at the begin of the columns). They are not used for further processing.

All algorithms described in this document are performed on a per-pixel basis. As the channels used in the two algorithms have different resolutions (see Table 2-1) parts of the channels need to be resampled[2]. It is obvious, that the precision of the algorithms is always dependent on the lowest resolution provided.

From an atmospheric correction point of view, the Sentinel-2 data processing could be performed to obtain a 60 m, a 20 m and a 10 m surface reflectance product.

The recommended baseline processing is the rural/continental aerosol type, but it can also be specified according to geography and climatology. However, a change of the aerosol type between successive scenes may cause brightness steps in the BOA reflectance at scene borders and should be avoided.

The AOT map is calculated using dark reference areas at 60 m resolution (see below). The results are smoothed with a moving window of 3 km × 3 km. There are two reasons for the low-pass filtering: (i) to suppress noise, and (ii) to smooth the influence of biome-dependent fluctuations of the spectral band correlation coefficient.

Water Vapour retrieval is calculated with the band 8a (865 nm, the 20 m spatial resolution resampled to 60 m) and band 9 (945 nm, 60 m resolution).

Haze removal would require a full scene processing without tiles.

In the current approach processing is performed on tile level. An extension of the algorithm for continuous data strips is given in APPENDIX A. This shall be implemented after its feasibility is demonstrated.

[2] *Cubic spline method*

2.4.1 The 60 m Product

For the 60 m product, all bands need to be resampled to 60 m. A complete AOT, water vapour, cirrus, and surface reflectance retrieval can then be performed for the 60 m data. In the final 60 m reflectance cube the cirrus channel should be omitted (as it does not represent surface information).

Input to the atmospheric correction on the 60 m product is the coarse pre-classification (as is specified in Chapter 3 and a data file with 12 bands on tile level (all bands except the wide10 m resolution NIR band, B8). The 10 m and 20 m data are resampled to 60 m. In mountainous terrain, additionally a 60 m resolution DEM is needed, which must be resampled from the 90 m. The DEM itself in not provided within the product, but only given as a reference within the Auxiliary Data Block of the Level-1C input data (see section 2.1.1 of [S2-L2A-PDD]).

2.4.2 The 20 m Product

Input to the 20m product is the pre-classification (land, water, cloud and snow/ice) map, either updated with the 20 m resolution bands and a 20 m resolution DEM in case of mountainous terrain (recommended) or resampled from the 60 m product. Additional input can be the maps of AOT (60 m) and water vapour WV (60 m) calculated in the first run, which has to be resampled to yield AOT (20 m) and WV (20 m). Then, no separate AOT (20 m) / WV (20 m) retrievals are necessary. The alternative is a recalculation of the AOT (20 m) with the 20 m bands.

If the haze removal option would be set, then an updated AOT retrieval with the 20 m channels would be mandatory. In this case, an updated pre-classification based on the 20 m bands is recommended to obtain a higher accuracy land/water map which is used during de-hazing. Haze removal is switched off if no pre-classification file exists.

WV (20m) tests should be performed in order to decide whether WV (20m) should be resampled from WV (60m) or updated using band 8a data (865nm, with the original 20 m resolution) and band 9 (945 nm) data resampled to 20 m. An analysis of the behaviour of the BOA reflectance spectra at 945 nm (possible spike artefacts) will indicate which method performs better.

Although the internal calculation will be performed with 12 bands (the 60 m data resampled to 20 m, and the 10 m data resampled to 20 m) it is recommended to omit the original 60 m channels in the final BOA reflectance product to avoid spectral artefacts due to mixed signatures and resampling, so the recommended final product will consist only of 9 channels.

2.4.3 The 10 m Product

This processing involves four channels (B2, B3, B4, B8, i.e., blue, green, red, broad-band NIR). Input is the previously calculated AOT (60 m) or AOT (20 m) which has to be resampled to get AOT (10 m) and a 10 m resolution DEM in rugged terrain. So no AOT retrieval is performed here and the resampled AOT (10 m) is free of tile border effects.

As the water vapour influence is very small (band 8 is affected a little) the scene-average water vapour can be used during the surface reflectance retrieval to specify the LUT file name with the nearest water vapour column. Example: the scene-average value is 1.4 cm, and LUTs are provided for water vapour columns of 0.4, 1.0, 2.0, 2.9, 4.0, and 5.0 cm. Then the LUT file name corresponding to 1.0 cm is specified in the input parameter file.

Surface reflectance retrieval is conducted with a known AOT and water vapour. It should be aware that small surface reflectance brightness steps at tile borders might occur

because of the adjacency effect. They have to be accepted as long as processing on tile base is technically unavoidable (see APPENDIX A for improvement of the algorithm).

A pre-classification file resampled to 10 m is only required if the haze removal option would be set. If this file does not exist, the option is switched off.

2.4.4 Summary

Figure 2-4 shows a schematic sketch of the proposed L2A processing on tile level.

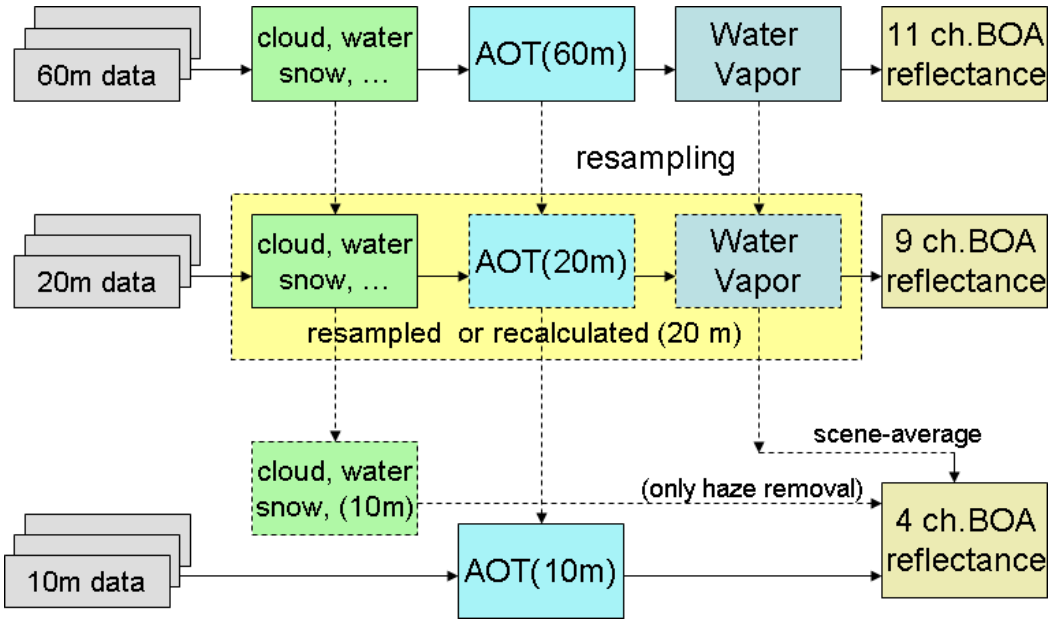

Figure 2-4 – Schematic sketch of processing the 60 m, 20 m, and 10 m data of Sentinel-2

A topographic correction is recommended if more than 5% (or 1% TBD) of the pixels have slopes > 8° or > 6° (TBD). Otherwise, the terrain can be considered as flat using the average elevation which decreases the processing time by a factor of 3 to 4. Justification for the > 8° slope criterion: for a typical solar zenith angle of θs = 40° this approximately corresponds to a 10% variation of the direct local solar irradiance (i.e., cos(θs)/cos(θs – 8) = 0.90).

Haze removal is not part of the baseline processing. If this option is selected, it requires a processing of the complete scene, not tiles, in order to avoid brightness steps at tile borders.

3. SCENE CLASSIFICATION

3.1 Overview

The algorithm of chapter three shall be suitable to detect clouds, snow and cloud shadows and to generate a classification map, which consists of 4 different classes for clouds (including cirrus), together with six different classifications for shadows, cloud shadows, vegetation, soils / deserts, water and snow. Input data for this part is the level 1C product, i.e. TOA reflectance measured at 60-meter resolution.

Associated quality indicators on snow and cloud probability are additionally provided. These Quality indicators calculate the probability (0-100%) that the earth surface is obstructed by clouds or optically thick aerosol.

Operational constraints have driven the design of this algorithm. The need for several algorithms to first determine if the pixel is cloudy or clear (e.g. atmospheric correction, mosaics) imposes to the cloud detection algorithm to be fast and efficient, limiting the use of CPU-intensive algorithms.

The algorithm uses the reflective properties of scene features to establish the presence or absence of clouds in a scene.

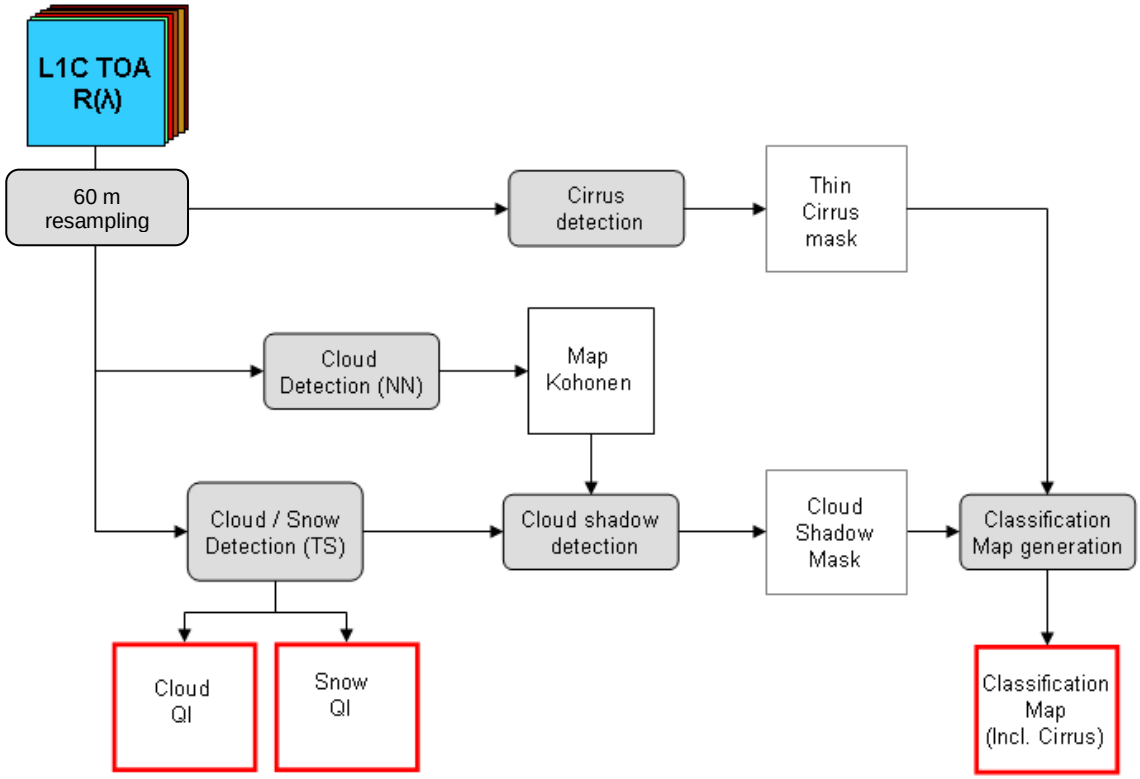

Figure 3-1 – Overview of the different processing modules (grey) and outputs (red) (NN: Neural Network, TS: ThreShold algorithm)

Figure 3-1 gives an overview of the different processing modules of the cloud detection and classification map algorithm. The modules are shown in grey and the final outputs are shown in red.

The Cloud/Snow detection (TS) algorithm is detailed in section 3.2. The Cirrus detection algorithm is described in section 3.3. The Cloud shadow detection algorithm is presented in 3.4. The classification map generation is explained in 3.5 and the Kohonen map generation by a neural network is described in APPENDIX A.

3.2 Cloud / Snow detection algorithm

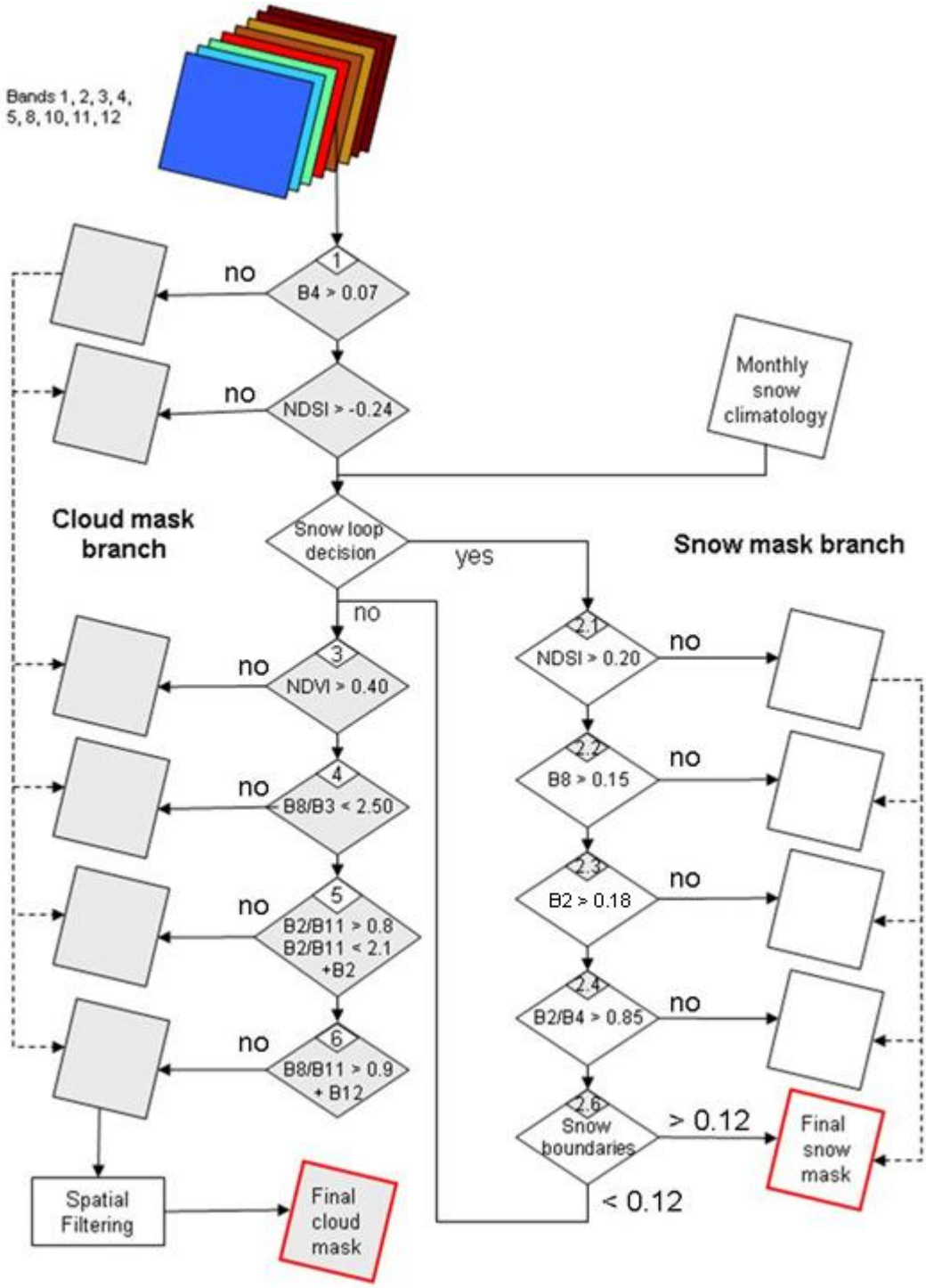

Figure 3-2 – Cloud Detection Algorithm sequential steps

Potential cloudy pixels are identified by a first filtering in the red region of the solar spectrum. Then all these potentially cloudy pixels undergo a sequence of filtering based on spectral bands thresholds, ratios and indexes computations (NDSI, NDVI). The result of each pixel test is a cloud probability (ranging from 0 for high confidence clear sky to 1 for high confidence cloudy). After each step the cloud probability of a potentially cloudy pixel is updated by multiplying the current pixel cloud probability by the result of the test. Finally the cloud probability of a pixel is the product of all the individual tests.

For performance reasons the sequential filtering of a potentially cloudy pixel stops when a test result set its cloud probability to zero. The pixel is then considered to be high confidence clear sky in the cloud probability map and the pixel is finally classified to its corresponding class map shown in Table 3-I.

The Figure 3-3 a above presents the sequential steps of the cloud / snow detection module.as a flow diagram. Details on the foundation for the chosen thresholds are given by references [58], [59] in Appendix C.

3.2.1.1 Step 1a - Brightness thresholds on red (Band 4)

The first step of the algorithm is to discard pixels that fall under a certain reflectance threshold in the red region of the solar spectrum.

Each band 4 pixel in the scene is compared to two brightness thresholds. Pixels that fall below the lower brightness threshold have their cloud probability set to 0.0 and are identified as non-clouds and classified as dark pixels in the classification map. Pixels that exceed the upper brightness threshold have their cloud probability set to 1.0 and are passed to step 2. Pixels that have their brightness between these two thresholds have their cloud probability calculated linearly from 0.0 to 1.0 as shown in Figure 3-4 and are passed to step 1b.

Current thresholds: T1 = 0.07; T2 = 0.25

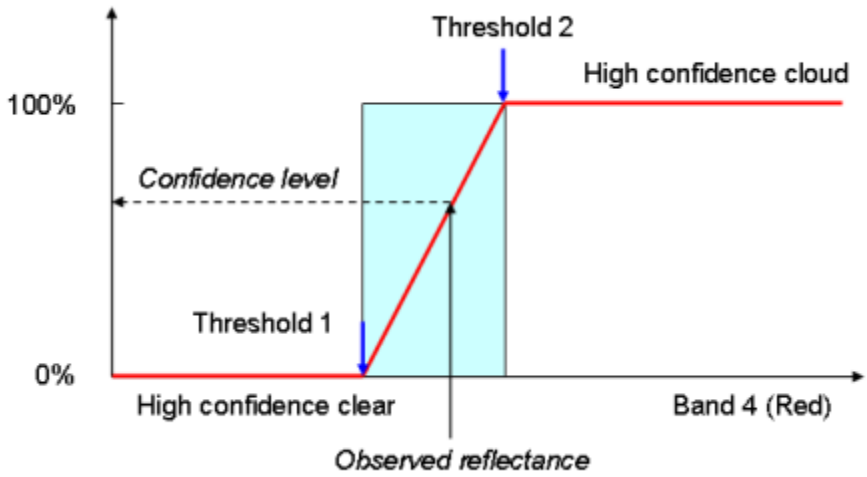

Figure 3-4 – Step 1 confidence level

3.2.2 Step 1b – Normalized Difference Snow Index (NDSI)

Most of potential cloudy pixels have NDSI values located between -0.1 and 0.2 so pixels with strong NDSI negative values could be discarded whereas others continue the algorithm path.

Pixels values from spectral bands 3 and 11 are used to formulate the normalized difference snow index (NDSI). The NDSI filter is expressed as:

NDSI = (band 3 – band 11) / (band 3 + band 11)

Each pixel NDSI value in the scene is compared to two NDSI thresholds. Pixels that fall below the lower brightness threshold have their cloud probability set to 0.0 and are identified as non-clouds and classified as dark pixels in the classification map. Pixels with NDSI that exceed the upper brightness threshold have their cloud probability set to 1.0 and are passed to step 2. Pixels that have their NDSI values between these two thresholds have their cloud probability calculated linearly from 0.0 to 1.0 (as shown in Figure 3-4), then multiplied by the precedent snow probability from step 1a and passed to step 2.

Current thresholds: T1 = -0.24; T2 = -0.16

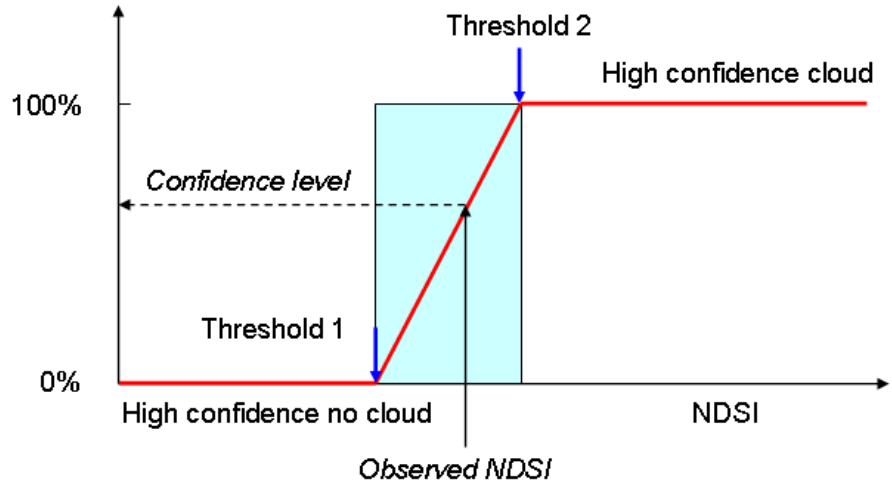

Figure 3-5 – Step 1b confidence level

3.2.3 Step 2 – Snow detection – Snow confidence mask

The objective of this step is to detect snow pixels and to create a snow confidence mask. It consists of four successive filters using pixels values from spectral bands 2, 3, 8 and 11.

The entry into the snow detection branch of the algorithm is conditioned by auxiliary information about snow. Monthly snow probability is associated to each pixel and a threshold decides the entry into the snow detection loop. This step helps to limit false snow detection in icy clouds.

Normalized Difference Snow Index (NDSI) and a successive set of filters and ratios are used to determine the probability that a pixel is covered by snow. The output of the snow detection loop is a snow confidence mask.

An additional processing step is performed in section 3.2.3.6 to limit the cloud false detection around the snow regions boundaries.

3.2.3.1 Snow climatology condition – The entry into snow detection loop

In order to help to discard false snow detections due to high altitude clouds that behave like snow or ice cover, auxiliary data shall be used in order to determine whether the snow detection algorithm for a particular scene shall be started. For this purpose yearly snow climatology data shall be assembled, which can be derived from the MODIS snow climatology database, putting together a map of the areas where no snow was detected during the past ten years (2000-2010). Figure 3-6 shows two examples of such no-snow areas in black. This long term no-snow area has to be collected and provided as another auxiliary input data, as described for Table 2-1 in [S2-L2A-PDD].

Each pixel is compared to this snow climatology map. If the pixel belongs to a “no-snow” area, the pixel does not enter the snow detection loop and pass to the successive cloud detection filters. If the pixel does not belong to a “no-snow” area then it enters the snow detection loop.

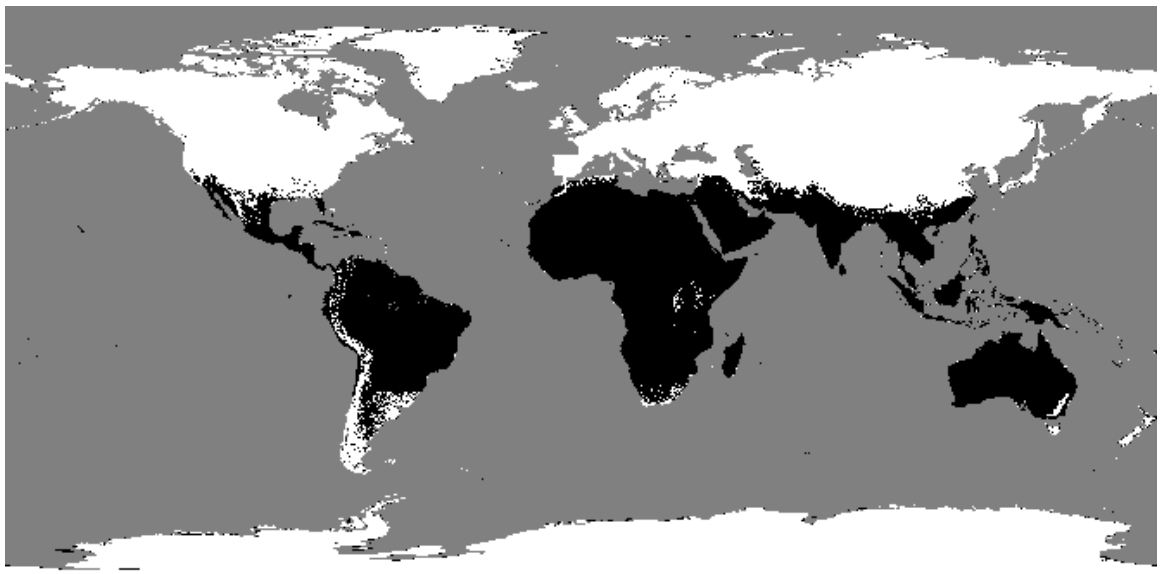

Figure 3-6 – Snow climatology map
(Black = no snow on land during the last 10 years) © MODIS

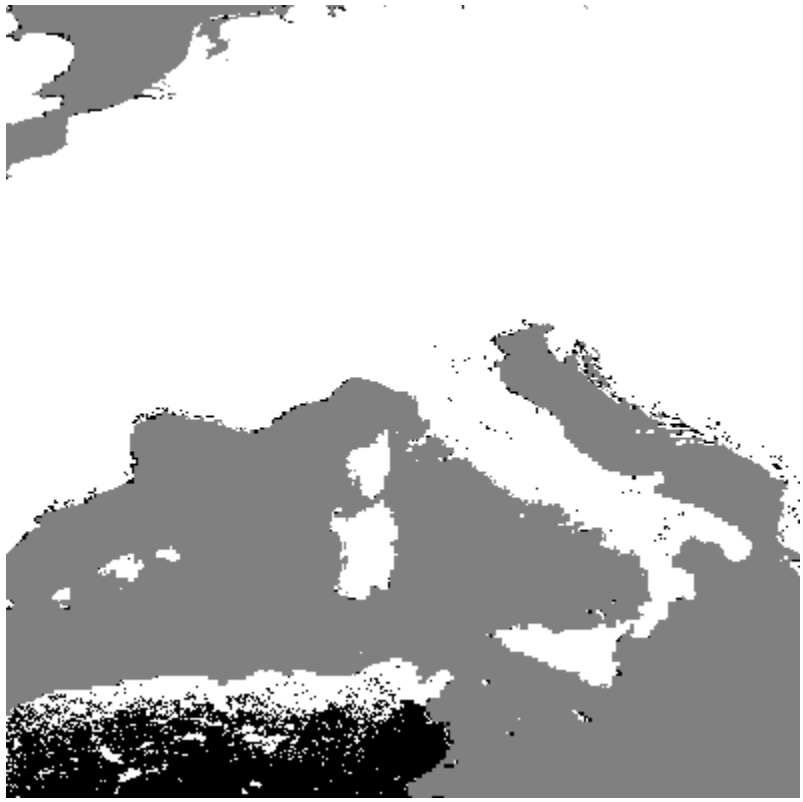

Figure 3-7 – Snow climatology map zoom over Italy
(Black = no snow on land during the last 10 years) © MODIS

Figure 3-7 is a close-up of Figure 3-6 over Mediterranean Sea and Italy to illustrate that no seldom snow event should be missed over this region due to the use of a snow climatology map.

3.2.3.2 Snow filter 1: Normalized Difference Snow Index (NDSI)

Pixels values from spectral bands 3 and 11 are used to formulate the normalized difference snow index (NDSI). The NDSI filter is expressed as:

NDSI = (band 3 – band 11) / (band 3 + band 11)

This filter is particularly useful for eliminating snow. The reflectance of clouds and snow is similar in band 3. However, in band 11, reflectance for clouds is very high while for snow it is low. Hall discovered that NSDI values greater than 0.4 represent snow cover quite well. Two thresholds are set for the NDSI. NDSI values that fall below the lower threshold have their snow probability set to 0.0 and are identified as non-snow. NDSI values that exceed the upper threshold have their snow probability set to 1.0 and are passed to the snow filter 2. Pixels that have their brightness between these two thresholds have their snow probability calculated linearly from 0.0 to 1.0 and are passed to snow filter 2.

Current thresholds: T1 = 0.20; T2 = 0.42

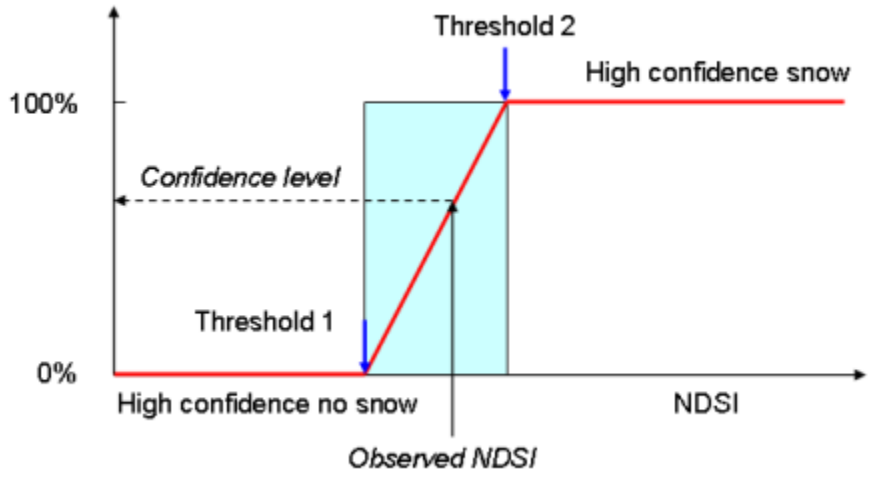

Figure 3-8 – Step 2 – Snow filter 1 confidence level

3.2.3.3 *Snow filter 2: Band 8 thresholds*

This filter eliminates regions that have high NDSI values but low reflectance in Band 8 (Near Infrared.)

Band 8 pixel values are compared to two brightness thresholds. Pixels that fall below the lower threshold have their snow probability set to 0.0 and are identified as non-snow. Pixel values that exceed the upper threshold have their snow probability that remains unchanged and are passed to the snow filter 3. For pixels that have a value between these two thresholds, a snow probability is computed linearly from 0.0 to 1.0 and multiplied by their precedent snow probability. This new snow probability is stored in the snow confidence mask. These pixels are passed to the snow filter 3.

Current thresholds: T1 = 0.15; T2 = 0.35

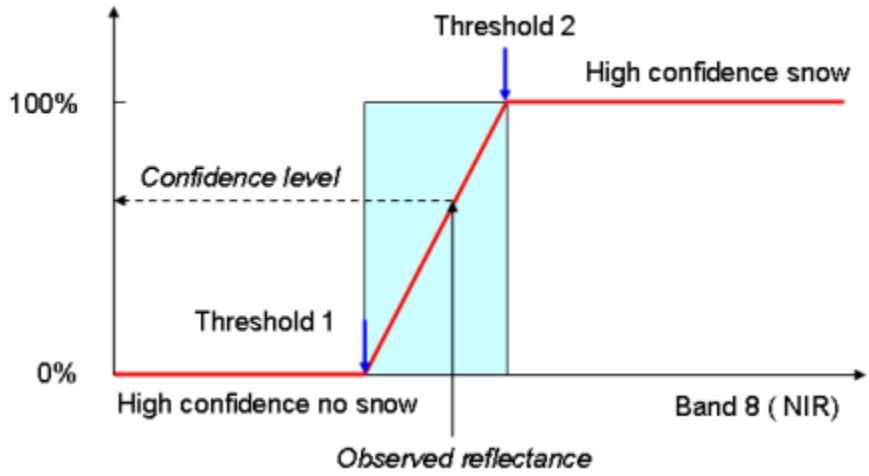

Figure 3-9 – Step 2 – Snow filter 2 confidence level

3.2.3.4 *Snow filter 3: Band 2 thresholds*

This filter eliminates regions that have high NDSI values but low reflectance in Band 2 (Blue).

Band 2 pixel values are compared to two brightness thresholds. Pixels that fall below the lower threshold have their snow probability set to 0.0 and are identified as non-snow. Pixel values that exceed the upper threshold have their snow probability that remains unchanged and are passed to snow filter 4. For pixels that have a value between these two thresholds, a snow probability is computed linearly from 0.0 to 1.0 and multiplied by their precedent snow probability. This new snow probability is stored in the snow confidence mask. These pixels are passed to the snow filter 4.

Current thresholds: T1 = 0.18; T2 = 0.22

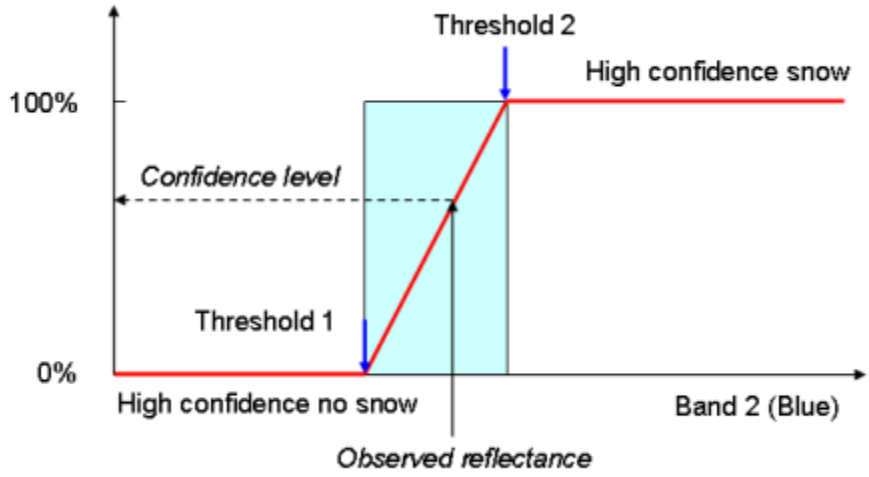

Figure 3-10 – Step 2 – Snow filter 3 confidence levels

3.2.3.5 Snow filter 4: Ratio Band 2 / Band 4

This filter eliminates regions that have high NDSI values but low B2/B4 ratio like some water bodies.

Two thresholds are set for the B2/B4 ratio. B2/B4 ratio values that fall below the lower threshold have their snow probability set to 0.0 and are identified as non-snow. B2/B4 ratio values that exceed the upper threshold have their snow confidence that remain unchanged and are passed to the following step. For pixels that have a B2/B4 ratio between these two thresholds, a probability is computed linearly from 0.0 to 1.0 and multiplied by their precedent snow probability. This new snow probability is stored in the snow confidence mask.

All the pixels that have a snow confidence value higher than 0 are passed to the step 5.

Current thresholds: T1 = 0.85; T2 = 0.95

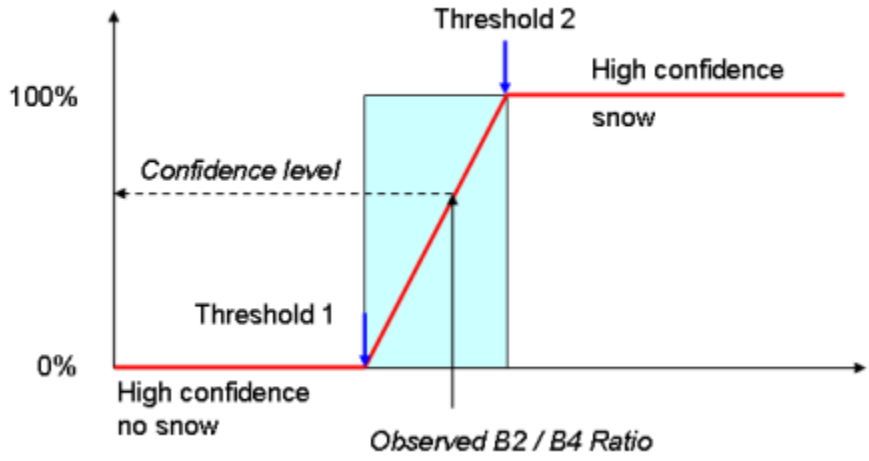

Figure 3-11 – Snow filter 4 confidence levels

3.2.3.6 Snow filter 5: Processing of snow boundaries zones

This step helps to remove false cloud detection at the boundaries of a snowy region, where mixed pixel (snow + ground) could be detected as cloud in the cloud detection algorithm.

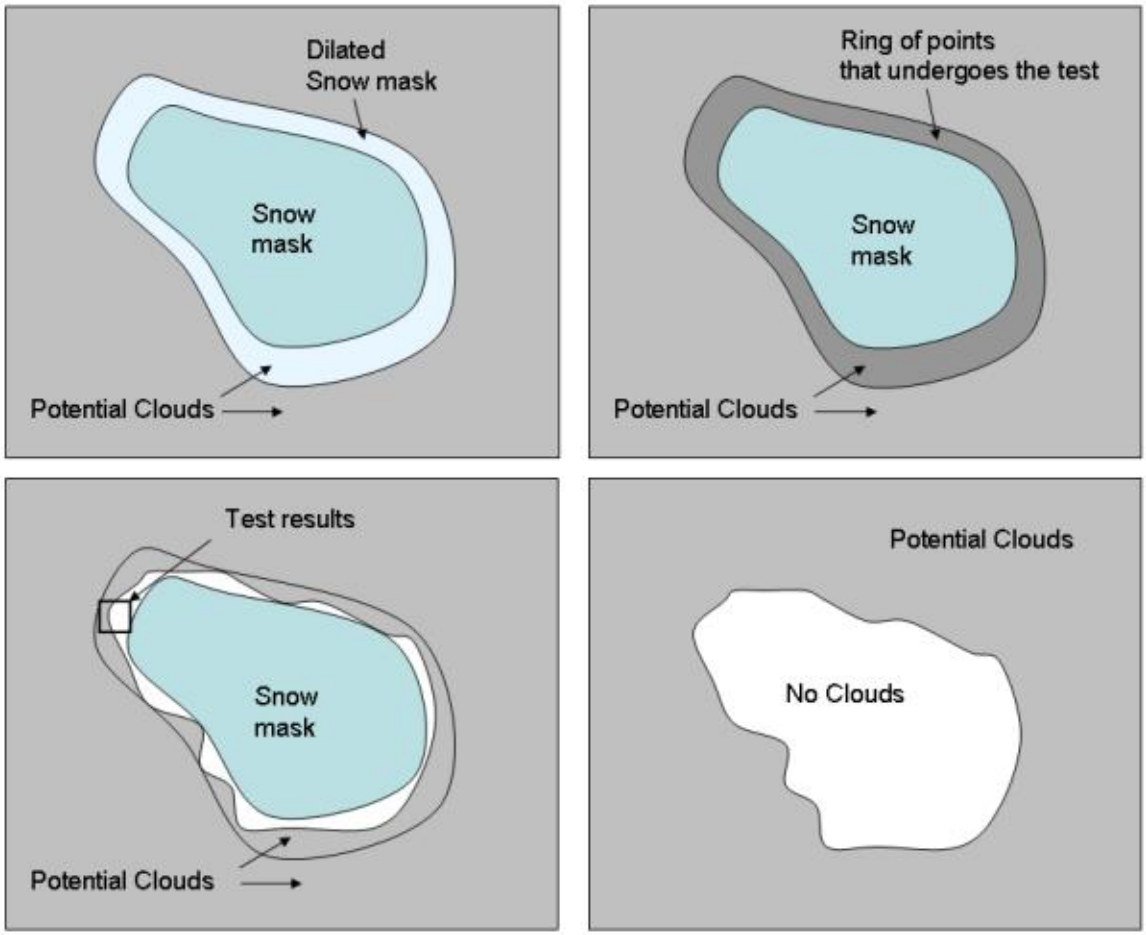

Figure 3-12 – Snow boundary region filtering

A "DILATE[3]" operator is used to determine a boundary zone (ring of pixels around a snowy region) on which a brightness test on Band 12 is performed.

Pixel values of band 12 that fall below a threshold of 0.25 have their snow confidence that remain unchanged. Pixels that exceed the threshold have their snow probability set to 0.0 and are identified as non-snow.

The result of this processing step is to extend the detected snow mask in a controlled manner to avoid cloud over-detection on partially snowy pixels.

3.2.3.7 End of snow detection loop

The pixels that have a snow probability that fall below a threshold of 0.12 are passed to the next cloud detection step whereas pixels that have their snow probability higher than this threshold are classified as snowy pixels in the classification map.

3.2.4 Step 3 – Normalized Difference Vegetation Index (NDVI)

Two filters are used to identify vegetation pixel, the Normalized Difference Vegetation Index (NDVI) and a reflectance ratio (B8/B3 - NIR/green) for senescing vegetation.

Pixels values from spectral bands 8 and 4 are used to formulate the normalized vegetation index (NDVI). The NDVI filter is expressed as:

NDVI = (band 8 – band 4) / (band 8 + band 4)

This filter is particularly useful for eliminating highly reflective vegetation. In the near-infrared (band 8), reflectance for green leaves is high because very little energy is absorbed. In the red region (band 4), the chlorophyll in green leaves absorbs energy so reflectance is low. The NDVI results in higher values for vegetation than for other scene features, including clouds. Two thresholds are set for the NDVI. NDVI values that exceed the upper threshold have their cloud probability set to 0.0 and are identified as non-cloud and classified as vegetation pixels in the classification map. NDVI values that fall below the lower threshold have their cloud confidence that remain unchanged and are passed to the fourth step. For pixels that have a NDVI value between these two thresholds, a probability is computed linearly from 1.0 to 0.0 and multiplied by their precedent cloud probability. This new cloud probability is stored in the cloud confidence mask.

Current thresholds: T1 = 0.36; T2 = 0.40

[3] *Dilation is a mathematical morphology method in order to gradually enlarge the boundaries of regions of foreground pixels. Areas of foreground pixels grow in size while holes within those regions become smaller. Details for application of the operator can be found e.g. in:*

http://idlastro.gsfc.nasa.gov/idl_html_help/DILATE.html#wp1002920

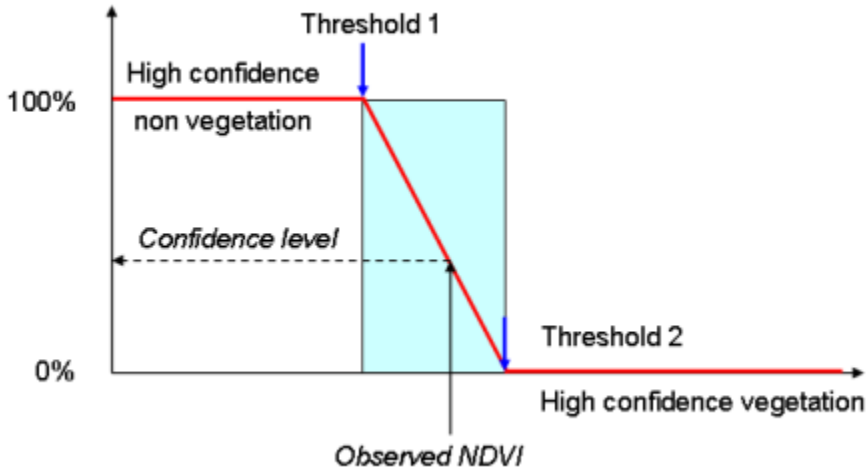

Figure 3-13 – Step 3 confidence level

All the pixels that have a cloud confidence value higher than 0 are passed to the step 4.

3.2.5 Step 4 – Ratio Band 8 / Band 3 for senescing vegetation

This filter eliminates highly reflective senescing vegetation and is formed by dividing the band 8 reflectance by the band 3 reflectance. In the near-infrared (band 8), green leaves that are dead or dying absorb even less energy and are thus highly reflective. In the green region (band 3), the leaves absorb less energy because of chlorophyll loss and exhibit increased reflectivity. The B8/B3 ratio values are higher for vegetation than other scene features including clouds.

Two thresholds are set for the B8/B3 ratio. B8/B3 ratio values that exceed the upper threshold have their cloud probability set to 0.0 and are identified as non-cloud and classified as vegetation pixels in the classification map. B8/B3 ratio values that fall below the lower threshold have their cloud confidence that remain unchanged and are passed to the fifth step. For pixels that have a B8/B3 ratio between these two thresholds, a probability is computed linearly from 1.0 to 0.0 and multiplied by their precedent cloud probability. This new cloud probability is stored in the cloud confidence mask.

Current thresholds: T1 = 1.50; T2 = 2.50

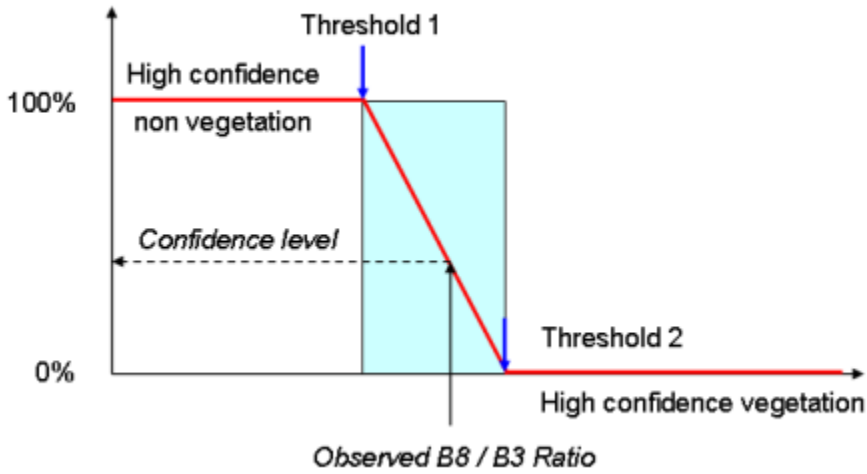

Figure 3-14 – Step 4 confidence level

All the pixels that have a cloud confidence value higher than 0 are passed to the step 5.

3.2.6 Step 5 – Ratio Band 2 / Band 11 for soils and water bodies

Bare soils pixels are detected when their reflectance ratio (blue/infrared, B2) fall below a threshold. An additional variable offset threshold in the infrared region (B12) is added to detect thin cloud over soils.

Bright water lakes waters pixels are identified when their reflectance ratio (blue/infrared, B2/B11) exceed a threshold. An additional variable offset threshold in the blue region is added to detect thin cloud over inland waters.

3.2.6.1 Pass 1 for soils detection

The pass1 eliminates different types of soils. It is formed by dividing the reflectance of band 2 by the reflectance of band 11. The B2/B11 ratio values are lower for soils than other scene features including clouds.

The entry into this test is conditioned by threshold on pixel value in Band 2. The pixel enters the test only if its value in Band2 is lower than a threshold that varies linearly in function of B2/B11 ratio. The lower is the B2/B11 ratio (higher probability to be a soil pixel) the lower is the threshold to enter the test and vice versa. It helps to keep thin clouds detection over soil regions.

For the pass 1, two thresholds are set for the B2/B11 ratio. B2/B11 ratio values that fall below the lower threshold have their cloud probability set to 0.0 and are identified as non-cloud and classified as soil pixels in the classification map. B2/B11 ratio values that exceed the upper threshold have their cloud confidence that remain unchanged and are passed to the step 5 pass 2. For pixels that have a B2/B11 ratio between these two thresholds, their precedent cloud probability is multiplied by a probability computed linearly from 0.0 to 1.0. This new cloud probability is stored in the cloud confidence mask. These pixels are passed to the step 5 pass 2.

3.2.6.2 Pass 2 for water bodies detection

This filter pass 2 eliminates different types of water bodies and is formed by dividing the band 2 reflectance by the band 11 reflectance. The B2/B11 ratio values are higher for water bodies than other scene features including clouds.

The entry into this test is conditioned by threshold on pixel value in Band 12. The pixel enters the test only if its value in Band 12 is lower than a threshold that varies linearly in function of B2/B11 ratio. The higher is the B2/B11 ratio (higher probability to be a water body pixel) the higher is the threshold to enter the test and vice versa. It helps to keep thin clouds detection over soil regions.

Two thresholds are set for the B2/B11 ratio pass 2. B2/B11 ratio values that exceed the upper threshold have their cloud probability set to 0.0 and are identified as non-cloud and classified as water pixels in the classification map. B2/B11 ratio values that fall below the lower threshold have their cloud confidence that remain unchanged and are passed to the step 6. For pixels that have a B2/B11 ratio between these two thresholds, their precedent cloud probability is multiplied by a probability computed linearly from 0.0 to 1.0. This new cloud probability is stored in the cloud confidence mask.

All the pixels that have a cloud confidence value higher than 0 are passed to the step 6.

Current thresholds: T11 = 0.55; T12 = 0.80; T21 = 2.1; T22 = 4.0

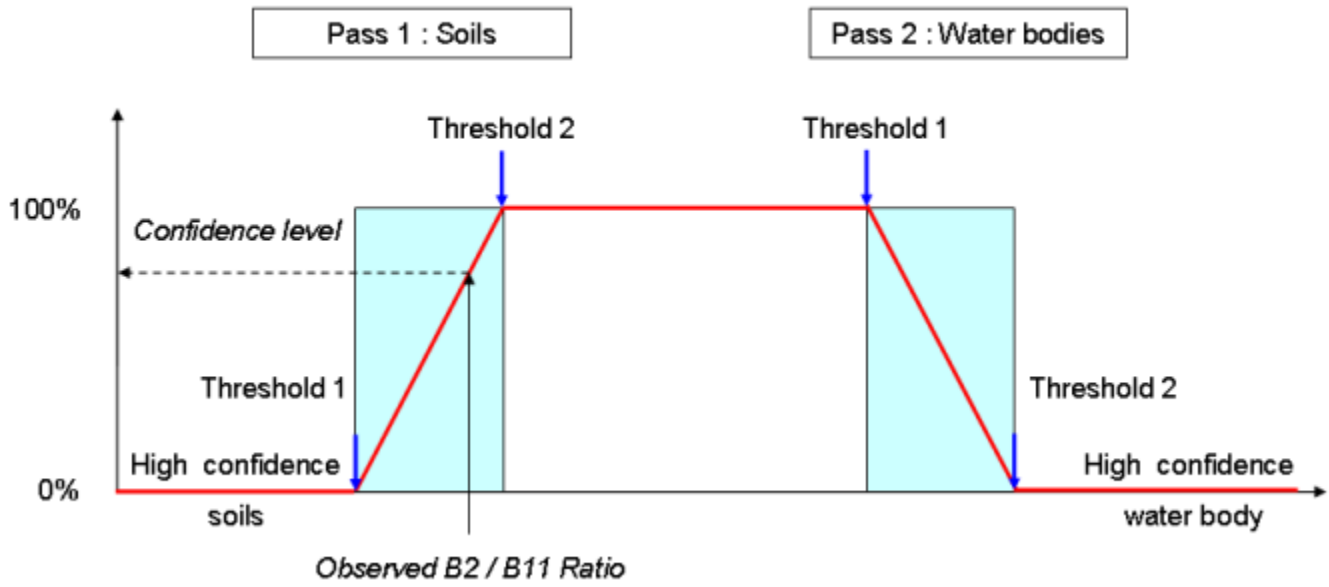

Figure 3-15 – Step 5 – Pass 1 & Pass 2 confidence level

3.2.7 Step 6 – Ratio Band 8 / band 11 for rocks and sands in deserts

This filter eliminates highly reflective rocks and sands in desert landscapes and is formed by dividing the band 8 reflectance by the band 11 reflectance. Rocks and sand tend to exhibit higher reflectance in band 11 than in band 8, whereas the reverse is true for clouds.

Two thresholds are set for the B8/B11 ratio. B8/B11 ratio values that fall below the lower threshold have their cloud probability set to 0.0 and are identified as non-cloud and classified as soil/desert in the classification map. B8/B11 ratio values that exceed the upper threshold have their cloud confidence that remain unchanged and are passed to step 7. For pixels that have a B8/B11 ratio between these two thresholds, a probability is computed linearly from 0.0 to 1.0 and multiplied by their precedent cloud probability. This new cloud probability is stored in the cloud confidence mask.

All the pixels that have a cloud confidence value higher than 0 are passed to the step 7.

Current thresholds: T1 = 0.90; T2 = 1.10

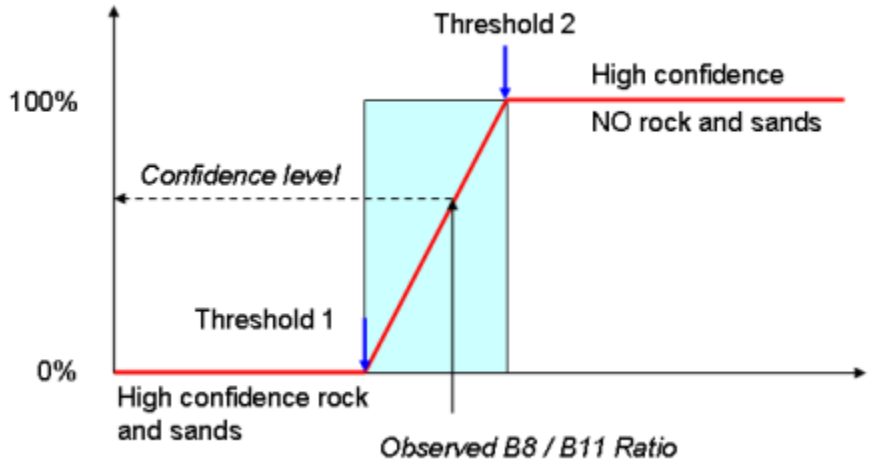

Figure 3-16 – Step 6 confidence level

3.2.8 Step 7 – Spatial filtering

At this stage of the algorithm a cloud confidence mask and a snow confidence mask are available.

An optional spatial filtering is proposed to take into account the slight misregistration of S2 spectral bands at the altitude of clouds. Indeed S2 spectral bands are co-registered at ground level with the use of a digital elevation model. The spatial filtering helps also to reduce false cloud detection that occurs on the borders of highly contrasted regions like river contours or shorelines.

It consists in applying a median filter[4] followed by a dilatation[5] operator to the final cloud mask. The kernel size of the filters could be 3x3 or 5x5 depending on the level of artefacts reduction desired.

This spatial filtering is done for the generation of the three cloud classes and the thin cirrus class in the classification map.

3.3 Cirrus cloud detection algorithm

3.3.1 Sentinel-2 band 10 (1.38 µm) thresholds

Cirrus cloud detection will rely on **Sentinel-2 band 10 (1.375 µm)** reflectance thresholds on a per pixel basis to detect the presence of thin cirrus cloud in the upper troposphere under daytime viewing conditions.

The strength of this cloud detection channel lies in the strong water vapour absorption in the 1.38 µm region (Gao et al., 1993). With sufficient atmospheric water vapour present (estimated to be about 1 cm precipitable water) in the beam path, no upwelling reflected

[4] *The median filter compares each pixel with its nearby neighbours in order to decide whether or not it is representative of its surroundings. Instead of simply replacing the pixel value with the* mean *of neighbouring pixel values, it replaces it with the* median *of those values. The median is a more robust average than the mean so that single very unrepresentative pixels will not affect the resulting value significantly.*

[5] *See Footnote 2 for explanation.*

radiance from the earth's surface reaches the satellite. This means that much of the earth's surface will be obscured in this channel. (However not the entire earth's surface as precipitable water is often less than 1 cm over polar regions, in midlatitude winter regions, and in high elevation regions).

With relatively little of the atmosphere's moisture located high in the troposphere, high clouds appear bright in the S-2 Band 10. Reflectance from low and mid level clouds is partially attenuated by water vapour absorption.

Simple low and high reflectance (normalized by incoming solar at the top of the atmosphere) thresholds are used to separate thin cirrus from clear sky and thick cloud scenes. If the reflectance exceeds the clear-sky threshold and is below the thick cloud treshold, then thin cirrus are detected. We subjectively define thin cirrus as a cloud that has a small impact on the visible reflectance, enabling atmospheric correction to be applied to retrieve land surface properties. Two reflectance thresholds have been determined for band 10 to identify thin cirrus:

Current thresholds: T1 = 0.012; T2 = 0.035

All B10 pixels that had a value in between the two given ranges are classified as thin cirrus in the first step.

3.3.2 Cross check with cloud quality indicator

An additional cross check is done with the probabilistic cloud mask obtained by the cloud detection algorithm described previously. This is due to the fact that pixels classified to be cirrus could have a cloud probability unequal to 0. The cloud probability of thin cirrus cloud pixels detected by S2 Band 10 is checked:

- If the cloud probability is above 0.65 then the thin cirrus cloud classification is rejected and the pixel classification is set to Cloud high probability.
- If the cloud probability is above 0.35 then the thin cirrus cloud classification is rejected and the pixel classification is set to Cloud medium probability.
- If the cloud probability is below or equal 0.35 then the thin cirrus cloud classification is accepted.

3.3.3 Restrictions

Ben-Dor (1994) analyzed a scene from the AVIRIS to demonstrate that thin cirrus detection using 1.38 μm observations may be more difficult for elevated surfaces (>2000m), dry atmospheric conditions, and high albedo surfaces. New injections of volcanic aerosols into the stratosphere may also impact this test.

3.4 Cloud Shadow detection algorithm

The cloud shadow mask is constructed using "geometrically probable" cloud shadows derived from the final cloud mask, sun position and cloud height distribution and "radiometrically probable" cloud shadow derived from the neural network "dark areas" classification described in APPENDIX B.

The literature shows that it is difficult to derive clouds shadow based only on radiometric behaviour because natural features like lakes or hill shadows can present the same spectral signature as cloud shadows. On the other hand it is also time consuming to search geometrically and iteratively for cloud shadow without a good a-priori estimation of

the top-cloud height. Therefore the method we propose here is a combination of these two methods, radiometric and geometric.

3.4.1 Radiometric input

The radiometric input is given by the classification derived from the Neural Network proposed in APPENDIX B. Cloud shadows appear to belong to a “dark areas” class as seen in Figure 3-17. One issue is that other features like lakes or hill shadows belong also to the same class.

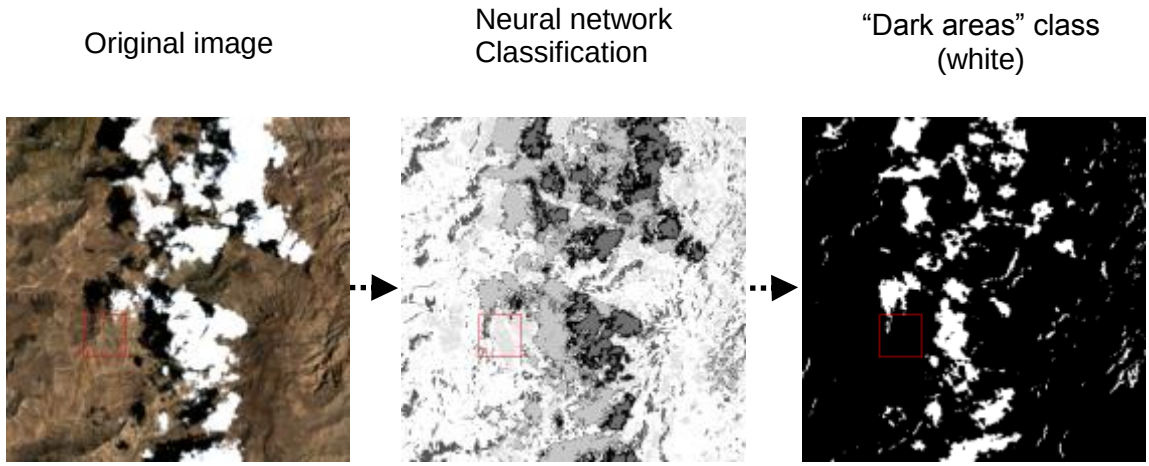

Figure 3-17 – Neural Network “Dark Areas” classification

An alternative for the radiometric input is to construct a “dark areas” class by applying a uniform reflectance threshold to all S2 Bands (B2, B3, B4, B8, B11, B12). An empirical reflectance threshold of 0.15 based on the cloud shadow statistics showed similar results.

3.4.2 Geometric input

The geometric input, a mask of “geometrically probable” cloud shadows, is derived from the final cloud mask obtained previously. It helps to resolve any ambiguity about “false cloud shadows” like lakes, dark areas or hill shadows from the first radiometric classification of shadows.

The mask uses the position of the sun, sun elevation, azimuth angles, and an empirical model for top-cloud height distribution shown on Figure 3-18. This empirical distribution has been derived from the analysis the Goddard/Irish cloud assessment dataset, clouds and projected shadows. The mask of “geometrically” probable cloud shadows has the same resolution as the final cloud mask (60m) and gives a probability of cloud shadow that depends on the distance of projection of the cloud shadow.

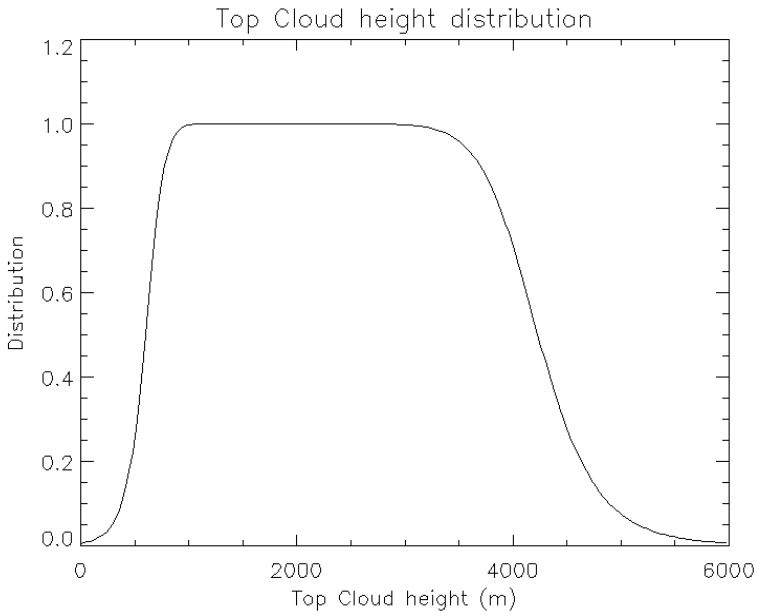

Figure 3-18 – Empirical Top-Cloud height distribution

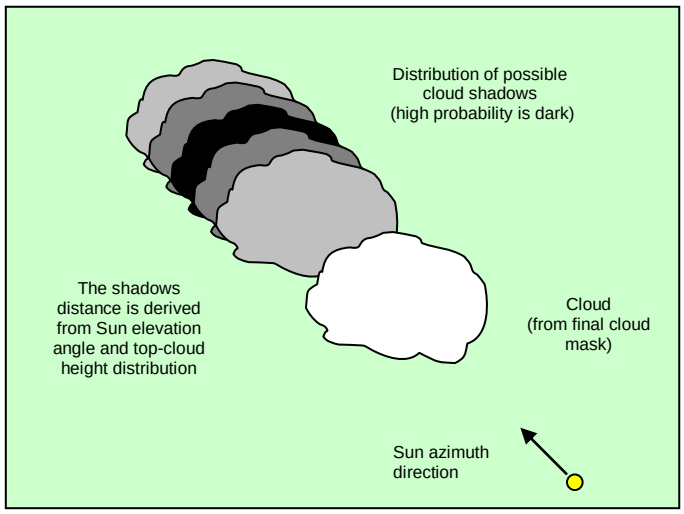

Figure 3-19 – Schematic illustration of the distribution of probable cloud shadows

The computation of this mask is done by the convolution of the final cloud mask by a kernel describing the distribution of “geometrically” probable cloud shadows projected on the ground (assumed to be flat).

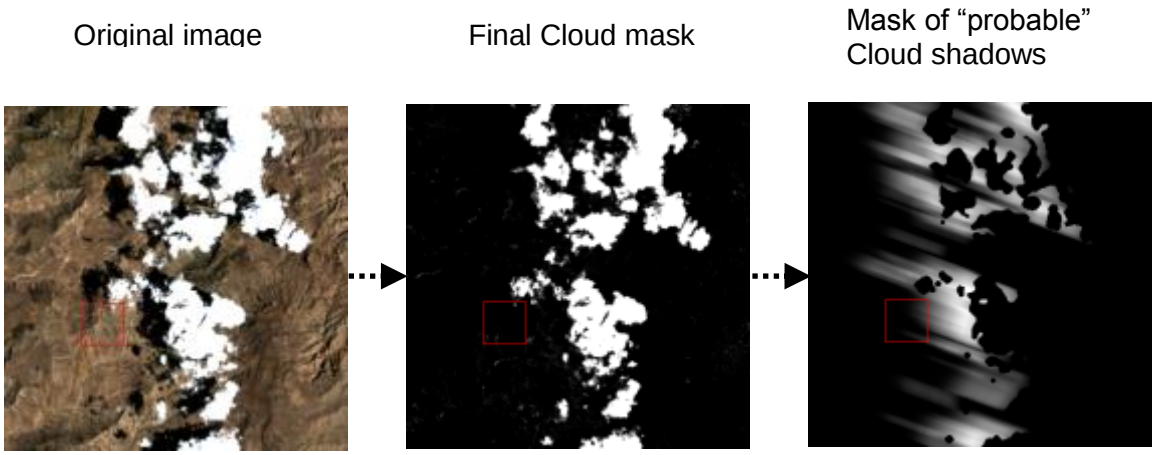

Figure 3-20 – Mask of “geometrically” probable cloud shadows

3.4.3 Generation of cloud shadow mask

The sequence of processing steps to generate the final cloud shadow mask is shown in Figure 3-21. The final cloud shadow mask is obtained by multiplying the result of the radiometric branch by the result of the geometric branch.

3.4.4 Adding cloud shadow information to the classification map

The pixels that have a cloud shadow probability that exceed a threshold are classified as cloud shadows pixels in the classification map.

3.4.5 Restrictions

This cloud detection algorithm is not suitable to detect cloud shadows over water bodies. The cloud shadows over water are expected to be classified as water bodies in the classification map.

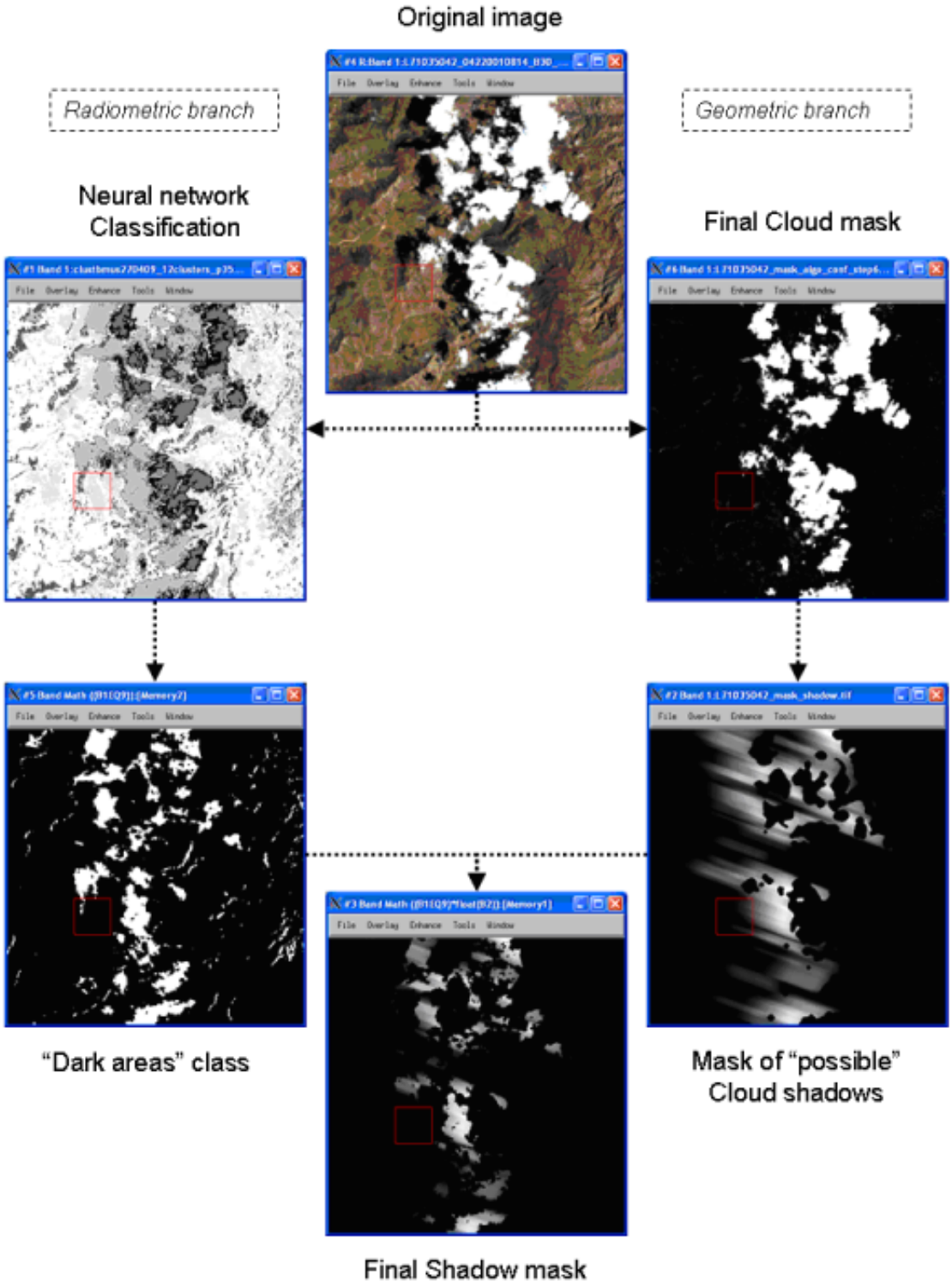

Figure 3-21 – Schematic view of the algorithm for cloud shadow mask generation

3.5 Generation of classification mask

The classification mask is generated along the process of generating the cloud mask quality indicator and by merging the information obtained by the cirrus cloud detection and the cloud shadow detection.

The classification map is produced for each Sentinel-2 Level 1C product at 60 m resolution and byte values of the classification map are organised as follows:

Table 3-I – Classification Map

Label	Classification
0	NO_DATA
1	SATURATED_OR_DEFECTIVE
2	DARK_AREA_PIXELS
3	CLOUD_SHADOWS
4	VEGETATION
5	BARE_SOILS
6	WATER
7	CLOUD_LOW_PROBABILITY
8	CLOUD_MEDIUM_PROBABILITY
9	CLOUD_HIGH_PROBABILITY
10	THIN_CIRRUS
11	SNOW

4. ATMOSPHERIC CORRECTION

This part of the algorithm has to be performed in order to obtain Bottom of Atmosphere corrected transforms using multispectral Level 1C image data as inputs.

The retrieval of atmospheric constituents and surface reflectance is based on a modelling of the radiative transfer in the earth's atmosphere. In most cases, no information on the bidirectional reflectance behaviour of surfaces is available, and a simple isotropic (Lambert) reflectance law has to be assumed. It is intended to use the libRadtran code [2] - [3] to compute the relevant atmospheric terms. In spectral regions dominated by scattering effects, calculations are performed with the scaled DISORT option (discrete ordinate radiative transfer [18]), in regions with strong atmospheric absorption the more accurate correlated k algorithm is employed [2]. The results have to be stored in look-up tables (LUTs).

In a strict sense, the surface reflectance should be called hemispherical-directional reflectance factor (HDRF), or hemispherical-conical reflectance factor HCRF, because the reflected radiation is always measured in a small cone. For small instantaneous field-of-view sensors "directional" is also a sufficiently accurate geometrical description. The anisotropic reflectance behaviour is characterized by the bidirectional reflectance distribution function (BRDF, [19], [20], [21]). However, for simplicity we will use the abbreviation surface reflectance instead of HDRF or HCRF.

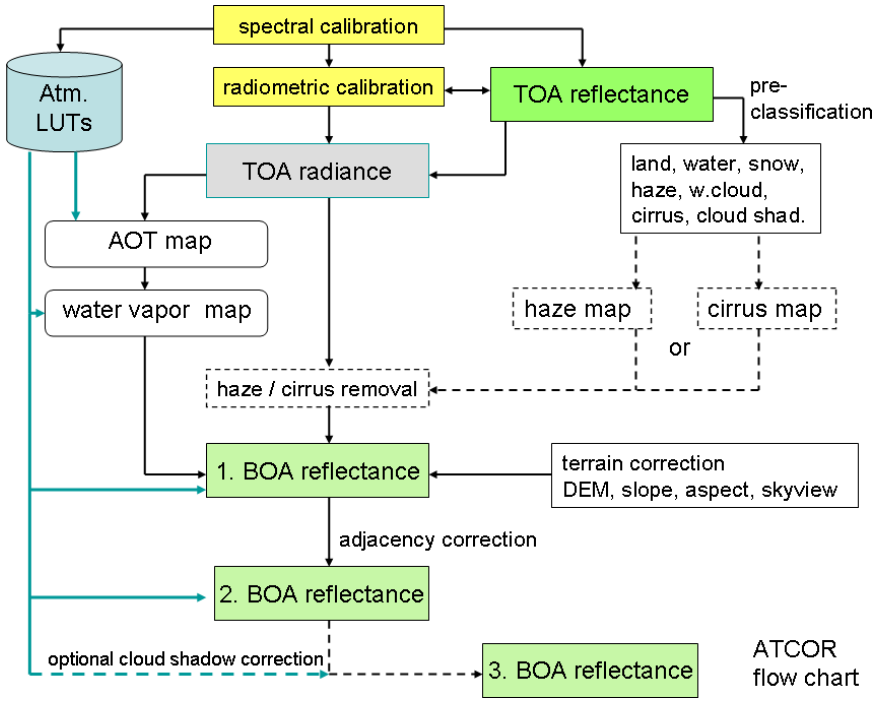

Figure 4-1 – Flow chart of processing

Figure 4-1 presents an overview on the processing steps included in the atmospheric correction. The spectral calibration (channel filter curves) is responsible for the calculation of the atmospheric look-up tables. The radiometric calibration is needed for the TOA reflectance and TOA radiance. Contrary to most other sensors, the level-1 Sentinel-2 data is TOA reflectance and not TOA radiance. Therefore, the flow chart of Figure 4-1 was modified correspondingly. Before the atmospheric correction takes place a coarse pre-classification of the scene (land, water, cloud, etc) is needed, which is part of the already described algorithm in chapter 3. Haze or cirrus corrections are optional steps. Then the aerosol optical thickness (AOT) and water vapour map are derived,

followed by the surface reflectance retrieval. The details are presented in the next sub-chapters.

S2AC employs the Lambert's reflectance law and assumes a constant viewing angle per tile (sub-scene). The solar zenith and azimuth angles can either be treated as constant per tile or can be specified for the tile corners with a subsequent bilinear interpolation across the scene.

4.1 Database of radiative transfer calculations (LUTs)

The libRadtran4 code shall be employed to calculate a database of radiative transfer function for different sensor and solar geometries, ground elevations, and atmospheric parameters[6]. The accuracy of the code shall be better than 5% [2]. The calculations shall be performed with a high spectral resolution of 0.6 nm and the results have to be stored as LUTs. This large database is subsequently resampled with the channel filter functions for a specific sensor, resulting in much smaller LUT file sizes. The atmospheric correction shall then be executed with the sensor-dependent LUT files.

The following list presents the 6-dimensional parameter space and the grid spacing which is required for each parameter. The atmospheric correction processor reads the LUTs pertaining to this parameter space and interpolates if required. For Sentinel-2 the standard processing is for the nadir view in which case the relative azimuth angle does not matter. In addition, there are four basic aerosol types (rural, urban, desert and maritime) available. Interpolation shall be supported for all parameters except the aerosol type.

Table 4-I: Parameter space for atmospheric correction.

parameter	range	increment / grid points
solar zenith angle	0 -70◦	10◦
sensor view angle	0 -10◦	10◦
relative azimuth angle	0 -180◦	30◦(180◦= backscatter)
ground elevation	0 -2.5 km	0.5 km
visibility	5 -120 km	5, 7, 10, 15, 23, 40, 80, 120 km
water vapour(1)	0.4 -5.5 cm	0.4, 1.0, 2.0, 2.9, 4.0, 5.0 cm
water vapour(2)	0.2 -1.5 cm	0.2, 0.4, 0.8, 1.1 cm

(1): *mid-latitud*e *summer*,

(2) mid-latitude winter

The LUT elevation range is 0 – 2.5 km above sea level. Higher elevations up to 3.5 km are calculated with linear extrapolation of the radiative transfer terms with negligible errors for elevations up to 4 km([7,8]).

[6] *See comment in footnote 1, section 1.2 concerning this approach.*

[7] *Ground elevation can in theoretical be extended to 8 km. However, this would put a tremendous burden on the size of the monochromatic database from which the resampled S2 database has to be calculated. It is also not supported in the current ATCOR code, which forms the base of the L2A_AtmCorr algorithm. However, the program internally extrapolates the atmospheric LUTs up to elevations of 3.5 km. In principle, additional LUT elevations of 4 and 8 km could be calculated: the corresponding subroutines reading the LUT files then have to be adapted, with the consequences stated ahead.*

Ozone concentration: Over the spectral range of Sentinel-2 (0.44 – 2.2 µm) several molecular absorbers in the atmosphere have to be taken into account. Most of them can be assumed with a constant mixing ratio on the global scale, such as oxygen, methane, and CO_2. For CO_2 a constant mixing ratio of 400 ppmv is assumed.

Ozone is known to vary on the global scale, extreme values of 200 – 500 Dobson Units (DU) can occur, however, a more typical range of values is from 250 - 400 DU.

With Sentinel-2, ozone cannot be retrieved on a per-pixel basis, but climatological averages can be used, e.g., as implemented in libRadtran's standard atmospheres. For instance, the mid-latitude summer atmosphere has an ozone column of 330 DU at sea level, decreasing with elevation.

Figure 4-2 shows the relative error in surface reflectance retrieval for ozone columns of 250 DU and 410 DU when the retrieval is performed with the assumption of a 330 DU column. The four curves correspond to the two ozone columns (250, 410 DU) and two surface reflectance values of ρ =0.05 (dark surface) and ρ=0.15. Retrieval errors of up to 6% can be found in the 400 - 700 nm part of the spectrum. The error is largest in the 550 – 620 nm region for low reflectance surfaces (relative reflectance error about 5 – 6%) decreasing with surface brightness. The maximum relative reflectance error is about 3% for medium reflectance surfaces with ρ =0.15. The calculation was perfomed with libRadtran4 using the parameters: mid-latitude summer atmosphere, rural aerosol, visibility 23 km, water vapor column 2.9 cm, solar zenith angle 40°, ground at sea level.

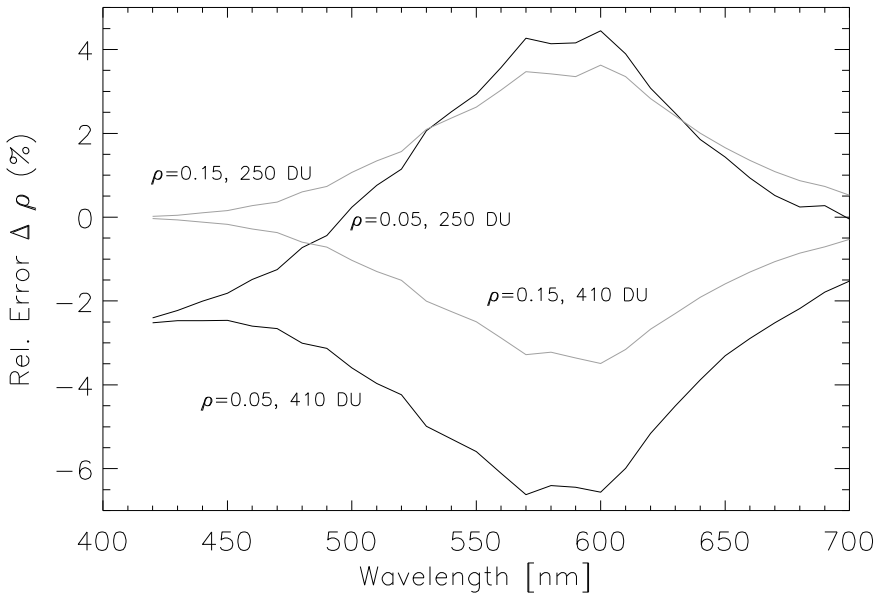

Figure 4-2 – Relative surface reflectance errors due to ozone

The mid-latitude summer and winter atmospheres employ ozone columns of 330 DU and 377 DU, respectively (sea level to space). As the ozone column is not retrieved from the Sentinel-2 imagery, LUTs can be provided for a discrete set of ozone columns if scene-

[8] *The 4 km threshold obviously affects mountainous regions higher than 4 km above sea level. The error impact of processing these regions with the extrapolated height of 3.5 km generally can be considered as small because the highest aerosol concentrations are below 3 km. For the visible bands of S2 the Rayleigh path radiance will be overestimated causing an underestimation of the surface reflectance, which might play an effect for dark surfaces. However, as the regions higher than 4 km are mostly snow covered areas the underestimation effect will be small. An exact value cannot be directly given without empirical measurements.*

average ozone values can always be delivered in the time frame of the Sentinel-2 scene processing. Daily updates with a maximum spatial resolution of 0.125 degree are available via ECMWF (http://www.ecmwf.int/). The ozone columns are no longer provided in DU but in [Kg/m2], so that a recalculation must be performed. Details can be found in section 2.4.1 of [ECMWF]. The following five ozone grid points are proposed for the LUT:

- Summer: 250, 290, 330, 370, 410 DU
- Winter: 250, 290, 330, 377, 420 DU

No ozone LUT interpolation will be performed, but the nearest grid point is selected.

The use of winter LUTs is recommended based on geography and climatology, because the use of summer LUTs under winter conditions yields relative surface reflectance retrieval errors up to 8% for channels beyond 700 nm.

4.2 Retrieval of aerosol optical thickness

If a sensor has the appropriate spectral bands, the aerosol type and visibility or optical thickness of the atmosphere can be derived, provided the scene contains reference areas of known reflectance behaviour, preferably dense dark vegetation (DDV) and water bodies [36], [37] [38].

If not enough dark reference areas can be found in the scene, the threshold in the 2.2 µm band will be iteratively raised (from surface reflectance = 0.05 to 0.10 and 0.12) to work with reference areas of medium brightness. A validation and accuracy assessment of the method can be found in [37, 38], so no separate validation is conducted here.

The results are smoothed with a moving window of 3 km × 3 km. There are two reasons for the low-pass filtering: (i) to suppress noise, and (ii) to smooth the influence of biome-dependent fluctuations of the spectral band correlation coefficient. A change of the aerosol type between successive scenes may cause brightness steps in the BOA reflectance at scene borders.

It follows a brief summary of the DDV algorithm:

The SWIR2 band (B12 at 2.19 μm) of the scene is searched for dark (or medium brightness) pixels and a correlation of the SWIR reflectance with the reflectance in B4 (red) and B2 (blue) can be employed to estimate the visibility automatically [37]. For this purpose, we use a modified version of the original idea for the following algorithm.

The SWIR2 reflectance is calculated assuming a visibility of 23 km (instead of the original version of top of atmosphere reflectance). Then, water pixels are excluded by employing only those pixels with SWIR reflectance values above 1% and an NDVI > 0.1. For the 2.2 μm band the upper threshold of the reflectance of the dark pixels is selected as 5%. If the number of reference pixels is less then 1% of the image pixels, then the upper reflectance threshold is increased to 10% or finally 12%. If the SWIR2 module would fail, the 1.6 μm band could be taken as a substitute. Then the corresponding upper reflectance thresholds are selected as 10% and 15%, or finally 18%, respectively. The reflectance ratios for B4 (red) and B2 (blue) are then calculated as:

$$\rho_{red} = 0.5\ \rho_{2.2} \qquad and \qquad \rho_{blue} = 0.5\ \rho_{red} \tag{0.1}$$

$$\rho_{red} = 0.25\ \rho_{1.6} \qquad and \qquad \rho_{blue} = 0.5\ \rho_{red} \tag{0.2}$$

This situation is sketched in Figure 4-3 (left). The correlation factor of 0.5 between the 2.2 μm and the red region is not a universal constant, but may typically vary between 0.4 and

0.6. The correlation actual also works for dark soils. So the dark pixels may also include soil areas. As the correlation factor may in general depend on the biome, season, and geography, an update of the DDV model would improve the accuracy of the aerosol retrieval. A seasonal DDV model was proposed for large boxes (about 10 km × 10 km) of MERIS data [40], but world-wide DDV model maps at a spatial resolution of about 100 m are currently not available.

B4 (red band) is then used to calculate the visibility (compare Figure 4-3 right) as the intersection of the measured radiance with the simulated visibility-dependent at-sensor radiance curve. Since the same visibility is employed for the blue spectral band this provides an opportunity to adjust the spectral behaviour of the path radiance (which is essentially the aerosol path radiance, since the Rayleigh path radiance is known) in the blue spectral region.

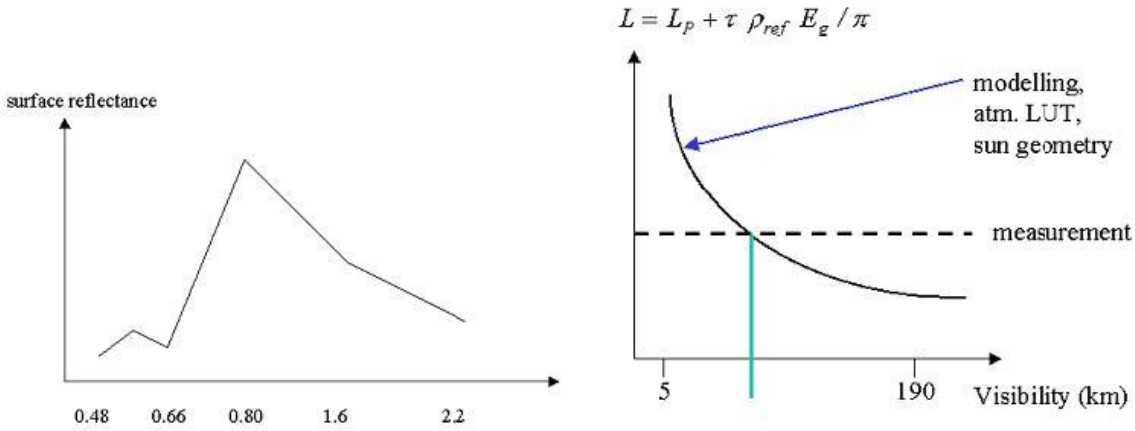

Figure 4-3 – Correlation of reflectance of dark vegetation in different spectral regions and visibility calculation

$$L_{p,blue}^{update} = L_{blue} - \tau_{blue}\rho_{blue}E_{g,blue}/\pi \quad (0.3)$$

Once the visibility and AOT have been calculated for the dark reference pixels, the average value is taken for the non-reference pixels, and the corresponding map is smoothed with a 3 km x 3 km spatial filter to remove noise and to suppress small-scale fluctuations that might be caused by biome-dependent changes in the spectral correlation. Experience with MODIS has shown that a large spatial filter size is necessary to avoid artefacts [39].

If a sufficiently large percentage (2-5%) of dark reference pixels can be found in a scene, the aerosol optical thickness is computed. If the scene also contains water bodies the water reflectance is checked in B8 (NIR band) and if negative reflectance pixels are encountered, the aerosol optical thickness is decreased (visibility increased) until the percentage of negative reflectance pixels is less than 1% of the scene pixels.

The original calculation is performed in the visibility space, because the atmospheric LUTs were calculated based on libRadtran's visibility parameter. However, the conversion from visibility VIS to AOT (at 550 nm) can be calculated with equation (0.4).

$$AOT(z, VIS) = exp\,(a(z) + b(z)ln(VIS)) \quad (0.4)$$

where a(z) and b(z) are obtained with a linear regression for a set of elevations z ranging between 0 and 2.5 km above sea level. The regression is performed with height data

between 0 and 2.5 km above sea level. But once the coefficients are calculated, this equation can be applied for z > 2.5 km. However, as stated in chapter 2.3, the maximum elevation for S2AC is 3.5 km, and elevations greater than 3.5 km are treated as having the maximum elevation. Besides the AOT file, S2AC employs an integer visibility index ('vi') file ranging from vi=0 to vi=182 to speed up array indexing. Here, vi=0 corresponds to VIS=190 km, and the 'vi' increment of 1 corresponds to an AOT increment 0f 0.006.

$$\delta = 0.185 + 0.006\ vi \tag{0.5}$$

In addition to B8, B4 is also checked for negative reflectance pixels (vegetation). An update of the visibility with respect to the specified input value shall be noticed. The final iterated visibility depends slightly on the initial value, because a coarse set of visibility grid points is used to restrict the number of iterations (n ≤ 8), see Table 4-II.

*Exampl*e : start vis = 10 km, potential visibility iterations = 19, 24, 34, 44, 54, 64, 74 km. The next step of 84 km is reset to 80 km. If the number of negative reflectance pixels (B4, B8 bands) is already less than 1% of the number of scene pixels for vis = 34 km, the program shall terminate the visibility loop after three iterations.

The upper visibility threshold of 80 km is a trade-off: although higher visibilities are possible they are not very likely, and even if a situation with a higher visibility (say vis=100 km) is encountered, results of a calculation with vis=80 km does not differ much from the results with vis=100 km. So the iteration capability is most important for low visibility start values.

Table 4-II – Visibility iterations on negative reflectance pixels (B2, B8)

visibility [km]	vis. increment [km]
5 -15	3
15 -20	4
20 -28	5
28 -60	10
60 – 80	10, but max VIS=80 km

The question of an automatic aerosol type calculation is addressed next.

Aerosol type estimation

After calculation of the scene path radiance in the blue and red region (as total minus reflected radiance, using the average values obtained for the dark reference pixels) the ratio of *L*p(*blue*, *scene*) to *L*p(*red*, *scene*) can be compared to the corresponding ratio for the libRadtran standard aerosols (rural, urban, maritime, desert) :

$$d_p = \frac{L_p(blue, scene)/L_p(red, scene)}{L_p(blue, MODTRAN)/L_p(red, MODTRAN)} \tag{0.6}$$

The aerosol type for which the double ratio (*d*p) is closest to 1 is the best approximation for the scene. It approximates the corresponding libRadtran aerosol type. However, some fine tuning is subsequently performed to be able to modify the wavelength behaviour of the path radiance compared to the standard aerosol types. If *L*p(*blue*, *scene*) deviates more than 5% from *L*p(*blue*, *libRadtran*) then *L*p(*blue*, *scene*) is used as the valid path radiance. In addition, the path radiance for any other bands in the blue to red region is

linearly re-scaled with the factor *L*p(*blue*, *scene*)/*L*p(*blue*, *libRadtran*), see Figure 4-4. Here, the path radiance in B4 is used as a fixed tie point. For wavelengths greater than 700 nm a possible typical 10% difference in path radiance between the selected aerosol type (after fine tuning) and the actual aerosol is usually not important, because path radiance contributes only a small fraction to the total radiance.

As the derived aerosol type is constant per scene in the S2AC model, the question arises whether the automatic selection is the best choice, especially if one considers neighbouring scenes. In this case the aerosol types could switch, leading to steps in the surface reflectance at the image borders. From this point of view a pre-selected aerosol type (e.g. rural-continental) might be the better choice in practise.

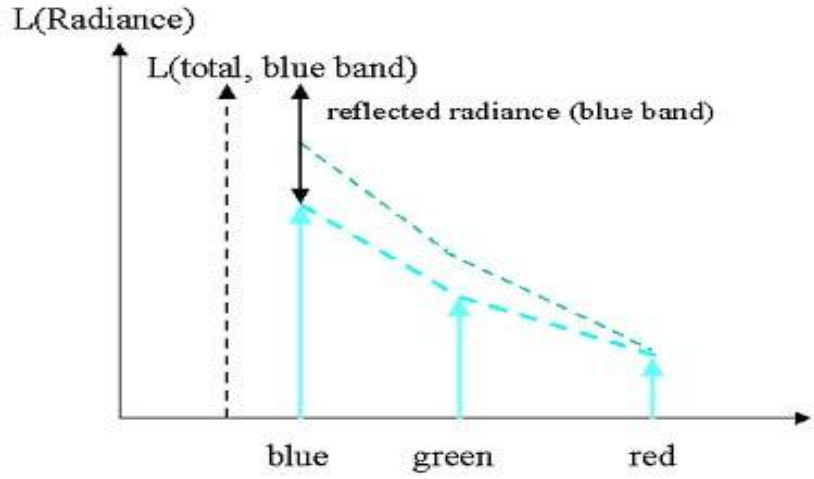

Figure 4-4 – Rescaling of the path radiance with the blue and B4

After subtraction of the reflected radiance from the total radiance in B2 the remaining signal is the updated path radiance. The path radiance of bands in the blue to red region is then rescaled with interpolation.

Summary

The algorithm starts with a user-defined visibility (e.g. 20 km) that is iterated as mentioned above. If the scene contains no dark vegetation (i.e., no very dark pixels), the surface reflectance threshold in the 2.2 µm band is raised from 0.05 to 0.10 or 0.12 to include medium brightness reference pixels. If the scene contains no reference and no water pixels then the scene is processed with the start visibility. If the visibility is constant per scene and the terrain is flat, no aerosol optical thickness (AOT) map is written to file, but the visibility and its corresponding AOT value are listed in the output ”log” file of S2AC. In case of a rugged terrain, the AOT map depends on surface elevation, and will always be written as an output file even for a constant visibility.

The presented approach has similarities and some differences to Kaufman [36, 37] and Liang [38]. All these algorithms rely on DDV and water bodies. Differences are:

- The Kaufman/MODIS approach does not iterate to reduce negative reflectance values, so this is an advantage in the S2AC approach.

- S2AC supports a variable aerosol model, but the recommendation is to employ a fixed aerosol type during operational processing, because of the potential problem of a switching of aerosol types between successive scenes (or within the set of tiles for one scene) in a Sentinel-2 trajectory which can cause brightness steps at the scene / tile borders.

- The LUTs of S2AC are different from the LUTs in [37-39], but the relevant radiative transfer quantities are included. The same argument also applies to the spectral bands: MODIS, Landsat TM, ETM, and S2 channels are different, but the LUTs are adapted to the spectral channels.

The method of Liang was validated with quantitative and statistical analyses using Landsat-5 TM imagery from several campaigns (FIFE, SCAR A). However, the influence of the adjacency was neglected in his method.

The recommended baseline for operational S2 processing is a fixed aerosol type (rural / continental).

4.3 Retrieval of water vapour

A water vapour retrieval can be included after the aerosol retrieval because the aerosol retrieval does not use water vapour sensitive spectral bands, but the water vapour algorithm (employing bands B8a (865 nm) and B9 (945 nm)) depends on aerosol properties. The water vapour retrieval over land is performed with the APDA (atmospheric precorrected differential absorption) algorithm [11] which has to be applied to two Sentinel-2 bands (B8a, B9).. Band 8a is the reference channel in an atmospheric window region, band B9 is the measurement channel in the absorption region. The absorption depth is evaluated as sketched in Figure 4-5 (line from point A to B) where the radiance at point A is calculated for an atmosphere with no water vapour assuming that the surface reflectance ρ_2 for the measurement channel is the same as for the reference channel ρ_1. The depth of the absorption feature (A –B) is a measure of the water vapour column content.

The water vapour dependent APDA ratio is calculated as :

$$R_{APDA}(\rho,u)=\frac{L_2(\rho_2,u)-L_{2,p}(u)}{L_1(\rho_1,u)-L_{1,p}(u)} \tag{0.7}$$

where the index 1 and 2 indicates bands B8a and B9, respectively. L and L_p are the total at-sensor radiance and path radiance, respectively. The symbol u indicates the water vapour column.

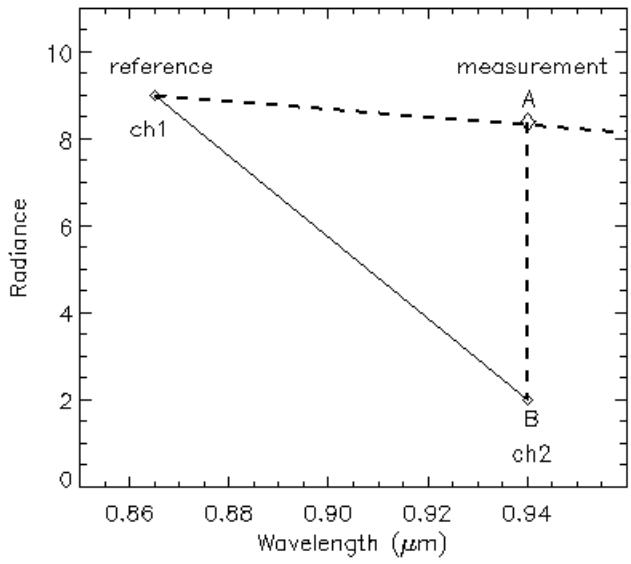

Figure 4-5 – Reference and measurement channels for the water vapour method

The problem is the estimation of the surface reflectance ρ_2 in the absorption band. The assumption $\rho_2 = \rho_1$ is recommended .for two reasons. First, the surface reflectance at B9 is difficult to assess from the other bands (e.g. non-linear reflectance behaviour of vegetation, iron content of soils), and second, the other bands are only marginally dependent on water vapour.

LUTs are then calculated for different atmospheric conditions (water vapour columns) and sun angles and an exponential fit function can be used to calculate the relationship between R_{APDA} and u

$$R_{APDA}(u) = exp\left(\alpha + \beta\sqrt{u}\right) \tag{0.8}$$

which can be solved for the water vapour column u , see Figure 4-6, where the diamonds in the figure mark the calculated water vapour grid points (u= 0.4, 1.0, 2.0, 2.9 cm) :

$$u = \left(\frac{\alpha = ln(R_{APDA}}{\beta}\right)^2 \tag{0.9}$$

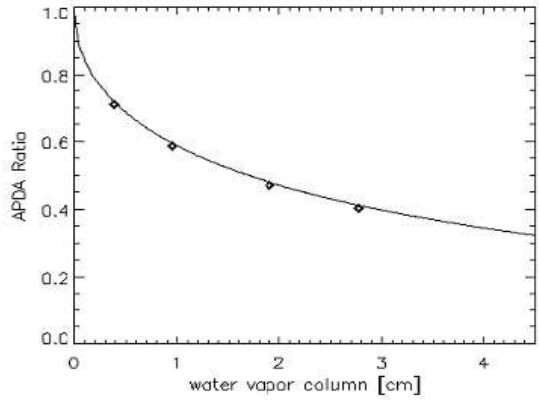

Figure 4-6 – APDA ratio with an exponential fit function for the water vapour

Equations (0.7) to (0.9) are iterated, starting with u=1.0 cm, calculating RAPDA, updating u, Li,p(u), ρ1, ρ_2 and repeating the cycle.

Remarks:

The APDA algorithm is relatively fast .Its disadvantage is that it is not stable numerically for very low reflectance targets (water, shadow regions). For water surfaces the scene-average value of the land water vapour column is taken as a default.

Five water vapour grid points at 0.4, 1.0, 2.0, 2.9, and 4.0 cm are sufficient to cover the 0.5 5.0 cm range with an accuracy of about 5-10 % [6]. The grid point 5.0 cm was recently added for the summer atmosphere to improve the accuracy in the 4.5 – 5.5 cm range.

For winter conditions, a typical winter altitude profile of air temperature / humidity will be selected (the libRadtran mid-latitude winter) to improve the accuracy of the water vapor and surface reflectance retrievals in such conditions, compare chapters 2.3 and 3. In this case the water vapor grid points are 0.2, 0.4, 0.8, and 1.1 cm.

4.4 Haze removal over land

Has removal is an optional processing which shall be switched to off in the default processing algorithm: the haze detection and removal algorithm partitions the scene into clear and hazy areas, then uses histogram matching techniques to subtract the haze signal before carrying out the 'normal' atmospheric correction. If applied to separate tiles of a scene, brightness steps in haze-corrected areas might occur at tile borders. Therefore, haze removal needs to be conducted on the full scene without tiling. As the Sentinel-2 scene level is a tile-based processing this option will be disabled. However the algorithm is described here for reasons of completeness.

The proposed haze removal algorithm works well in the majority of cases, but not always. Therefore, it is not part of the baseline processing. Problems will arise if the scene contains very turbid water bodies that are not identified as water. The reason is that water and clouds have to be masked prior to the haze removal.

An intermediate output product is calculated which is the haze-corrected image, but only for channels in the 400 -800 nm region. The second step is the 'normal' atmospheric correction with tiling using the haze-corrected channels (below 800 nm) and the remaining channels (beyond 800 nm).

In many cases of satellite imagery the scene contains haze and cloud areas. The optical thickness of cloud areas is so high that the ground surfaces cannot be seen, whereas in hazy regions some information from the ground is still recognizable. In S2AC the scene is partitioned into clear, hazy, and cloud regions. Here we will treat the low altitude boundary layer (0 -3 km) haze as opposed to high altitude cirrus. Thin boundary layer haze can be detected with broad-band multispectral instruments. As a first approximation, haze is an additive component to the radiance signal at the sensor. It can be estimated and removed as described below. Cloud areas have to be masked to exclude them from haze areas and to enable a successful haze removal. The treatment of cloud shadow regions is discussed in chapter 2.7. The haze removal algorithm runs fully automatic. It is a combination of the improved methods [45], [56] and consists of five major steps:

1. Masking of clear and hazy areas with the tasseled cap haze transformation [48].

$$TC = x_1 * BLUE + x_2 * RED \tag{0.10}$$

where BLUE, RED, *x*1=0.846, and *x*2=-0.464 are the blue band B2, red band, B4 and weighting coefficients, respectively. The clear area pixels are taken as those pixels where TC is less than the mean value of TC.

Calculation of the regression between the blue (B2) and red band (B4) for clear areas ("clear line" slope angle α), see figure 2.7

Haze areas are orthogonal to the "clear line", i.e., a haze optimized transform (HOT) can be defined as :

$$HOT = BLUE * sin\alpha - RED * cos\alpha \tag{0.11}$$

HOT values are rounded to integer, called HOT level.

Calculation of the histogram of HOT for the haze areas.

For bands below 800 nm the histograms are calculated for each HOT level j. The haze signal Δ to be subtracted is computed as the DN corresponding to HOT(level j) minus the DN corresponding to the 2% lower histogram threshold of the HOT(haze areas). The de-hazed new digital number is:

$$DN(new) = DN - \Delta \tag{0.12}$$

So the haze removal is performed before the surface reflectance calculation. Two options are available: the use of a large area haze mask (equation (0.13)), which is superior in most cases, or a compact smaller area haze mask (equation (0.14)).

$$HOT > mean(HOT) - 0.5 * stdev(HOT) \tag{0.13}$$

$$HOT > mean(HOT) \tag{0.14}$$

In addition, the user can select between haze removal of ”thin / medium haze” or ”thin to moderately thick haze”, the last option is superior in most cases.

The algorithm only works for land pixels, so the water mask is used to exclude water pixels. Cloud pixels are excluded with the default reflectance threshold T = 25% in the blue-green spectral region, see the description of the file *preference parameters.dat* in ([49], chapter 6.2).

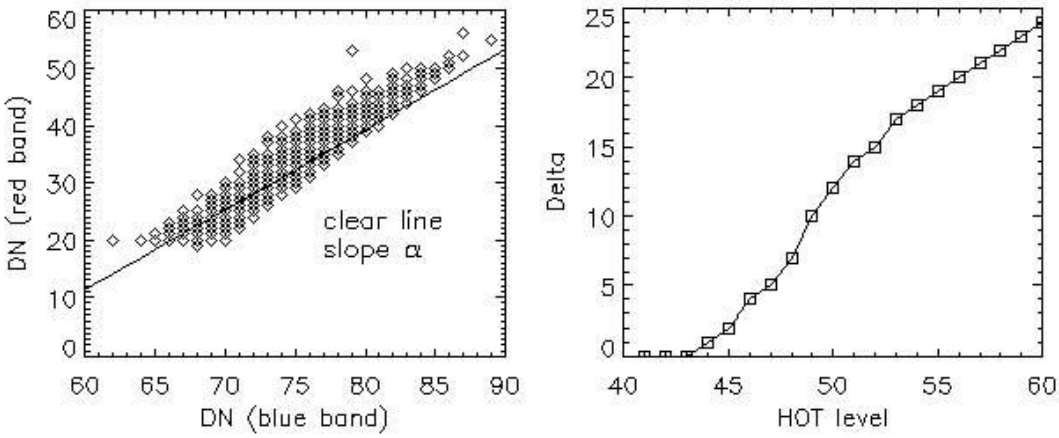

Figure 4-7 – Haze removal method; Left: regression between B4 and B2 for clear areas. Right: calculation of Delta=Δ as a function of the HOT haze level (example Landsat TM band 1)

4.5 Cirrus removal

On the first glance, images contaminated by cirrus appear similar to hazy scenes discussed in the previous section. However, haze usually occurs in the lower troposphere (0-3 km) while cirrus clouds exist in the upper troposphere and lower stratosphere (8 -16 km). The effect of boundary layer haze can be observed in the visible region, but seldom in longer wavelength channels > 850 nm. However, cirrus also affects the NIR and SWIR spectral regions. Thin cirrus clouds are difficult to detect with broad-band multispectral satellite sensors in the atmospheric window regions, especially over land, because land scenes are spatially inhomogeneous and this type of cloud is partially transparent. On the other hand, water vapour dominates in the lower troposphere and usually 90% or more of the atmospheric water vapour column is located in the 0 -5 km altitude layer. Therefore, if a narrow spectral band is selected in a spectral region of very strong water vapour absorption, e.g., around 1.38 μm or 1.88 μm, the ground reflected signal will be totally absorbed, but the scattered cirrus signal will be received at a satellite sensor or a sensor in a high-altitude aircraft (e.g., 20 km AVIRIS scenes).

So a narrow channel at 1.38 μm is able to detect cirrus clouds, and if a correlation of the cirrus signal at this wavelength and other wavelengths in the VNIR and SWIR region can be found, then the cirrus contribution can be removed from the radiance signal to obtain a

cirrus-corrected scene[9]. The basic ideas of cirrus correction were presented in several papers ([41], [42], [44]). The algorithm differs for water and land pixels. For water, a scatterplot of the 1.38 μm versus B8a (865 nm) channel is used, for land the band-correlation is determined from a scatterplot of the 1.38 μm versus the red channel B4 (665 nm). To obtain a high sensitivity, only vegetation pixels are taken because they have a low reflectance in the red spectral region, so the cirrus contribution is easily traced. The scatterplot is computed in terms of the apparent (TOA or at-sensor) reflectance of ρ1.38 versus ρred where the apparent reflectance is defined as:

$$\rho^* = \frac{\pi L}{E_s \ cos\theta_s} \tag{0.15}$$

where L is the recorded radiance signal, Es the extraterrestrial solar irradiance for the selected band, and θs is the solar zenith angle. Following [41] the method can be described by the following set of equations:

$$\rho^*(\lambda) = \rho_c(\lambda) \ + \ \frac{T_c(\lambda) \ \rho(\lambda)}{1 \ - s_c(\lambda) \ \rho(\lambda)} \tag{0.16}$$

Here, ρ_c is the reflectance of the cirrus cloud, Tc the two-way transmittance (direct plus diffuse) through the cloud, ρ the reflectance of the *"virtual*" surface (land or water surface including all effects of molecular and aerosol scattering below the cirrus), and s_c is the cloud base reflectance of upward radiation. Equation (0.16) can be simplified, because of $s_c \ \rho << 1$, yielding

$$\rho^*(\lambda) = \rho_c(\lambda) \ + \ T_c(\lambda) \ \rho(\lambda) \tag{0.17}$$

With the assumption that the cirrus reflectance ρc(λ) is linearly related to the cirrus reflectance at 1.38 *μm we obtain*

$$\rho^*(\lambda) = \rho_c(1.38\mu m) \ / \ \gamma \tag{0.18}$$

where γ is an empirical parameter derived from the scene scatterplot of ρ1.38 versus ρred. It depends on the scene content, cirrus cloud height, and solar and viewing angles. Figure 4-8 shows an example of such a scatterplot. The red line is the left-side boundary of data points that are not influenced by ground surface reflection, i.e. cirrus-contaminated pixels are clustered around this line, and its slope represents the correlation coefficient γ (the blue line represents the first of several iterations). Papers on the cirrus algorithm often restrict eq. 2.45 to the wavelength interval 0.4 <λ< 1 *μm*, but we will extend this relationship into the SWIR region. Substituting equation (0.18) into equation (0.17) yields

$$T_c(\lambda) \ \rho(\lambda) = \rho^*(\lambda) \ - \ \rho_c(1.38\mu m) \ / \ \gamma \tag{0.19}$$

[9] The parallax difference between the cirrus band and other bands is up to 0.81°. The parallax error will be compensated in the ortho-rectified product at the ground surface. However, a parallax error will remain at the cirrus altitude level. As cirrus altitudes cannot be calculated from Sentinel-2 imagery and may vary between typically 8 and 20 km the corresponding spatial misregistration is up to about 300 m. So the issue of cirrus removal is left open.

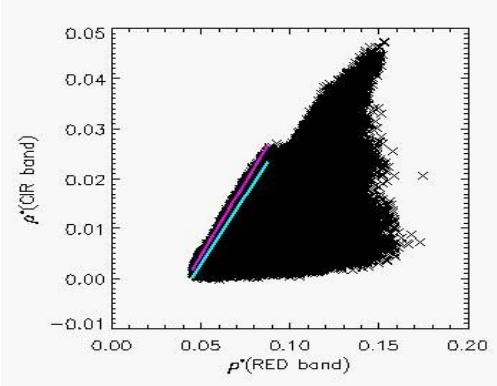

Figure 4-8 – Scatterplot of apparent reflectance of cirrus (1.38 µm) band versus B4 (red band)

Neglecting the cirrus transmittance T_c (i.e., setting T_c = 1), we obtain the *"cirrus path radiance corrected*" apparent reflectance image (index 'cc'):

$$\rho^*_{cc}(\lambda) = \rho^*(\lambda) \; - \; \rho_c(1.38\mu m) \; / \; \gamma \tag{0.20}$$

As the cirrus is almost on top of the atmosphere we have $\rho c(1.38\mu m) = \rho^* c\,(1.38\mu m)$ and the apparent cirrus reflectance can be calculated with equation (0.15). Cirrus removal is conducted as the first step during atmospheric correction, followed by the aerosol and water vapour retrievals. If the average water vapour column W of a scene is less than some threshold (default W=0.6 cm) then the cirrus removal algorithm is switched off, to avoid a misinterpretation of bright surfaces as cirrus in the 1.38 µm channel. Normally, atmospheric water vapour completely absorbs surface features in the 1.38 µm channel, but the channel might become partly transparent to surface features for very low water vapour values. This water vapour threshold can be set in the file containing the preference parameters for the atmospheric processing.

The cirrus and (boundary layer) haze removal options are exclusive, i.e., only one of them can be selected per run. The cirrus detection and removal is the baseline processing.

4.6 Cloud shadow removal

De-shadowing is not part of the baseline operational processing, but can be used during the commissioning phase. This chapter contains a brief overview on the cloud shadow algorithm. More details and examples of processing can be found elsewhere ([49], [46]). It is recommended not to use this algorithm in the fully automatic processing, because it requires much more processing time and needs optimized information on two thresholds that can best be determined in an interactive mode. It can be used in the fully automatic mode, but at the cost of deteriorated results.

Remotely sensed optical imagery of the Earth's surface is often contaminated with cloud and cloud shadow areas. Surface information under cloud covered regions cannot be retrieved with optical sensors, because the signal contains no radiation component being reflected from the ground. In shadow areas, however, the ground-reflected solar radiance is always a small non-zero signal, because the total radiation signal at the sensor contains a direct (beam) and a diffuse (reflected skylight) component. Even if the direct solar beam is completely blocked in shadow regions, the reflected diffuse flux will remain. Therefore, an estimate of the fraction of direct solar irradiance for a fully or partially shadowed pixel can be the basis of a compensation process called de-shadowing or shadow removal. The method can be applied to shadow areas cast by clouds or buildings.

The proposed de-shadowing technique works for multispectral and hyperspectral imagery over land acquired by satellite / airborne sensors. The method requires a channel in the visible and at least one spectral band in the near-infrared (0.8-1 μm) region, but performs much better if bands in the short-wave infrared region (around 1.6 and 2.2 μm) are available as well. The algorithm consists of these major components: (i) the calculation of the covariance matrix and zero-reflectance matched filter vector, (ii) the derivation of the unscaled and scaled shadow function, (iii) a histogram thresholding of the unscaled shadow function to define the core shadow areas, (iv) a region growing to include the surroundings of the core shadow areas for a smooth shadow/clear transition, and (v) the de-shadowing of the pixels in the final shadow mask.

The method starts with a calculation of the surface reflectance image cube $\rho i = \rho(\lambda i)$, where three spectral bands around λi = 0.85, 1.6, and 2.2 μm are selected. These bands from the near and shortwave infrared region are very sensitive to cloud shadow effects, because the direct part of the downwelling solar radiation flux at the ground level is typically 80% or more of the total downwelling flux. Channels in the blue-to-red region (0.4-0.7 μm) are not used for the detection of shadow regions because they receive a much larger diffuse radiation component, making them less sensitive to partial shadow effects. Instead, visible channels serve to define a potential cloud mask.

The surface reflectance is first computed with the assumption of full solar illumination, i.e., the global flux on the ground consists of the direct (Edir) and diffuse (Edif) component. If DN denotes the digital number of a pixel, LP the path radiance, and τ the atmospheric transmittance (ground-to-sensor) the surface reflectance can be obtained as:

$$\rho_i(x,y) = \frac{\pi(d^2\{c_0(i) + c_1(i)DN_i(x,y)\} - L_{p,i})}{\tau_i\{E_{dir,i} + E_{dif,i}\}} \tag{0.21}$$

Here, d is the Earth-Sun distance at the image acquisition time in astronomical units, c0 and c1 are the radiometric calibration coefficients (offset and slope) to convert the digital number into the corresponding at-sensor radiance L, i.e., $L = c_0 + c_1 DN$, and i is the channel index.

The proposed de-shadowing algorithm consists of a sequence of eight processing steps as sketched in Figure 4-9. It starts with the atmospheric correction. The next step is the masking of water bodies and cloud areas with simple spectral criteria as detailed below. Water pixels have to be excluded as far as possible to avoid their assignment as shadow pixels.

Step 3 calculates the covariance matrix $C(\rho)$ where ρ is the surface reflectance vector comprising only the non-water and non-cloud pixels. For each pixel, this vector holds the reflectance values in the 3 selected channels (around 0.85, 1.6, 2.2 μm). The matched filter is a vector tuned to a certain target reflectance spectrum ρ_t to be detected:

$$V_{mf} = \frac{C^{-1}(\rho_t - \bar{\rho})}{(\rho_t - \bar{\rho})^T C^{-1}(\rho_t - \bar{\rho})} \tag{0.22}$$

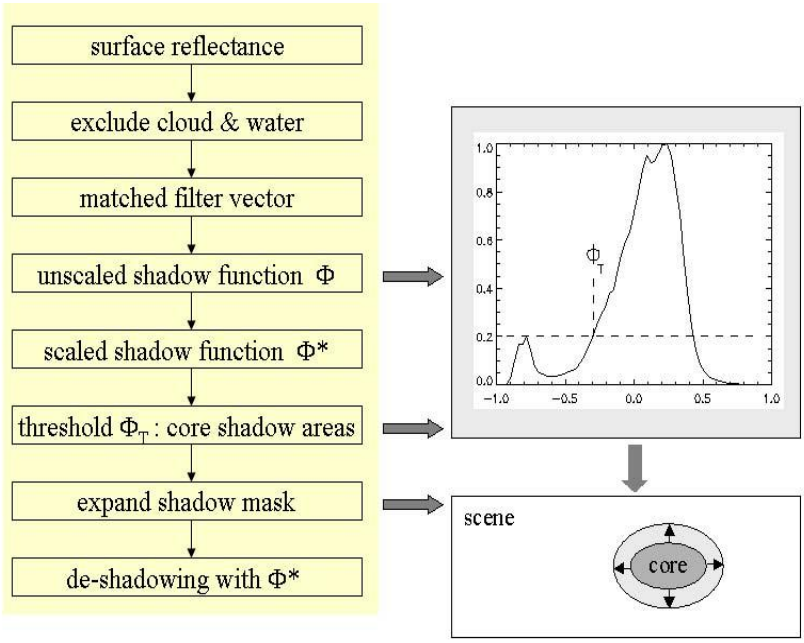

Figure 4-9 – Flow chart of processing steps during de-shadowing

Here, $\bar{\rho}$ is the scene-average spectrum, without the water/cloud pixels. Selecting $\rho_t = 0$ for a shadow target yields a special simplified form of the matched filter, where the 'sh' index symbolizes shadow:

$$V_{sh} = -\frac{C^{-1}\bar{\rho}}{\bar{\rho}^T C^{-1}\bar{\rho}} \tag{0.23}$$

The shadow matched filter vector is then applied to the non-water/non-cloud part of the scene and yields the still un-normalized values φ that are a relative measure of the fractional direct illumination, also called *unscale*d *shado*w *functio*n here:

$$\Phi(x,y) = V_{sh}^T(\rho(x,y) - \bar{\rho}) \tag{0.24}$$

The matched filter calculates a minimum RMS shadow target abundance for the entire (nonwater/non-cloud) scene. Therefore, the values of Φ are positive and negative numbers. The arbitrary, image-depending range of Φ has to be rescaled to the physical range from 0 to 1, where 0 indicates no direct illumination (full shadow), and 1 means full direct illumination. The histogram of Φ is used to rescale the image data. Figure 4-10 shows a schematic sketch of such a histogram with a smaller peak (at Φ2) representing the shadow pixels and the main peak (at Φmax) representing the majority of the fully illuminated areas. The statistical assumption is used that full direct solar illumination is already obtained for pixels with Φ(*x*, *y*)=Φmax . Then the values Φ are linearly mapped from the unscaled (Φmin, Φmax) interval onto the physically scaled (0,1) interval, where the *scale*d *shado*w *functio*n is named Φ∗:

$$\Phi^* = \frac{\Phi - \Phi_{min}}{\Phi_{max} - \Phi_{min}} \qquad if \quad \Phi \le \Phi_{max} \tag{0.25}$$

The smallest value of the scaled shadow function is $\Phi^*_{min} = 0$, which means no direct illumination.

However, to avoid overcorrection and to cope with scenes containing merely partial shadow areas, it is advisable to set Φ^*_{min} at a small positive value. This value of Φ^*_{min}, i.e., the minimum fractional direct illumination (deepest shadow in a scene, typically ranging between 0.05 and 0.10) is scene-dependent, see the detailed discussion below.

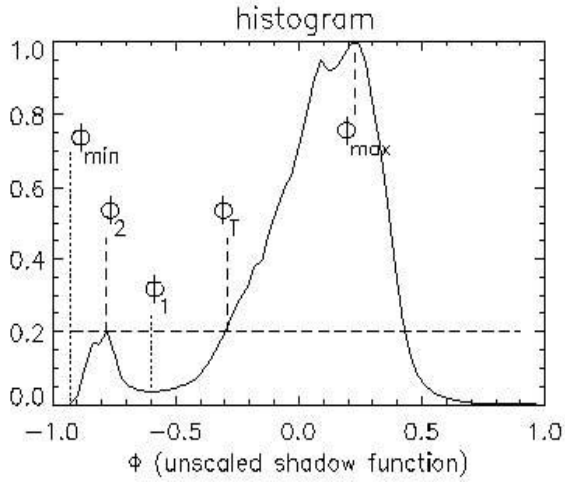

Figure 4-10 – Normalized histogram of unscaled shadow function

In principle, the de-shadowing could now be performed with the physically scaled function $\Phi*$, which represents the fraction of the direct illumination for each pixel in the ρ vector, i.e., the complete scene without cloud and water pixels. However, since the matched filter is not a perfect shadow transformation, it is much better to restrict its application to the potential, most-likely shadow areas. This is an important processing step to reduce the number of mis-classifications or false-alarms. If omitted it will cause strange 'shadow' pixels scattered all over the image, see [49], [46].

Therefore, the proposed method tries to find the core shadow areas in a scene, and subsequently expands the core regions to obtain the final mask that includes a smooth shadow/clear transition. The physically scaled shadow function $\Phi*$ is then applied only to the pixels in the final mask.

The histogram of the unscaled shadow function Φ can be employed to separate regions of low values of Φ from the moderate-to-high values, compare Figure 4-10. A threshold Φ_T can be set in the vicinity of the local histogram minimum (Φ1) and the core shadow mask is defined by those pixels with $\Phi(x, y) < \Phi_T$. The details of the choice of Φ_T are discussed below. As always with thresholding, some arbitrariness is involved in the final selection.

Once the core shadow mask has been defined, it is expanded to include the surrounding shadow / clear transition zone of 100 m width. De-shadowing with the scaled shadow function Φ^* is then exclusively applied to the pixels in this final mask. This means the direct solar flux (*E*dir term in equation (0.21)) has to be multiplied with $\Phi^*(x, y)$:

$$\rho_i(x,y) = \frac{\pi(d^2\{c_0(i) + c_1(i)DN_i(x,y)\} - L_{p,i})}{\tau_i\{E_{dir,i}\Phi^*(x,y) + E_{dif,i}\}} \tag{0.26}$$

4.7 Reflectance retrieval in flat terrain

The radiation transfer for a large homogeneous Lambertian surface of ground reflectance ρ is described by [23], [16]

$$L(\rho) = L_p + \frac{\tau\ E_g(0)\ \rho/\pi}{1 - s\rho} = L_p + \tau\ E_g(\rho)\ \rho/\pi \tag{0.27}$$

where *L*, *L*p, *τ*, *E*g(0), and s are the total at-sensor or TOA radiance, path radiance, total ground-to-sensor transmittance, global flux on the ground for ρ = 0, and the spherical albedo of the atmosphere, respectively. The total transmittance τ is the sum of the direct and diffuse transmittances, i.e., τ = *τ*dir + *τ*dif . The global solar flux on the ground consists of a direct and a diffuse hemispherical component, i.e., *E*g = *E*dir + *E*dif . The wavelength or spectral channel index has been omitted for clarity.

As Sentinel-2 L1 data is already converted into TOA reflectance and S2AC needs scaled radiance as input, the TOA reflectance has to be converted into TOA radiance

$$L(k) = \frac{E_s(k)\cos\theta_s}{\pi d^2}\,\rho_{TOA}(k) \tag{0.28}$$

where k, E_s , θ_s , and d are band index, extraterrestrial solar irradiance for an astronomical distance of 1, solar zenith angle, and sun-earth distance in astronomical units, respectively. E_s depends on the spectral solar irradiance database. The one selected by ESA might differ from the one used in S2AC / libRadtran and an adjustment is needed in this case.

Equation (0.29) is a special form of the usual relationship between the measured digital number (DN) and the at-sensor radiance

$$L(k) = c_0(k) + c_1(k)DN(k) \tag{0.29}$$

where the calibration offset $c_0 = 0$ and the calibration gain is

$$c_1(k) = \frac{E_s(k)\cos\theta_s}{\pi d^2} \tag{0.30}$$

In the following description we use DN = ρ_{TOA} .

In case of image data, the surface reflectance varies from pixel to pixel and equation (0.27) has to be iterated.

Step 1: The influence of the neighbourhood (adjacency effect) is neglected and the surface reflectance is obtained from

$$\rho^{(1)} = \frac{\pi\ [d^2\ (c_0 + c_1\ DN) - L_p]}{\tau\ E_g} \tag{0.31}$$

The factor d^2 takes into account the sun-to-earth distance (d is in astronomical units) since the LUTs with the path radiance and the direct and diffuse solar fluxes are calculated for d=1.

Step 2: The second step calculates the average reflectance in a large neigborhood of each pixel (typical range R=1 km)

$$\bar{\rho} = \frac{1}{N^2}\sum_{i,j=1}^{N}\rho_{i,j}^{(1)} \tag{0.32}$$

where N corresponds to the number of pixels for the selected range R of the adjacency effect [5]. The exact choice of R is not critical since the adjacency influence is a second-order effect. Instead of the range-independent weighting in equation (0.32), a range-dependent function could be selected with an exponential decrease of the weighting coefficients [5]. However, except for special landscapes the average reflectance over a large adjacency box (2 R x 2 R) usually does not change much as a function of range, because field patterns are repeated, so a range-independent weighting is recommended as it reduces the processing time.

Step 3: The reflectance of equation (0.31) is corrected for the adjacency influence

$$\rho^{(2)}(x,y) = \rho^{(1)}(x,y) + q\{\rho^{(1)} - \bar{\rho}(x,y)\} \tag{0.33}$$

where the function q indicates the strength of the adjacency effect. It is the ratio of the diffuse to direct ground-to-sensor transmittance, i.e.

$$q = \tau_{dif}/\tau_{dir} \tag{0.34}$$

4.8 Reflectance retrieval in mountainous terrain

In mountainous terrain the topography introduces strong brightness variations depending on the orientation of a surface element. The objective of a combined topographic / atmospheric correction is the elimination of topographic effects during the surface reflectance retrieval. Surfaces oriented to the sun and away from the sun appear brighter and darker, respectively, compared to a flat surface. These effects can clearly be observed if surface slopes exceed a certain threshold, e.g. 7◦. An accurate digital elevation model (DEM) of about the same spatial resolution as the pixel size of the instrument and a very accurate ortho-rectification are required to achieve a satisfactory topographic correction [5]. Otherwise DEM artifacts will appear in the product after topographic / atmospheric correction.

It is recommended not to perform a topographic correction in quasi-flat areas, the decision criterion is that at least 1% of the scene pixels should have slope values > 6 degrees. Otherwise, slope artifacts may appear in the corrected scene.

While the ortho-rectification needs only the terrain elevation data, the atmospheric / topographic correction requires the following additional products derived from the DEM:

map of DEM slope (unit degree) (mandatory),

map of DEM aspect (unit degree) (mandatory),

map of DEM topographically cast shadow (binary map: 1=no shadow pixel, 0=shadow pixel), optional, recommended for steep terrain and / or low solar elevation,

map of sky view factor (optional).

The sky view factor is the fraction of the visible hemisphere, i.e. for a flat terrain the sky view factor is 1, and if 50% of the hemisphere is not visible then the sky view factor is 0.5. If the sky view factor map is not specified, it will be calculated within the topographic module using an approximation with the local slope angle θn of a pixel at position (x,y) [24].

$$V_{sky}(x,y) = cos^2(\theta_n(x,y)/2) = \frac{1 \; + \; cos(\theta_n(x,y))}{2} \tag{0.35}$$

A more accurate method employs a ray tracing algorithm to calculate the sky view factor, e.g., [25], [26]. However, the accurate algorithm is only needed in case of terrain with steep slopes.

Compared to the flat terrain where the TOA radiance consists of three radiation components (path radiance, pixel reflected and adjacency radiation) we need one additional radiation component in a rugged terrain, the terrain reflected radiation, see Figure 4-11 for a schematic sketch of the radiation components and the different sky view methods. The terrain reflected radiation is obtained from the average reflectance in a certain neighborhood (radius 0.5 km) weighted with the terrain view factor and multiplied with the global solar flux. The terrain view factor is related to the sky view factor:

$$V_t(x,y) = 1 \; - \; V_{sky}(x,y) \tag{0.36}$$

The solar and DEM geometry is shown in Figure 4-12 as well as the three solar radiation components taken into account for rugged terrain: direct and circumsolar irradiance, and diffuse hemispherical sky flux. It can be shown that these three components are equivalent to the direct and diffuse solar flux components in a flat terrain. In case of a topographic shadow pixel the direct and circumsolar components are set to zero.

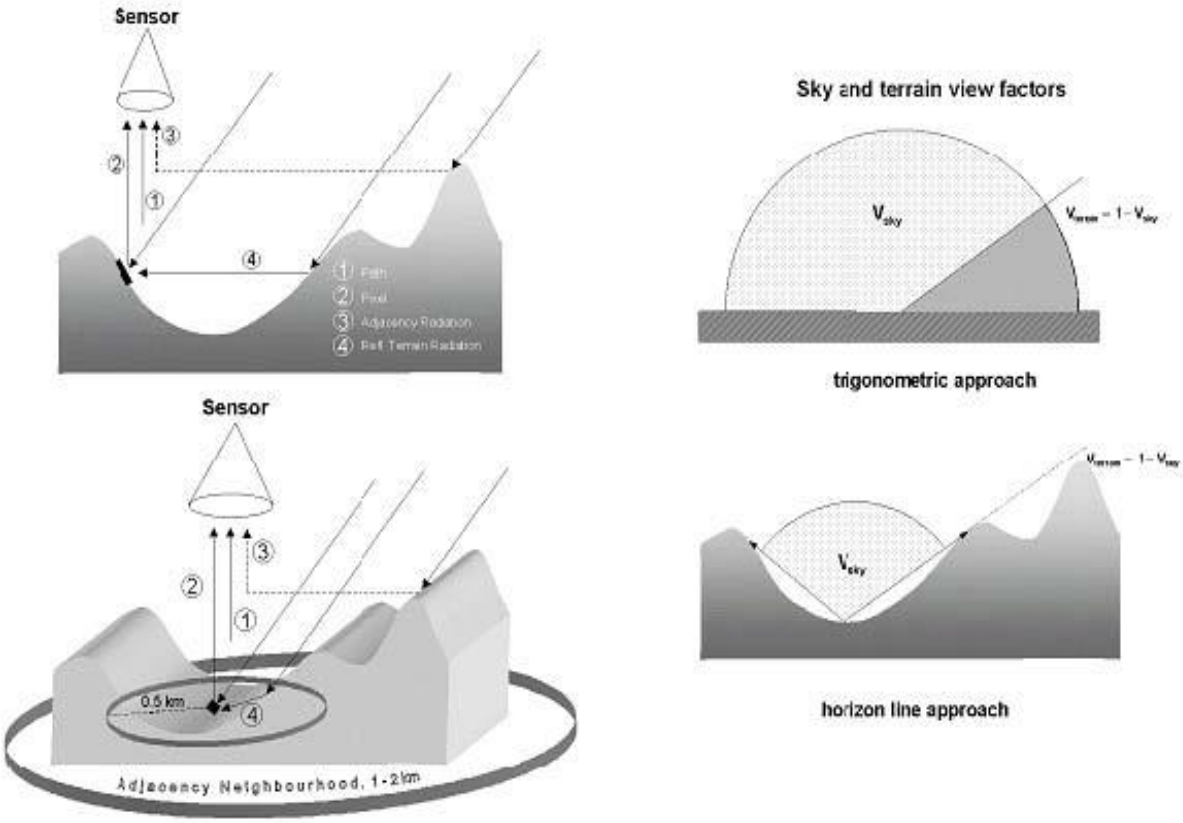

Figure 4-11 – Radiation components in rugged terrain, sky view factor

Left: schematic sketch of radiation components in rugged terrain; 1: path radiance; 2: pixel reflected radiance; 3: adjacency radiance; 4: reflected terrain radiance. Right: sky and terrain view factor.

Similar to the flat terrain case, we also calculate the reflectance iteratively. The first step neglects the adjacency effect and starts with a fixed terrain reflectance of $\bar{\rho}^{(0)}_{terrain} = 0.1$ [5]:

$$\rho^{(i)}(x,y) = \frac{\pi\ [d^2(c_0 + c_1 DN(x,y)) - L_p(z,\theta_v,\phi)]}{\tau(z,\theta_v)[b(x,y)E_s\tau_s(z)cos\beta(x,y) + E^*_{dif}(x,y,z) + E^{i)}_t(z,\rho_r)\bar{\rho}^{(i-1)}_{terrain}V_t(x,y)]} \tag{0.37}$$

The super-script index (i) denotes the iteration step. The terms are defined as:

x, y	horizontal coordinates, corresponding to the georeferenced pixel positions;
z	vertical coordinate, containing the elevation information from the DEM;
DN(x,y)	digital number of georeferenced pixel;
θv	sensor view (tilt) angle ;
*L*p(*z*, *θ*v, *φ*)	path radiance, dependent on elevation and viewing geometry;
*τ*v(*z*, *θ*v)	ground-to-sensor view angle transmittance, direct plus diffuse components;
*τ*s(*z*)	sun-to-ground beam (direct) transmittance;
β(*x*, *y*)	angle between the solar ray and the surface normal (illumination angle);

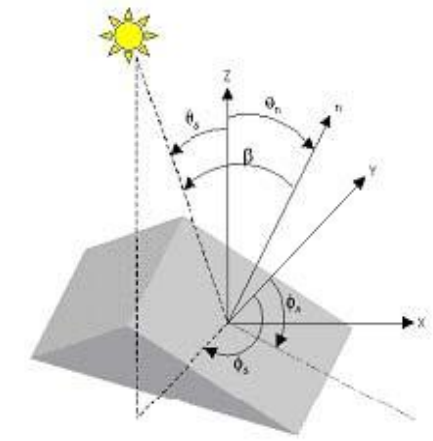

Geometry of solar illumination

$$\cos\beta = \cos\theta_s \cos\theta_n - \sin\theta_s \sin\theta_n \cos(\phi_s - \phi_n)$$

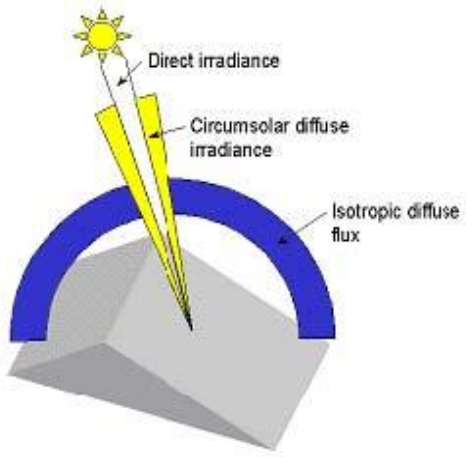

Direct and diffuse radiation components

Figure 4-12 – Solar illumination geometry and radiation components

b(x,y)	binary factor: b=1 if pixel receives direct solar beam, otherwise b=0;
E_s	extraterrestrial solar irradiance (earth-sun distance d=1 astronomical unit);
$E_d^*(x, y, z)$	diffuse solar flux on an inclined plane (see equation (0.40));
$E_g(z)$	global flux (direct plus diffuse solar flux on a horizontal surf. at elevation z);
$E_t(z)$	radiation reflected from adjacent slopes;
$\rho_{terrain}^{(0)}$	= 0.1, initial value of average terrain reflectance;
$\bar{\rho}_{terrain}^{(i)}(x, y)$	locally varying average terrain reflectance, calculated iteratively (i=1,2,3);
$V_t(x, y)$	terrain view factor (range 0-1).

The next step iterates equation (0.37) averaging the reflected terrain radiation over a square box of 0.5 × 0.5 km. If equation (0.37) is used with $E_t = E_g$ then three iterations are usually sufficient to be independent of the start value of the terrain reflectance [5]. However, for highly reflective surfaces, e.g. snow, and high terrain view factors, more than three iterations are necessary, and a faster convergence of $\bar{\rho}_{terrain}^{(i)}$ can be achieved with a geometric series for the terrain reflected radiation E_t as proposed in [22]:

$$E_t^{(i)} = E_g \frac{\bar{\rho}_{terrain}^{(i-1)} V_t}{1 - \bar{\rho}_{terrain}^{(i-1)} \bar{V}_t} \tag{0.38}$$

The last step accounts for the adjacency effect (equation (0.33)).

If $\theta s, \theta n, \varphi s, \varphi n$ denote solar zenith angle, terrain slope, solar azimuth and topographic azimuth, respectively, the illumination angle β can be obtained from the DEM slope and aspect angles and the solar geometry:

$$cos\beta(x,y) = cos\theta_s \; cos\theta_n(x,y) + sin\theta_s \; sin\theta_n(x,y) \; cos\{\phi_s - \phi_n(x,y)\} \tag{0.39}$$

The illumination image $cos\beta(x, y)$ is calculated within S2AC and stored as a separate map. The diffuse solar flux on an inclined plane is calculated with Hay's model [27] taking also into account the binary topographic cast shadow factor b:

$$E_d^*(x,y,z) = E_d(z) \; [b \; \tau_s(z) \; cos\beta(x,y)/cos\theta_s + \{1 - b \; \tau_s(z)\} V_{sky}(x,y)] \tag{0.40}$$

4.9 Empirical BRDF correction

For many surface covers the reflectance increases with increasing solar zenith and / or viewing angle [30]. Scenes in mountainous regions often exihibit a large variation of terrain slopes, and thus bidirectional brightness variations for a certain surface cover, e.g. meadow or forest. This behaviour cannot adequately be eliminated with the Lambertian assumption. It leads to overcorrected reflectance values in faintly illuminated areas (having small values of $cos\beta$), see Figure 4-13 (left). The center part of this Figure shows the result of an empirical correction with a simple geometric function depending on the local solar zenith angle β as explained below. Obviously, some correction is needed to avoid a misclassification of these bright overcorrected areas. Several approaches have been pursuit to solve this problem:

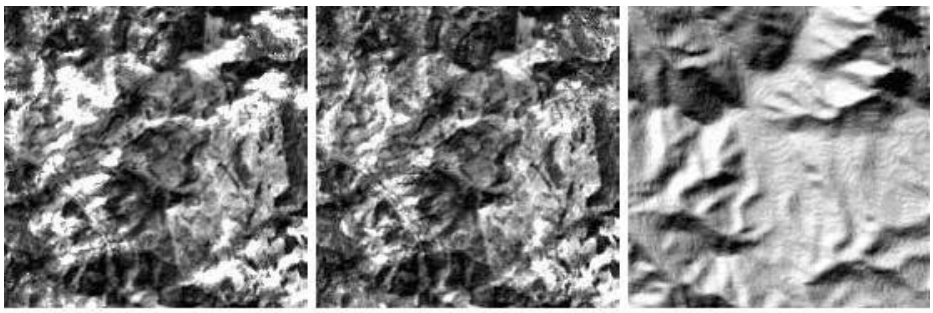

Figure 4-13 – BRDF correction in rugged terrain imagery
Left: image without BRDF correction.
Center: after BRDF correction with threshold angle βT = 65◦.
Right: illumination map = cos β

an empirical coefficient C is calculated based on a regression of brightness values and the local ilumination angle derived from the DEM. The coefficient depends on scene content and wavelength ([31], [32]).

the sun-canopy-sensor (SCS) geometry is employed in forested terrain instead of the solely terrain-based geometry [33].

the SCS method is coupled with the C-correction [34].

a simplified empirical approach accounting for the direct and diffuse illumination and incidence and exitance angles applied to vegetation canopies [35].

These approaches produced good results on sample scenes with uniform cover types presented in the above papers. When applying the methods to a wider range of areas, some of the practical problems are:

mountainous scenes often contain a number of different covers, e.g., deciduous forest, coniferous forest, mixed forest, shrubs, meadow, rocks, etc.

the computation of the C coefficients for different surface covers would require a pre - classification.

the correlation obtained for the C coefficients is often less than 0.7, yielding unreliable results with this method.

These remarks are supported by reference [32]. These authors applied different correction approaches to a TM scene containing different cover types and noted that there is no optimum method for all cover types. A drawback of the Minnaert and empirical C-methods is that they do do not distinguish between the direct and diffuse solar illumination as opposed to the physically based approach of S2AC. Nevertheless, the latter approach also cannot avoid problems in faintly illuminated areas. Therefore, it is supplemented by an empirical method with three adjustable parameters (βT , *b*, and *g*) as explained below. This approach was tested on different rugged terrain scenes with vegetated and arid landscapes and usually yields satisfactory results. It reduces overcorrected reflectance values starting at a threshold local solar zenith angle βT greater than the scene's solar zenith angle θs. Equation (0.41) defines the implemented basic geometric correction function which depends on the local solar incidence angle (solar illumination βi) and the threshold angle β_T . The exponent b (= 1/3, 1/2, 3/4, or 1) is the second parameter and can be selected by the user. Some guidelines on the choice of b are discussed below. The third adjustable parameter is the lower bound g of the correction function, see Figure 4-14.

$$G = \{cos\beta_i / cos\beta_T\}^b \qquad \leq g \tag{0.41}$$

The threshold illumination angle β_T should have some margin to the solar zenith angle to retain the original natural variation of pixels with illumination angles close to the solar zenith angle. The threshold angle can be specified by the user and the following empirical rules are recommended:

$\beta_T = \theta_s + 20^\circ$ *if* $\theta_s < 45^\circ$

If $45 \leq \theta_s \leq 20^\circ$ then $\beta_T = \theta_s + 15^\circ$

If $\theta_s > 55^\circ$ then $\beta_T = \theta_s + 10^\circ$

These rules are automatically applied if $\beta_T = 0$, e.g., during batch processing.

The geometric function G needs a lower bound g to prevent a too strong reduction of reflectance values. Values of G greater than 1 are set to 1, and values less than the boundary g are reset to g. This means the processing works in the geometric regime from βT to 90◦and the updated reflectance is

$$\rho_g = \rho_L G \tag{0.42}$$

where ρ_L is the isotropic (Lambert) value.

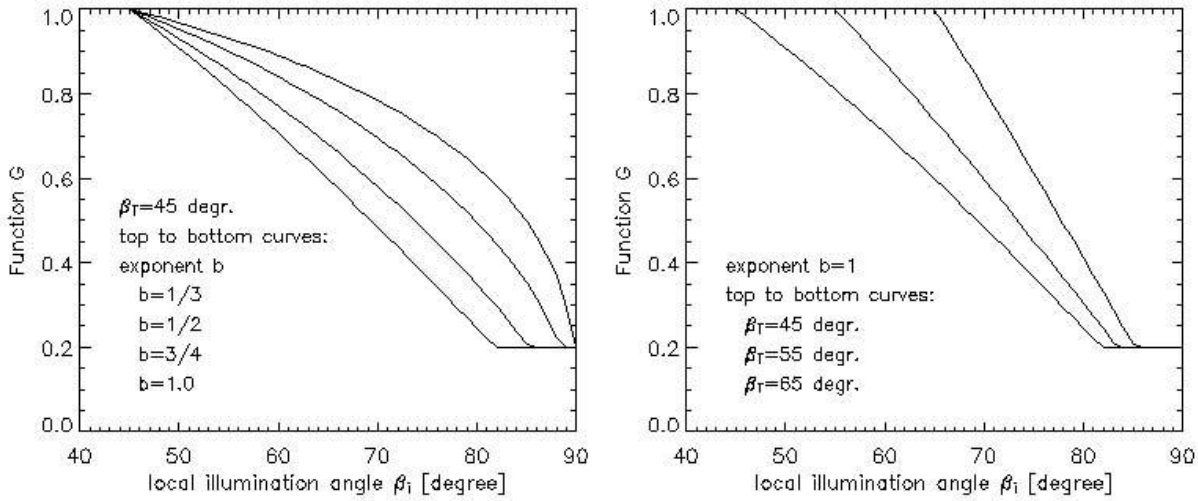

Figure 4-14 – Geometric functions for empirical BRDF correction

Left: Functions G of equation (0.41) for different values of the exponent b.
Right: Functions G of equation (0.41) for b=1 and different start values of βT.
The lower cut-off value is g=0.2.

Figure 4-14 shows a graphical presentation of equation (0.41). The left part displays the function G for different values of the exponent b. For b=1 the decrease with β_i is strong with a constant gradient. For smaller values of b the decrease with β_i is moderate initially, but the gradient increases with larger βi. Currently, different functions G for soil/sand and vegetation can be selected in S2AC [49]. The function G for soil / sand is applied with a wavelength-independent exponent b. After testing a large number of vegetated mountainous scenes two vegetation modes were finally selected because of their good performance:

1. b=0.75 for channels with λ< 720 nm and b=0.33 for λ> 720 nm (”weak” correction),

b=0.75 (λ< 720 nm) and b=1 (λ> 720 nm), (”strong” correction).

In most of the tested cases, the first vegetation mode (”weak” correction) was appropriate. A simple criterion (vegetation index ρ850nm/ρ660nm > 3) is used to distinguish soil/sand and vegetation. The right part of Figure 4-14 shows the effect of shifting the threshold illumination angle β_T . For larger values of β_T the decline of function G starts later with a larger gradient, and the lower bound g is met at slightly higher values of βi. In most cases, g=0.2 to 0.25 is adequate, in extreme cases of overcorrection g=0.1 should be applied.

Reference [7] contains a comparison of different topographic correction methods for several Landsat-TM, ETM+, and SPOT-5 scenes from different areas. The proposed empirical S2-AC approach performed best in most of these cases, but no method ranked first in all cases.

4.10 Adjacency effect

The adjacency effect depends on the aerosol height distribution (among other factors). As this height distribution is not known for operational purposes, a typical adjacency range of 1 km is assumed, i.e., the standard adjacency kernel window size is 2 km. The adjacency range is not a critical parameter, as the influence of the adjacency effect primarily depends on the pixel-to-background reflectance contrast and field patterns tend to repeat itself, i.e. the average reflectance in a 2 km adjacency window is usually very close to the value for a 4 km window. In addition, the adjacency range shall be one of the input parameters, so it can be specified if desired.

4.11 Algorithm validation

The AC algorithms proposed in this document derive from ATCOR [47] and were continually validated over a time period of more than 10 years. Comparisons were conducted with in-situ reflectance measurements, mainly during EU and ESA campaigns [53], [54], [55]. The validations comprised a large range of surface covers, atmospheric conditions, and solar geometries.

A comparison with an independent approach based on the SMAC / 6S codes was recently performed for ETM+ data and a simulated S2 scene based on spectrally resampled AVIRIS data [S2-L2A-TN5].

This Page Is Intentionally Blank

APPENDIX A Processing Strategy on continuous data strips

APPENDIX A describes a new strategy on the Sentinel-2 (S2) aerosol retrieval for long strips of continuous data acquisition.

A.1 *Introduction*

The new strategy is applicable to a long strip (e.g. 15,000 km) of S2 data to avoid AOT steps between successive S2 scenes. There can be up to $n_x=4$ tiles in the across-track direction, and the number of tiles n_y in the along-track direction depends on the strip length and along-track tile size. For technical reasons (faster array addressing with integers), the aerosol processing is conducted with the visibility index VI (discrete integers, range 0 – 183) instead of visibility or AOT. The VI range (0 – 183) corresponds to the visibility range 190 – 5 km, and an AOT(550nm) range from 0.053 to 1.15. A VI step of 1 corresponds to an AOT increment of 0.006.

The new strategy requires two runs of ATCOR: the first run performs the AOT/VI retrieval for the long strip of S2 data, the second run employs this VI map and conducts the water vapor and surface reflectance retrievals per tile. As the AOT/VI retrieval is conducted on a 60 m grid, the corresponding image data (bands B4, B12) have to be resampled to 60 m. It is proposed to perform the long-strip AOT/VI retrieval with the geometry of the original geometrically uncorrected image. This means the number of across-track pixels is about 5,000 (exactly 290 km / 0.06 = 4834). The same number of image lines can be taken (i.e. a 300 km strip length), yielding tiles of approximate size 5,000 × 5,000 pixels, which is not a processing problem for a modern PC, compare Figures 2, 3.

For the two ATCOR runs a separate ATCOR wrapper is needed, consisting of the AOT/VI loop for the requested number of tiles (n_y), and the water vapor / surface reflectance loop.

First part of wrapper:

The first part of the wrapper with the AOT/VI retrieval consists of $n_y= (S/ 60)$ or $n_y= (S/ 60)+1$ tiles in along-track direction, where S = strip length in meters. For each of these tiles, the solar and view geometry at the tile borders have to be specified in the corresponding ATCOR (*scene_tile_number.inn*) file. In addition, the DEM file (elevation) has to be calculated and re-mapped into the IGM (Input Geometry Model) format. The wrapper has to process each AOT/VI tile, calculate the small cell AOT/VI averaging (3 km × 3 km), and store the small VI map at the appropriate location in the total compact VI array. The re-mapping to the original 60 m resolution employing a cubic spline interpolation is conducted in the second stage, see Fig. 2.

Second part of wrapper:

The second part of the wrapper could work with the same number of tiles for the processing of the 60 m configuration. However, for the 20 m and 10 m configurations, smaller tiles have to be used (e.g. of size 100 km × 100 km), implying that additional tiles in the across-track direction have to be introduced. Therefore, the number of tiles in the loop is larger in the latter cases.

The first task is the re-mapping of the compact whole strip VI map to the full-resolution (60 m pixel) employing a cubic spline interpolation and storing this information in a file. Another advantage of using the VI (instead of AOT) is that the VI depends less on elevation which reduces potential spline interpolation artifacts in mountainous terrain. If a tile with no VI reference pixels is found (i.e. no vegetation and no water), the default VI =45 (corresponding to visibility = 23 km) is taken. Another possibility would be to take the

average VI of the two adjacent tiles. In case of two or more successive tiles without reference pixels it is probably best to use the default values.

Then for each tile loop (in x= across-track and y=along-track direction), the corresponding part of the full-resolution VI map has to be read from the VI file. For the 10m/20m configurations this file needs a further appropriate resampling (and interpolation) to match the 10m / 20m resolution. Additionally, the former input files (*scene_tile_number.inn*) containing the solar and view geometry have to be updated correspondingly. Also, the complete set of DEM files (elevation, slope, aspect, skyview) has to be updated with respect to the spatial resolution (10 m, 20 m, 60 m) of the selected S2 configuration. Again, it is recommended to process the data in the original geometry format, which distinctly facilitates the processing scheme. However, this requires a re-mapping of the DEM files into the IGM system.

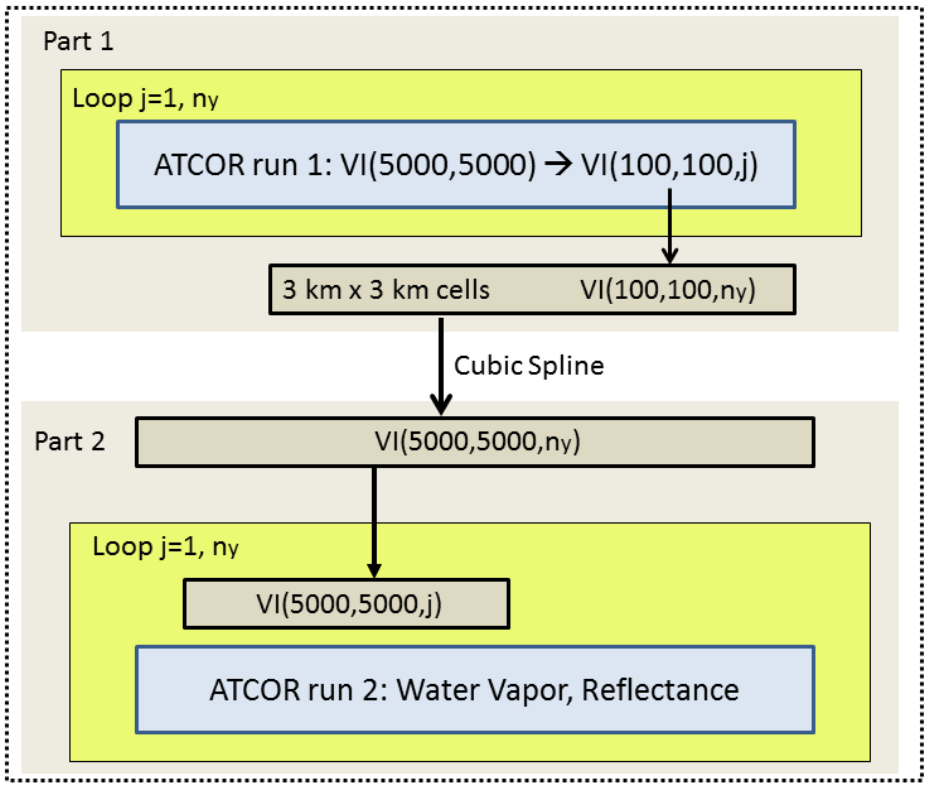

Figure 4-15 – Schematic sketch of ATCOR wrapper for tiling

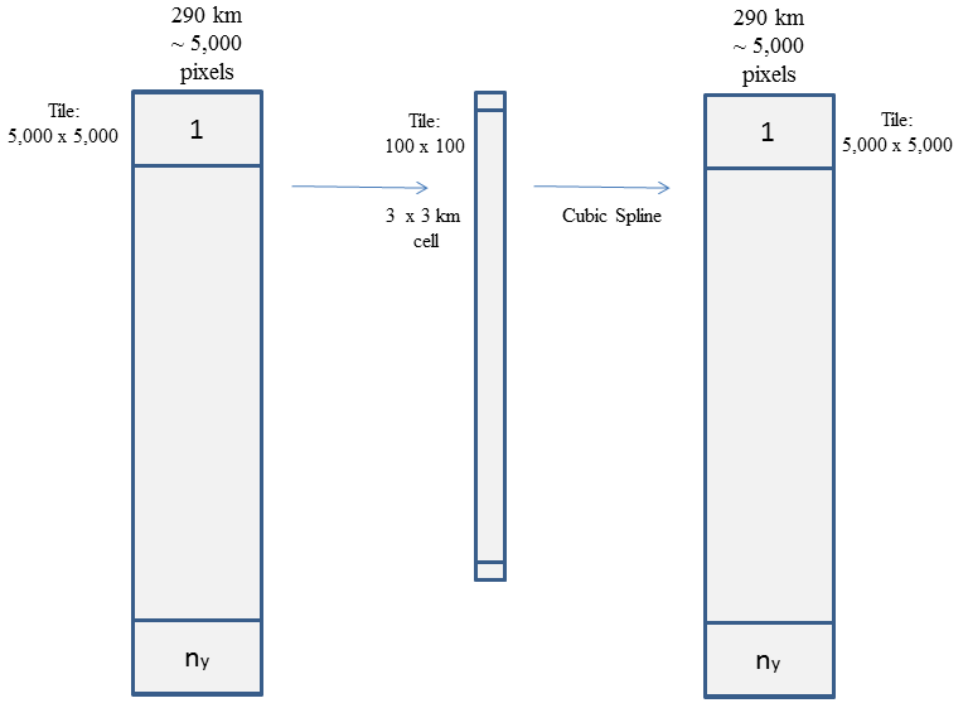

Figure 4-16 – Tiling for a long strip of S2 data using the raw geometry

A.2 Example

Strip length 15,000 km. This yields 50 tiles in along-track direction, assuming 5,000 lines at 60 m per tile.

First part of wrapper:

Assuming (for simplicity) 5,000 pixels per line, the size of the VI map (per tile) is 5,000 × 5,000 = 25 MB, because the VI can be stored with 1 byte per pixel. This array is kept in memory until the small cell (3 km × 3 km) averaging is performed. Each small cell then constitutes a grid point in the compressed VI map of size 100 × 100 pixels. Finally, after processing n_y=50 tiles, the total compressed VI map consists of 100 × 5,000 pixels, which is stored as a file of size of 0.5 MB or might be kept in memory.

In addition, all radiative transfer functions derived from the first part and needed for the retrievals of water vapor and surface reflectance have to be stored and passed to the second part of the wrapper processing.

Second part of wrapper:

Read the file of (compressed total strip) VI map, expand it to full size (5,000 columns × 50 *5,000 lines = 5,000 × 250,000 pixels) with cubic spline interpolation (array size 1.25 Giga-pixel). Although the original VI array is 1 byte/pixel, the cubic spline interpolation has to be performed on float data, yielding a temporary array size of 1.25*4 = 5 GB, which is already too big to be kept in memory. After this spline interpolation the smoothed

array can be byte-rounded, yielding a VI map of 1.25 GB, and this map has to be written to a file.

Then run 2 of the wrapper follows with a loop over all tiles, either with only in-track tiles or with combined across-track and in-track tiles. For each tile the appropriate part of the spline-interpolated VI map is read from file, the aerosol retrieval is skipped, and the water vapour and surface reflectance retrievals are conducted.

A.3 Implementation and first tests

The proposed concept was implemented in IDL. For this purpose, a wrapper *("atcor_s2w")* was written consisting of two parts:

- It performs the loop over all tiles and calls the previous program *("atcor_s2")*, which is modified to terminate after the VI/AOT calculation and store the necessary tile information.
- It reads the compressed (total strip) VI map and expands it to the full spatial resolution employing a cubic spline interpolation. Then the tile loop starts, reading the appropriate tile VI, skipping the VI/AOT calculation, and conducting the water vapor and surface reflectance retrievals. Both parts require changes in the former code of *"atcor_s2".*

The wrapper program is called with 2 parameters: the file name of the first image tile and the number of tiles e.g.:

atcor_s2w, input='/data1/s2_scene001_t01.bsq', nfiles=15 .

If the number of tiles is less than 10 the tile names should be '*_t1.bsq', '*_t2.bsq' etc. If the number is between 10 and 99, the image tile names should be '*_t01.bsq', up to '_t99.bsq', and if there are 100 tiles or more the names should be '*_t001.bsq' etc. No gaps in this sequence are allowed.

A first test of this concept was successfully performed with the previous simulated S2 scene (Bowie scene containing cirrus, Berthelot et al. 2010, Richter 2012). AOT results are shown in Fig. 4.

Figure 4-17 – AOT without (left) and with tiling (right) for a simulated S2 scene

This scene consists of 614 across-track pixels and 1400 lines. The image was split into 3 tiles: tile 1 contains lines 1 – 500, tile 2 contains lines 501 – 1000, the last one the lines 1001-1400.

For all tile images the corresponding input parameter files (i.e. *'*_t1.inn'* to *'*_t3.inn'*) with the updated view and solar geometry (and DEM files) has to be created before starting the wrapper, as well as the corresponding tile-specific DEM files. In the current test, this was done for a flat DEM (the elevation file contains a constant height of 100 m for all pixels, and the slope / aspect files contain 0 for all pixels). In addition, the current test scene is already in the proposed raw geometry.

Fig. 5 presents a true color composite (RGB = bands B4, B3, B1) of the results without and with tiling. It is clear that the AOT differences of Fig. 4 will influence the RGB rendition, especially for the AOT sensitive bands in the visible part of the spectrum.

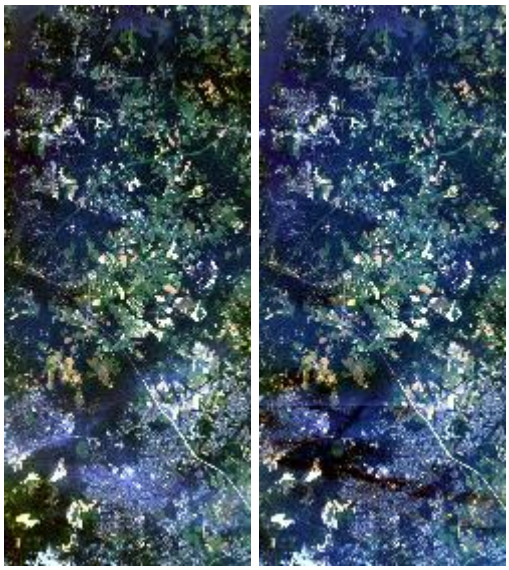

Figure 4-18 – Surface reflectance scene (RGB = 665, 560, 443 nm)), left: no tiling, right: tiling

Of course, this scene is not representative for the final S2 image size, but it is sufficient for testing the proposed tile processing concept. The differences between the AOT maps in Fig. 4 are due to two factors:

1. the cirrus removal (performed per tile versus for the whole scene), because the cirrus part is subtracted before the aerosol retrieval), and
2. the distribution of dark reference pixels in the scene.

These differences are enhanced because of the small scene size. They will be much smaller for a large scene. Nevertheless, the dynamic range of AOT is very similar (0.12 – 0.28 in case of no tiling, 0.10 – 0.26 for the tiled scene).

A.4 Summary

A new concept has been developed to enable the processing of a long strip of S2 data using small tiles during the aerosol retrieval. The first pass of the atmospheric correction performs the aerosol retrieval for the whole strip on a per tile basis, averaging the visibility index for small cells (3 km × 3 km), and using a compact 3 km grid for the whole strip. The second pass resamples this compact map to the full original size employing a cubic spline interpolation to avoid steps of the visibility index / AOT at tile borders. The

last step uses the interpolated aerosol map and retrieves the water vapor map and the surface reflectance cube.

A first version of this concept for the 60 m S2 configuration was implemented and tested in IDL. In order to facilitate the processing in terms of code complexity and to ease memory requirements, it is recommended to use the original geometrically uncorrected scene. The tile processing is coded in a separate ATCOR wrapper program ("*atcor_s2w"*) calling the existing code ("*atcor_s2"*) which had to be modified to support the new tiling concept.

APPENDIX B Kohonen Self Organizing Map

APPENDIX B describes the theoretical background for the algorithm used for the cloud shadow detection in section 3.4.1.

A Kohonen map algorithm was used to generate a typical “dark area” TOA reflectance spectrum[10]. The dark area spectrum then was extrapolated to a Sentinel-2 spectrum, reflecting the wavelength centres for the six Sentinel-2 MSI bands of interest (bands 2, 3, 4, 8, 11 and 12). The resulting spectrum is used as a look up table for processing a classification mask on potential cloud shadows using a minimum distance algorithm on each reflectance pixel of each of the six spectral bands. The configured threshold for the dark area classification is validated by an off line comparison with the database of the Kohonen map. The initial generation of the Kohonen Map algorithm, which was processed and trained offline will be described in the following.

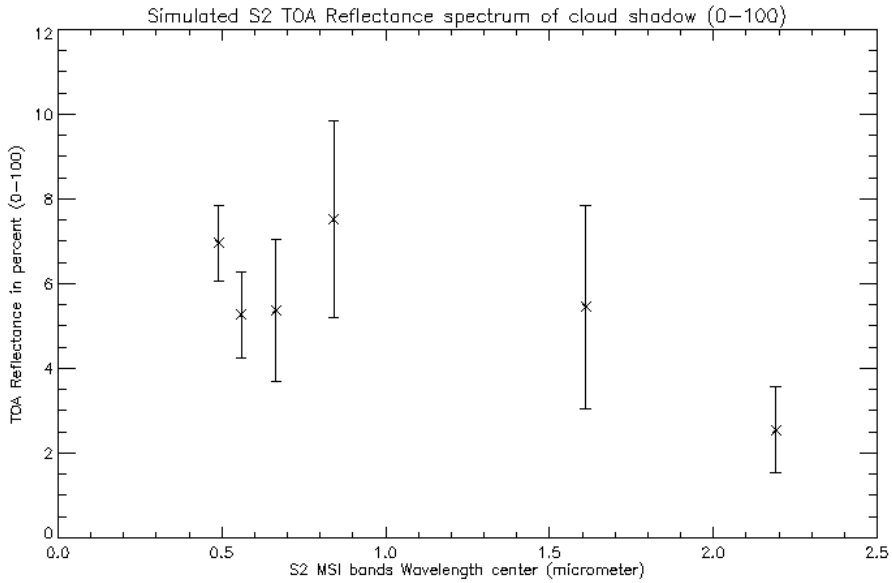

Figure 19 - Simulated S2 TOA reflectance of Cloud Shadow for (bands 2, 3, 4, 8, 11 and 12) and related error bars.

B.1 Theoretical Background

The neural networks method applied in processing the Landsat data sets is a variant of the topological maps method of Kohonen. The topographical maps method is one of the first, non-supervised, automatic neural networks learning models implemented, and it is closely associated through theoretical studies to statistical methods of automatic classification, such as the non-linear principal component analysis and the density function approximation.

The algorithm proposed by Kohonen is a self-organising algorithm that projects the entry data space (a multi-dimensional matrix) on a lower dimension field (of typical dimension 1 2 or 3), known as “topological map”, and hereby referred to as C. The purpose of this projection is to partition great numbers of observations in groups of similar characteristics. However, the Kohonen algorithm allows the realised groupings to have a neighbourhood structure that can be materialized through a topological map.

[10] *Landsat ETM+ TOA has been used as source data set for training the network.*

A Kohonen's map architecture is comprised of two interconnected layers: The input layer and the topological map.

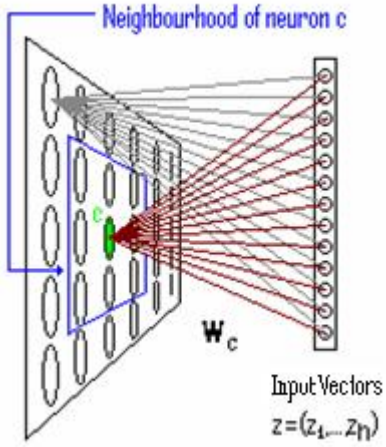

Figure 4-20: Neural Network

The sole function of the input layer is to present to the network the data (input vectors) to be processed. The neurons take the dimension of the input vectors. During the research the dimension of each neuron has been 5,6,7,8 or 9 depending on the parameters we were exploring at the time.

The topological map is a grid space of regular structure and of low dimension (2 or 3). Each grid intersection is a neuron. The map geometry is predetermined during its conception. The linking between the neurons of C is done through a non-oriented graph structure, which induces a discrete distance d on C. For each couple of neurones (c,r) of C, d(c,r) is thus defined as being the length of the shortest path between c and r on the C grid.

For each neuron c, this distance function allows for the definition of a neighbourhood (as a zone of influence surrounding each neuron). This notion in turn imposes topological constrains upon the final map structure representation.

$$K^{h(t)}\ d\ c,r\ = \exp\left(\frac{-d\ c,r}{2h\ t}\right)$$

The kernel function is used to manage the span of each neighbourhood. This function is dependant of h(t) called temperature function, which decreases after each iteration of the algorithm, and of the distance d. the variables c and r represent neurones. The influence that one neuron has on another when altered is inversely dependant to their distance and the temperature parameter. It is an iteration counter and therefore is a natural number.

Conforming to the majority of the artificial neural networks algorithms, Kohonen maps operate in two modes: training and mapping.

B.2 Training

If we represent by wc the weight vectors that connect each neuron of the grid space with the values of the input layer, then these vectors are the parameters processed during the training phase of the SOM. The training is done in a predetermined number of iterations. Each iteration is conducted in two sub-periods.

During the first period each point of the input vector is affected to a specific neuron by

the affection function: $\chi(z) = \arg\min_{c} ||z - wc||2$

After the best matching map unit c is found the data point z will be associated to the class which is represented by the neuron c.

During the second period (or update period) the neurons modify their respective weight vectors wc. The self-organising aspect of the map only allows for an update in the vicinity of the most active areas, meaning the neighbourhood of the best matching neurone.

The update of the i-th weight vector wc (the weight vector Wci) is calculated by:

$$ {}_{t+1}w_{c_i} = \begin{cases} {}_{t}w_{c_i} + \alpha(t) * K^{h(t)}(d(c,g)) * (z_i - {}_{t}w_{c_i}) & \text{for} \quad K^{h(t)}(d(c,g)) > 0.001 \\ {}_{t}w_{c_i} & \text{for} \quad K^{h(t)}(d(c,g)) < 0.001 \end{cases} $$

With α(t) being the training step function, which decreases after each iteration, and the cut-off limit for Kh(t)(d(c,g)) determined by the user (depending on the required accuracy of the results, the computing power and availability of time).

Near the end of training, the weight vector of each neurone converges towards a value such as he will no longer be able to be active but for a very limited and well determined neighbourhood of observations from the input vector. Each neuron has a part of the input vector's data attributed to it:

Zc={zp| with p the index value of the attributed data points.}.

Each such grouping of values is represented by the vector of reference of the group, rwc. The vector of reference rwc is none other than the weight vector wc arriving to the neuron c at the end of the training season.

The purpose of the training of self-organising maps is to create referent vectors that best represent the underlying probability density of the data set. The network will approximate the neighbourhood relationships of the different sub groupings of the training batch. This imposes to neighbouring neurones on the map to have referent vectors that are close in the Euclidian distance sense, upon the data space.

The initial grid form can be selected manually by the user, and it usually represents the anticipated complexity of the map. The som toolbox for matlab does a principal component analysis of the data space, and then selects the length and width of the grid to be proportional to the main eigenvectors calculated by the principal component analysis.

After the training period, the Kohonen map is a structured presentation of the data set studied, and we can then use it to interpret data.

B.3 Mapping of SOM

Mapping is usually an easy evaluation (through minimum distance) of the best matching map unit for each pixel. However after testing with that method we discovered that there were many cases where the reference vectors of two really close classes had a similar spectral signature and such that we got corrupted results from data that came close in between two categories. Specifically the problem was to distinguish water from shadow without using thermal infrared, and differentiating some cloud classes from snow. As an additional goal of the S2PAD project was to have a probability for each neurone to belong

in cloud, non-cloud, we chose to follow our research with probabilistic self-organising maps.

B.4 Application

B.4.1 Creation of Training data sets

The final version of the training database contains 1000000 pixels, taken from 20 Landsat images, with 50000 pixels taken individually out of each of them. For each pixel the values of the pixel in each spectral band from b10 to b70, the standard derivation S50 on a five by five window of the spectral band 50, its column and line values, the zone and image from which the pixel was taken, as well as the value of the pixel on the ACCA mask are saved into a text file. 550000 pixels are cloud pixels according to the ACCA classification and 450000 are clear sky values. There are no cloud shadows pixels in this database, since these are covered in a different map. As noted above, special care has been given to also include snow and bare areas, both with and without cloud coverage. In order to do so the algorithm contains special selection functions, but the main way to achieve this was to select images that were characterised by such features. Thus the images, from which the pixels are randomly selected with the previous criteria, are handpicked from the list of available images due to their interesting properties.

B.4.2 Cloud SOM map

The SOM map that we see in Figure 4-21 is the end result of the SOM algorithm that is used as an input for the PRSOM. It was determined that no time would be spent on classifying manually each vector, since we needed probabilistic results, rather than a binary inclusion of each neuron in a specific class.

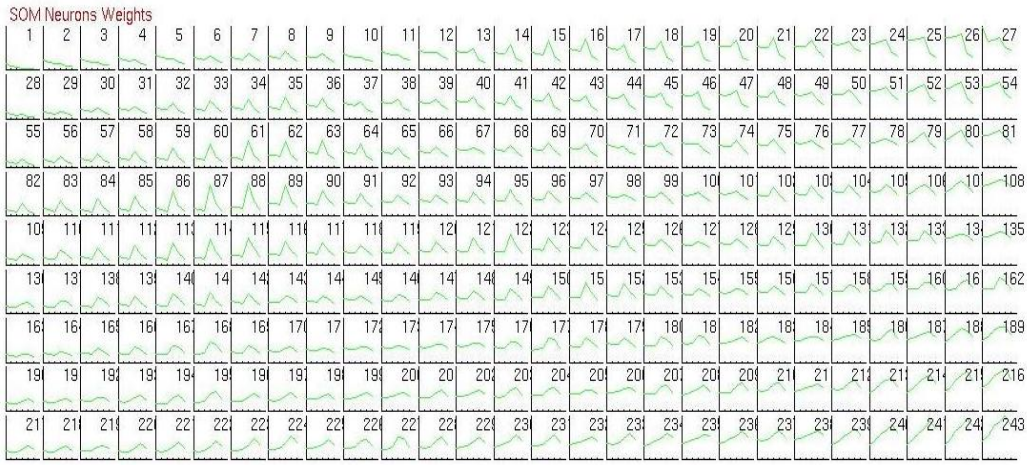

Figure 4-21: Referent Vector of the Cloud mask

However we present here some data obtained on the neurons. The matrixes are transposed.

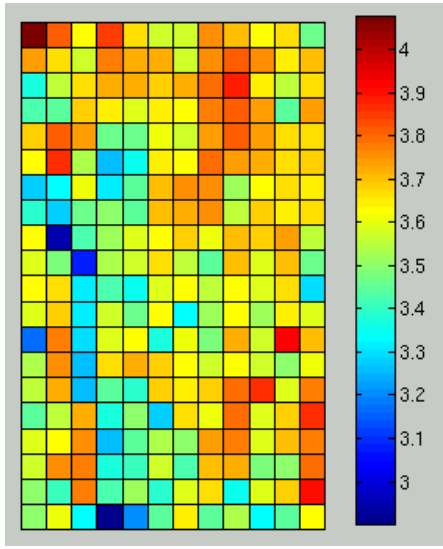

Figure 4-22: Number of hits in the training data (in log 10)

In Figure 4-22 we can see that the neurons represent well the training data, with few neurons in blue capturing a small number of data, while most of them capture a significant amount of data. The existence of red pixels in the borders signifies that these neurons might have been more centralized on a bigger map, with a longer training period. However the existences of central orange and yellow neurons (meaning neurons that have been attributed over 10.000 pixels each) indicate that the map is well trained.

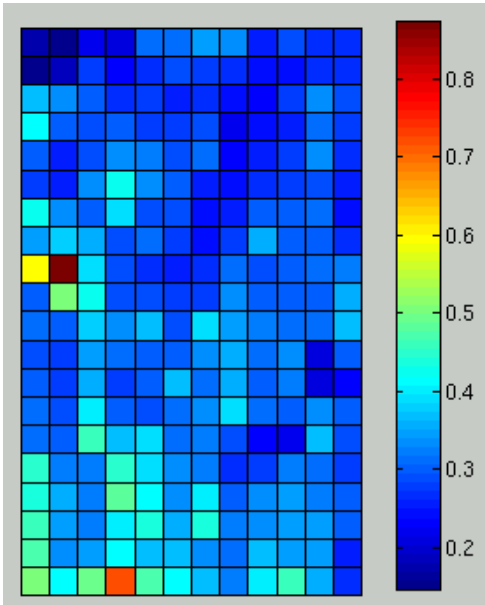

Figure 4-23: Variance of each neuron

The values seen in the Figure 4-23 reinforce the previous statements, since the variance is generally low, indicating that the neurons are well placed inside the data space.

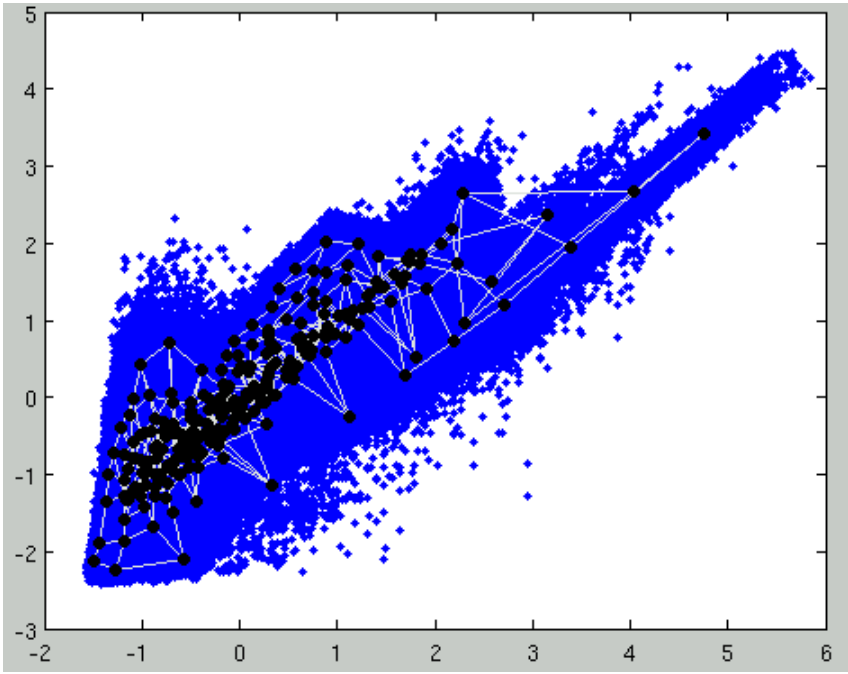

Figure 4-24: Projection of the neurons on the bands 20 and 40 of the training data set

In Figure 4-24 we projected the neurons on the intersection plane of band 20 and band 40. The image might be a bit misleading since neurons may seem to miss very density areas big, yet we must bear in mind that the training database contains 1000000 pixels, and thus we cannot really perceive density agglomerations in this image. We can however perceive that neurons have generally embraced the shape of the data. The values on the axis can be negative since the database was normalised before executing the SOM.

We can note that pixel number one has amassed a great number of pixels, and has a very low variance. This is due to its reference vector: it has values that are close to zero and therefore represent either cloud shadows or water.

APPENDIX C Bibliography

[4] Richter, R., ”A spatially adaptive fast atmospheric correction algorithm”, *Int*. *J*. *Remote Sensing*, Vol. 17, 1201-1214 (1996).

[5] Richter, R., ”Correction of satellite imagery over mountainous terrain”, *Applie*d *Optics*, Vol. 37, 4004-4015 (1998).

[6] Richter, R., and Schläpfer, D., ”Considerations on water-vapour and surface-reflectance retrievals for a spaceborne imaging spectrometer”, *IEE*E *Trans*. *Geosci*. *Remote Sensing*, Vol. 46, 1958-1966 (2008).

[7] Richter, R., Kellenberger, T., and Kaufmann, H., ”Comparison of topographic correction methods”, *Remote Sensing*, Vol. 1, 184-196 (2009).

[8] Tanre, D., Deroo, C., Duhaut, P., Herman, M., and Morcrette, J.J., ”Description of a computer code to simulate the signal in the solar spectrum: the 5S code”, *Int*. *J*. *Remote Sensing*, Vol. 11, 659-668 (1990).

[9] Vermote, E.F., Tanre, D., Deuze, J.L., Herman, M., and Morcrette, J.J., ”Second simulation of the satellite signal in the solar spectrum, 6S: an overview”, textitIEEE Trans. Geosci. Remote Sensing, Vol. 35, 675-686 (1997).

[10] Rahman, H., and Dedieu, G., ”SMAC: a simplified method for the atmospheric correction of satellite measurements in the solar spectrum”, *Int*. *J*. *Remote Sensing*, Vol. 15, 123-143 (1994).

[11] Schläpfer, D., Borel, C.C., Keller, J., and Itten, K.I., ”Atmospheric precorrected differential absorption technique to retrieve columnar water vapour”, *Remote Sens*. *Environ.*, Vol. 65, 353366 (1998).

[12] Chylek, P., Borel, C.C., Clodius, W., Pope, P.A., and Rodger, A.P., ’Satellite-based columnar water vapour retrieval with the multi-spectral thermal imager (MTI)”, *IEE*E *Trans*. *Geosci*. *Remote Sens.*, Vol. 41, 2767-2770 (2003).

[13] Rodger, A., and Lynch, M. J., ”Determining atmospheric column water vapour in the 0.4-2.5 μm spectral region”, Proceedings of the AVIRIS Workshop 2001, Pasadena, CA (2001).

[14] Pearce, W. A., ”A study of the effects of the atmosphere on Thematic Mapper observations”, report 004-77, EG&G Washington Analytical Services Center, Inc., Riverdale, MD, (1977).

[15] Dave, J. V., ”Effect of atmospheric conditions on remote sensing of a surface nonhomogeneity”, *Photogramm*. *Eng*. *Remote Sens.*, Vol. 46, 1173-1180 (1980).

[16] Kaufman, Y. J., ”The atmospheric effect on the separability of field classes measured from satellites”, *Remote Sens*. *Environ.*, Vol. 18, 21-34 (1985).

[17] Richter, R., Bachmann, M., Dorigo, W., and Müller, A., ”Influence of the adjacency effect on ground reflectance measurements”, *IEE*E *Geosci*. *Remote Sensing Letters*, Vol. 3, 565-569 (2006).

[18] Stamnes, K., Tsay, S. C., Wiscombe, W. J., and Jayaweera, K., ”Numerically stable algorithm for discrete-ordinate-method radiative transfer in multiple scattering and emitting layered media”, *Applie*d *Optics*, Vol. 27, 2502-2509 (1988).

[19] Nicodemus, F. E., ”Reflectance nomenclature and directional reflectance and emissivity”, *Applie*d *Optics*, Vol. 9, 1474-1475 (1970).

[20] Slater, P. N., ”Radiometric considerations in remote sensing”, *Proc*. *IEEE*, Vol. 73, 997-1011 (1985).

[21] Schaepman-Strub, G., Schaepman, M. E., Painter, T. H., Dangel, S., and Martonchik, J. V., ”Reflectance quantities in optical remote sensing -definitions and case studies”, *Remote Sensin*g *Environment*, Vol. 103, 27-42 (2006).

[22] Sirguey, P., ”Simple correction of multiple reflection effects in rugged terrain”, *Int*. *J*. *Remote Sensing*, Vol. 30, 1075-1081 (2009).

[23] Tanre, D., Herman, M., and Deschamps, P. Y., ”Influence of the background contribution upon space measurements of ground reflectances”, *Applie*d *Optics*, Vol. 20, 3676-3684, (1981).

[24] Kondratyev, K. Y., ”Radiation in the atmosphere”, *Academic Press*, London, (1969).

[25] Dozier, J., Bruno, J., and Downey, P., ”A faster solution to the horizon problem”, *Computer*s & *Geosciences*, Vol. 7, 145-151 (1981).

[26] Corripio, J. G., ”Vectorial algebra algorithms for calculating terrain parameters from DEMs and the position of the sun for solar radiation modelling in mountainous terrain”, Int. J. Geographical Information Science, Vol. 17, 1-23 (2003).

[27] Hay, J. E., and McKay, D. C., ”Estimating solar irradiance on inclined surfaces: a review and assessment of methodologies”, *Int*. *J*. *Sola*r *Energy*, Vol. 3, 203-240 (1985).

[28] Irish, R.R., Barker, J. L., Goward, S. N., and Arvidson, T., ”Characterization of the Landsat-7 ETM+ automated cloud-cover assessment (ACCA) algorithm” *Photogr*. *Engin*. *Remote Sens*. Vol. 72, 1179-1188 (2006).

[29] Ackerman, S. A., Strabala, K. I., Menzel, W. P., Frey, R. A., Moeller, C. C., and Gumley, L. E., ”Discriminating clear sky from clouds with MODIS”, *J*. *Geophys*. *Res.*, Vol. 103, D24, 32,141-32,157 (1998).

[30] Kriebel, K. T., ”Measured spectral bidirectional reflection properties of four vegetated surfaces”, *Applie*d *Optics*, Vol. 17, 253-259 (1978).

[31] Teillet, P. M., Guindon, B., and Goodenough, D.G., ”On the slope-aspect correxti on of multispectral scanner data”, *Canadia*n *J*. *Remote Sensing*, Vol. 8, 84-106, (1982).

[32] Riano, D., Chuvieco, E., Salas, J., and Aguado, I., ”Assessment of different topographic corrections in Landsat-TM data for mapping vegetation types”, *IEE*E *Trans*. *Geoscience and Remote Sensing*, Vol. 41, 1056-1061 (2003).

[33] Gu, D., and Gillespie, A., ”Topographic normalization of Landsat TM images of forest based on subpixel sun -canopy -sensor geometry”, *Remote Sensin*g *of Environment*, Vol. 64, 166-175 (1998).

[34] Soenen, S., A., Peddle, D. R.,and Coburn, C. A., ”SCS+C: a modified sun -canopy -sensor topographic correction in forested terrain”, *IEE*E *Trans*. *Geoscience and Remote Sensing*, Vol. 43, 2148-2159 (2005).

[35] Shepherd, J. D., and Dymond, J. R., "Correcting satellite imagery for the variance of reflectance and illumination with topography" *Int*. *J*. *Remot*e *Sensing*, Vol. 24, 3503-3514 (2003).

[36] Kaufman, Y. J., and Sendra, C., "Algorithm for automatic atmospheric corrections to visible and near-IR satellite imagery", *Int*. *J*. *Remot*e *Sensing*, Vol. 9, 1357-1381 (1988).

[37] Kaufman, Y. J., Wald, A. E., Remer, L. A., Gao, B.-C., Li, R.-R., and Flynn, L., "The MODIS 2.1 *μ*m channel -correlation with visible reflectance for use in remote sensing of aerosol", *IEE*E *Transaction*s *o*n *Geoscienc*e *an*d *Remot*e *Sensing*, Vol. 35, 1286-1298 (1997).

[38] Liang, S., Fallah-Adl, H., Kalluri, S., Jaja, J., Kaufman, Y. J., and Townshend, J. R. G., "An operational atmospheric correction algorithm for Landsat Thematic Mapper imagery over the land", *J*. *Geophys*. *Res.*, Vol 102, D14, 17,173-17,186 (1997).

[39] Kaufman, Y. J., Tanre, D., Remer, L.A., Vermote, E. F., Chu, A., and Holben, B.N., "Operational remote sensing of tropospheric aerosol over land from EOS moderate resolution imaging spectrometer", *J*. *Geophys*. *Res.*, Vol 102, D14, 17,051-17,067 (1997).

[40] Santer, R., Ramon, D., Vodot, J., and Dilligeard, E., "A surface reflectance model for the aerosol remote sensing over land", *Int*. *J*. *Remot*e *Sensing*, Vol. 28, 737-760 (2007).

[41] Gao, B.-C., Kaufman, Y.J., Han, W., and Wiscombe, W.J., "Correction of thin cirrus path radiances in the 0.4 -1.9 *μ*m spectral region using the sensitive 1.375 *μ*m cirrus detecting channel", *J*. *Geophys*. *Res.*, Vol. 103, D24, 32,169-32,176 (1998).

[42] Gao, B.-C., Yang, P., Han, W., Li, R.-R., and Wiscombe, W.J., "An algorithm using visible and 1.38 *μ*m channels to retrieve cirrus cloud reflectances from aircraft and satellite data", *IEE*E *Trans*. *Geosci*. *Remot*e *Sens.*, Vol. 40, 1659-1668 (2002).

[43] Gao, B.-C., Kaufman, Y. J., Tanre, D., and Li, R. R., "Distinguishing tropospheric aerosols from thin cirrus clouds for improved aerosol retrievals using the ratio of 1.38–*μ*m and 1.24–*μ*m channels", *Geophys*. *Res*. *Letters*, Vol. 29, No. 18, 1890, 36-1 to 36-4 (2002).

[44] Gao, B.-C., Meyer, K., and Yang, P., "A new concept on remote sensing of cirrus optical depth and effective ice particle size using strong water vapour absorption channels near 1.38 and 1.88 *μm*", *IEE*E *Trans*. *Geosci*. *Remot*e *Sens.*, Vol. 42, 1891-1899 (2004).

[45] Richter, R., "Atmospheric correction of satellite data with haze removal including a haze/clear transition region", *Computer*s & *Geosciences*, Vol. 22, 675-681 (1996).

[46] Richter, R., and Müller, A., "De-shadowing of satellite/airborne imagery", *Int*. *J*. *Remot*e *Sensing*, Vol. 26, 3137-3148 (2005).

[47] Richter, R., Schläpfer, D., and Müller, A., "An automatic atmospheric correction algorithm for visible/NIR imagery" *Int*. *J*. *Remot*e *Sensing*, Vol. 27, 2077-2085 (2006).

[48] Crist, E. P., and Cicone, R. C., "A physically-based transformation of Thematic Mapper data -the Tasseled Cap", *IEE*E *Trans*. *Geosci*. *Remot*e *Sensing*, Vol. GE-22, 256-263 (1984).

[49] Richter, R., ”Atmospheric / topographic correction for satellite imagery”, S2AC-2/3 User Guide, DLR-IB 565-01/09, DLR, Wessling (Germany), (2009).

[50] Engel, J. L., and Weinstein, O., ”The Thematic Mapper -an overview” *IEE*E *Trans*. *Geosci*. *Remot*e *Sensing*, Vol. 21, 258-265 (1983).

[51] Running, S. W., et al., ”Terrestrial remote sensing science and algorithms planned for EOS/MODIS” *Int*. *J*. *Remot*e *Sensing*, Vol. 15, 3587-3620 (1994).

[52] Kalyanaraman, S., Rajangam, R. K., and Rattan, R., ”Indian remote sensing spacecraft 1C/1D” *Int*. *J*. *Remot*e *Sensing*, Vol. 16, 791-799 (1995).

[53] ESA workshop on the Digital Airborne Spectrometer Experiment (DAISEX) ESA SP-499, ESTEC 15-16 March 2001, Noordwijk, Netherlands (2001)

[54] Richter, R., Müller, A., and Heiden, U., ”Aspects of operational atmospheric correction of hyperspectral imagery” *Int*. *J*. *Remot*e *Sensing*, Vol. 23, 145-157 (2002).

[55] Richter, R., and Schläpfer, D., ”Geo-atmospheric processing of airborne imaging spectrometry data. Part 2: atmospheric / topographic correction.”, *Int*. *J*. *Remot*e *Sensing*, Vol. 23, 26312649 (2002).

[56] Zhang, Y., Guindon, B., and Cihlar, J., ”An image transform to characterize and compensate for spatial variations in thin cloud contamination of Landsat images”, *Remot*e *Sensin*g o*f Environment*, Vol. 82, 173-187 (2002).

[57] Berthelot, B., Louis, J., and Richter, R., “Sentinel-2 MSI – Selection of algorithms for level 2A products generation”, ESA contract 21450/08/I-EC (2010).

[58] Irish Richard R., “Landsat 7 Automatic Cloud Cover Assessment”, ACCA SPIE paper

[59] Irish Richard R., John L. Barker, Samuel N. Goward, and Terry Arvidson, “Characterization of the Landsat-7 ETM Automated Cloud-Cover Assessment (ACCA) Algorithm”, PHOTOGRAMMETRIC ENGINEERING & REMOTE SENSING, p1980-p1988, October 2006.

[59] LDCM Cloud Cover Assessment July 15th, 2008 Pat Scaramuzza, SGT U.S. Geological Survey Center for Earth Resources Observation and Science.

[60] Ackerman Steve, Kathleen Strabala, Paul Menzel, Richard Frey, Chris Moeller, Liam Gumley, Bryan Baum, Suzanne Wetzel Seemann, Hong Zhang, “Discriminating Clear-sky from cloud with MODIS – MODIS Algorithm Theoretical Basis Document (MOD35)”.

[61] Charantonis Anastase Alexandre, “Cloud detection algorithm development in preparation for the Sentinel-2 mission” 2009.